Title
Soil Processes and Microbial Communities in a Hyperarid System

Author
Finstad, Kari Michelle

Publication Date
2016

Peer reviewed|Thesis/dissertation

Soil Processes and Microbial Communities in a Hyperarid System

by

Kari Michelle Finstad

A dissertation submitted in partial satisfaction of the

requirements for the degree of

Doctor of Philosophy

in

Environmental Science, Policy and Management

in the

Graduation Division

of the

University of California, Berkeley

Committee in charge:

Professor Ronald G. Amundson, Chair
Professor Jillian F. Banfield
Professor Cecilia Demergasso
Professor David L. Shuster

Summer 2016

Abstract

Soil Processes and Microbial Communities in a Hyperarid System

by

Kari Michelle Finstad

Doctor of Philosophy in Environmental Science, Policy and Management

University of California, Berkeley

Professor Ronald G. Amundson, Chair

The Atacama Desert is a coastal desert in South America spanning both Peru and Chile. While the desert experiences a range of climate regimes, perhaps the most unique region of the desert lies in the north of Chile where annual precipitation is less than 2 mm. This hyperarid region of the desert often goes decades without precipitation and is believed to have maintained a semi-continuous hyperarid climate for the last few million years.

Hyperaridity has had a profound impact on the geochemical and biological processes of the region. One of the most notable and economically important features of the desert are the salars. Salars are the location of past lakes that have lost their surface water due to changes in climate and/or tectonic activity. They provide minable concentrations of iodine, boron, and other salts, and are recognized as one of the only habitats for microbial life in this region. Presently, they are covered in thick and rugged salt crusts, often made of sodium chloride (halite) and calcium sulfate (gypsum).

Due to the extreme and persistent aridity, shallow groundwater is pulled upward towards the surface via capillary flow. This upward water movement is the reverse direction of most well drained desert soils, and leaves a diagnostic imprint in the soil chemistry. The first chapter of my dissertation explores how soils in salars differ from those found in other more humid deserts, and proposes changes to the USDA Soil Taxonomy that would allow for a more accurate and informative classification of them.

To further understand and catalogue the rates and processes of soil formation in this unique environment, in my second chapter I examine the chemical and isotopic profiles of two soils of differing ages in the Salar Llamara, Chile. I found that soil development is actively occurring, with evaporation of shallow groundwater driving the major geochemical processes. The upward movement of water produces a distinctive salt profile, with the most soluble salts concentrated on the surface and the least soluble salts near the base.

Through monitoring and experimental work, I calculated long-term evaporation rates, and found that they decrease with soil age as the salt crust thickness increases. While it has been suggested that these salars are part of an ancient landscape, this work provides evidence that they are

dynamic and evolve on relatively short timescales. Finally, despite the lack of rainfall, I found that the crusts are able to sustain microbial growth by buffering environmental changes in temperature and relative humidity.

While the hyperarid region of the Atacama Desert only receives rare and infrequent precipitation, it is exposed to marine fog from the Pacific Ocean on a regular basis. The amount of fog changes predictably from west to east as the distance from the coast increases. For many years the Atacama Desert was suggested to be the dry limit to life. However, in the last decade it has been recognized that microbial communities are capable of surviving in salt crusts on the surface of salars. At a relative humidity over 75%, halite is able to absorb enough moisture from the atmosphere to create a saline solution in its mineral pores. In this way, salt crusts can provide organisms with liquid water in the absence of precipitation.

My third chapter is a detailed investigation of the microbial community composition and structure in this unique ecosystem. Using next metagenomics techniques, I reconstructed 124 distinct draft quality genomes from three sites along a fog frequency transect. All communities are comprised of a large variety of Halobacteriales*, Salinibacter*, Chlorophyta, and Cyanobacteria. Additionally, some communities contain lower abundances of Nanohaloarchaea, Actinobacteria, Gammaproteobacteria, Thermoplasmatales, and *Naegleria*. Candidate Phyla Radiation bacteria (OD1 and TM7) not previously reported from hypersaline environments before, were also found in low abundance in some of the communities.

While there is a lot of overlap in community membership across sites, samples cluster by site based on bacterial and archaeal abundance patterns. The concentration of photosynthetic organisms declines with increasing distance from the fog source (Pacific Ocean), and radiocarbon dating showed that carbon cycling is occurring more rapidly in sites with more fog events. I conclude that the strongest driver of community membership is fog delivered moisture, controlled by proximity to the coast.

The final chapter of my dissertation explores a unique late Quaternary paleoenvironmental record in loess deposits. Within what is largely a deflationary landscape, I found small loess dunes that have been slowly accreting for the last 20,000 years in depressions of the highly eroded Soledad formation. One of the unique local climate characteristics of this area is the strong and persistent on-shore winds.

Radiocarbon ages of organic matter embedded within the deposits show that the dunes began accumulating rapidly at the Last Glacial Maximum, and that the accumulation of sediment slowed considerably after the Pacific Ocean attained its present post-glacial level. Chemical and isotopic analysis of the sediment and fatty acids preserved within the dunes provide evidence for increased marine fog density and intensity of onshore westerly winds beginning 10,000 yr BP. At this time, grain size increases while accumulation rates simultaneously decrease, suggesting greater wind speeds and/or decrease in sediment supply. Organic sediment $\delta^{15}N$ values steadily decrease, suggesting a shorter path length between N upwelling (Pacific Ocean) and N deposition in the dunes. This unique and continuous record of paleo-conditions provides a window into local processes occurring over the last 20,000 years.

Table of Contents

Acknowledgements

First off, I would like to thank Ron Amundson for his continuous support and guidance throughout this process. Your encouragement and mentorship has made this possible. Thank you for opening my eyes to the world of soil and showing me how great research is done. Second, I would like to thank Jill Banfield for her dedication and willingness to take me in as one of her own. I am grateful for the opportunity to have learned metagenomics from the best. Other academic mentors I would like to thank include Todd Dawson and Gary Sposito. Cecilia Demergasso and Guillermo Chong, thank you for your generosity and sharing your perspective on the Atacama Desert with me. My work would not be what it is without the support of my collaborators, thank you Gary Andersen, Yvette Piceno, Jaime Barnes, Gavin McNicol, Ken Williford, and Michael Tuite for working with me and always contributing your best. Thank you Tim Teague, Paul Brooks, Stefania Mambelli, Wenbo Yang, and Anna Engelbrektson for your hours of analytical support.

I have much appreciation and gratitude for Amundson lab members, past and present, who have supported my research and been good company over the last six years: Marco Pfeiffer, Erik Oerter, Sarah Reed, Simona Balan, and Luiz Mezquita. You have made great friends and collaborators in the field and in the lab. Thank you to all the Banfield lab members who have been generous with their time and patient as I learned microbiology and metagenomics simultaneously: Alex Probst, Rose Kantor, Karen Andrade, Cindy Castelle, Sue Spaulding, and Brian Thomas.

I would like to thank all of the friends that I have made along the way in ESPM over the years, there are far too many to name. The camaraderie and support I received from you all has made a world of difference. Thank you to my fellow Jedi/Transformers for keeping me in balance while navigating these last few years. I would also like to thank my friends outside of academia for adding some variety to my life and an alternative perspective. A sincere thank you to my parents Terry and Stein for supporting and encouraging me throughout my life. Finally, thank you Chris for being my number one fan. Your support and stability have kept me going when I needed it most and you have always reminded me of what is most important when I've lost sight of it.

Chapter 1:
Hyperarid Soils and the Soil Taxonomy

Introduction

The Soil Taxonomy has undergone much evolution, particularly within the Aridisol order, since its initial publication in 1975 (Yaalon, 1995). As soils of previously understudied regions are examined, pedological features may be discovered that are inadequately described within the existing Soil Taxonomy (Soil Survey Staff, 1999). Many earth and ecological scientists rely on the taxonomic nomenclature of a soil to derive significant information about its origin and utility (Schimel and Chadwick, 2013). It is therefore important that the Soil Taxonomy continue to reflect current research and understanding if it is to remain pertinent and useful to scientists globally.

Much of the criteria currently used to classify Aridsols are derived from the deserts of western North America that span a broad range of altitudes, latitudes, temperatures, and moisture. The majority of this region is arid, with precipitation (P) to potential evapotranspiration (PET) ratios of 0.05 to 0.2. While challenging to life, plant available moisture can be available for significant periods of time and water is available to move downward under unsaturated flow. In contrast, international research in the past few decades has begun to reveal the pedological features of hyperarid environments ($P/PET < 0.05$) (eg. Amit and Yaalon, 1996; Ewing et al., 2006; Quade et al., 2007; Bockheim and McLeod, 2008). These soils bear genetic features considerably different from those in more humid environments, such as the deserts of North America. First, the landscapes lack or have minimal plant cover. A striking illustration of this is to compare Google Earth imagery to the distribution of a hyperarid climate shown in Fig. 1 – the low imprint of biology is striking. As a consequence of minimal plant cover, the cycling of organic matter and biotic mixing processes in these soils are largely absent. Additionally, in the more extreme hyperarid regions there is little leaching of the most soluble salts from the soil profile. In most North American deserts, soils have minor amounts of sulfates and even smaller quantities of more soluble salts such as halite. In contrast, the prolonged lack of precipitation in certain hyperarid environments has produced landscapes with solute accumulations far exceeding that found in more humid deserts. In the Atacama Desert for example, the near-continuous hyperaridity has preserved Pliocene-aged fluvial landforms and soils cemented with combinations of sulfates, chlorides, and nitrates (Rech et al., 2006; Amundson et al., 2012). Similarly, soils in different regions of Antarctica contain horizons cemented with nitrates, chlorides, and sulfates (Bockheim, 2014), and Pleistocene soils cemented with chlorides have been identified in the Negev Desert (Amit and Yaalon, 1996).

The present Soil Taxonomy lacks diagnostic horizons for soil horizons cemented with halite ($NaCl$) or enriched with nitratine ($NaNO_3$). More fundamentally, it lacks a way to distinguish the unique pedogenesis that occurs in hyperarid environments. Here we suggest that these omissions hinder the ability of scientists and researchers to convey the pedologic history and utility of these soils, which are found across the globe. In this paper we examine and discuss soils from the Atacama Desert in relation to their formation and classification as an illustrative example of hyperarid pedogenesis. We then summarize the literature on indurated salic and nitric horizons, and consider how the Soil Taxonomy might be amended to accommodate them.

Current Soil Taxonomy

The current Soil Taxonomy includes diagnostic horizons for a range of salts: $CaCO_3$ (calcic), $CaSO_4 \bullet 2H_2O$ (gypsic), and salts more soluble than gypsum (salic). To qualify, horizons with these salts are required to be at least 15 cm thick, non-cemented, and contain a threshold amount of the given salt (Soil Survey Staff, 1999). While gypsic and calcic horizons are specific to sulfate and carbonate respectively, salic horizons include all salts more soluble than gypsum. There is currently no means to designate a salic horizons composed primarily of halite or nitrate.

In addition to these diagnostic horizons, there are also petrogypsic and petrocalcic horizons that are cemented. Indurated gypsic and calcic horizons are defined by their lateral continuity, induration, and thickness (Soil Survey Staff, 1999). An indurated horizon is important in the Soil Taxonomy because it is indicative of great antiquity, restricted plant growth, and considerable limitations to the use of the soil. The current Soil Taxonomy does not, however, include an indurated salic (petrosalic) horizon, which in some hyperarid deserts is equally as important as petrogypsic and petrocalcic horizons.

Finally, the Aridic Soil Moisture Regime (SMR) is currently the most water-limiting in the Soil Taxonomy and includes soils in both aridic and hyperaridic climates. In normal years these soils are defined as dry (in the control section) more than 50% of the time while soil temperatures are above 5˚C at 50 cm depth and some or all parts of the soil are moist less than 90 consecutive days when the soil temperature is above 8˚C at 50 cm depth (Soil Survey Staff, 1999).

#	Geographical Location	Location of Horizon	Descriptive Term	Proposed Name	Reference
1	Atacama Desert, Chile	Subsurface	Nitric Horizon	Nitric	Ewing et al., 2006
2	Dry Valleys, Antarctica	Subsurface	Nitric Horizon	Nitric	Bockheim, 1997
3	Turpan-Hami area, China	Subsurface	Nitric Horizon	Nitric	Qin et al., 2012
4	Atacama Desert, Chile	Subsurface	Salic Horizon	Petrosalic	Ewing et al., 2006
5	Negev Desert, Israel	Subsurface	Petrosalic Horizon	Petrosalic	Amit and Yaalon, 1996
6	Dry Valleys, Antarctica	Subsurface	Petrosalic Horizon	Petrosalic	Bockheim, 1997
7	Kerman, Iran	Subsurface	Petrosalic Horizon	Petrosalic	Moghiseh and Heidari, 2012
8	Azran, Jordan	Subsurface	Hard Salic Horizon	Petrosalic	Khresat and Qudah, 2006
9	Namib Desert, Namibia	Subsurface	Pedogenic Halite Crust	Petrosalic	Watson, 1983
10	Death Valley, USA	Surface	Rock Salt	Petrosalic	Hunt et al., 1966
11	Libyan Desert, Egypt	Surface	Salt Crust	Petrosalic	Aref et al., 2002
12	Atacama Desert, Chile	Surface	Petrosalic Horizon	Petrosalic	This paper
13	Arabian Desert, Saudi Arabia	Surface	Blocky Salt Crust	Petrosalic	Goodal et al., 2000

Table 1. A selection of publications that have previously described an indurated salic or nitric horizon. Only horizons 10 cm or more in thickness were included. Map number corresponds to the number on Figure 1. The location of the horizon, either surface or subsurface, indicates the direction of water flow (downwards vs. upward, respectively). The original term used to describe the horizon is noted alongside the designation proposed in this study.

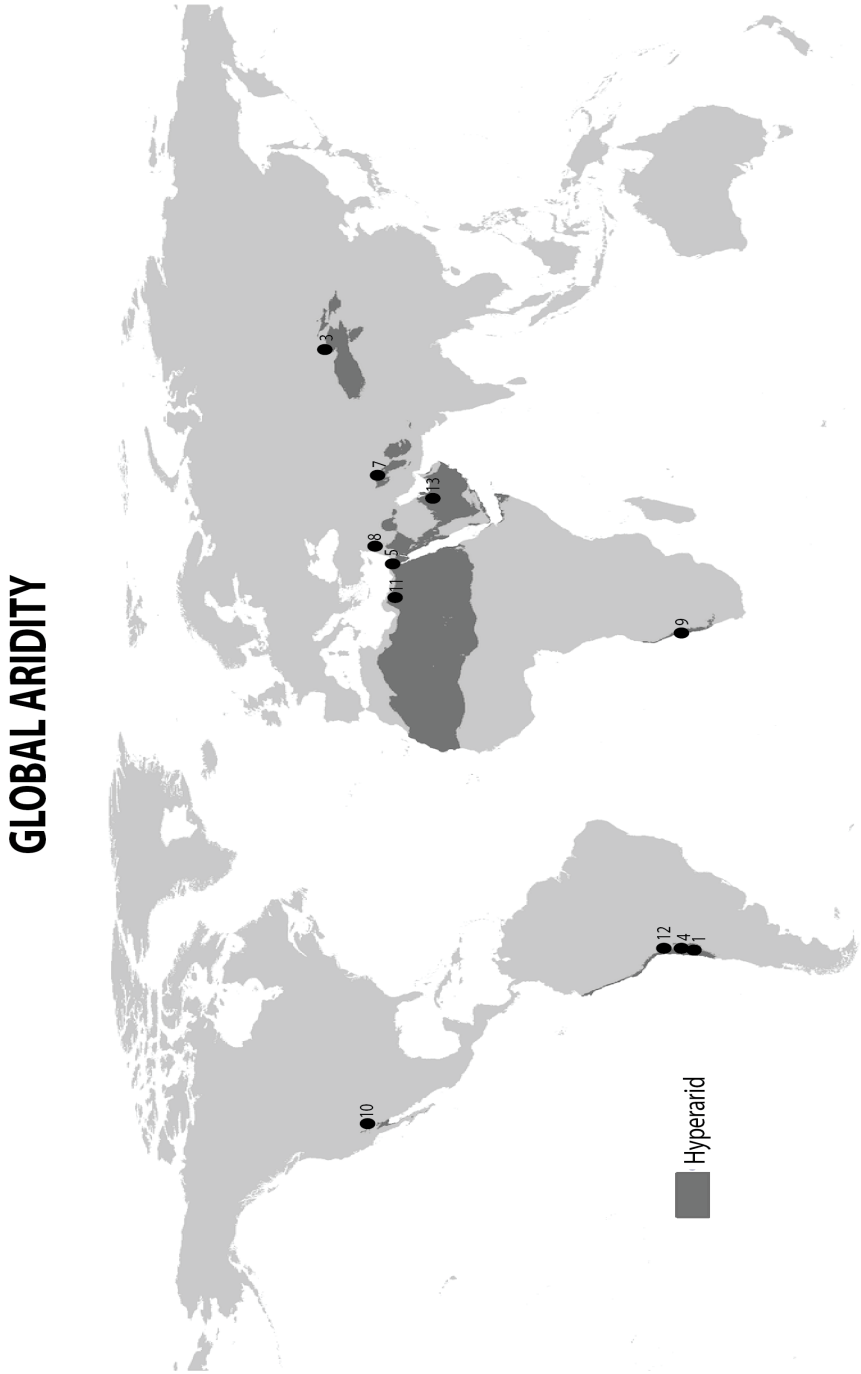

Figure 1. The global distribution of hypearidity in warm deserts. Points indicate the location of previously described indurated salic or nitric horizons and the numbers correspond to the references listed in Table 1. Soils #2 and #6 are not displayed because the aridity data set did not include values for polar regions. †Aridity data set is from Zomer et al., 2008, 2007 and available at http://www.cgiar-csi.org.

Global Distribution of Hyperaridity and Indurated Salic and Nitric Horizons

Aridity (in the climatological sense), is dependent on the relationship between moisture inputs and moisture losses, and is measured as P/PET. PET is calculated from measurements of mean monthly temperatures and the average number of daylight hours per month. At values of P/PET < 0.05, a region is considered to be hyperarid. Figure 1 shows the global distribution of hyperaridity. In 1997, the United Nations Environmental Programme concluded that 7.5% of the Earth's land surface is hyperarid and an additional 12.1% is arid (UNEP, 1997).

Indurated salt crusts are widespread and described in the literature by pedologists and sedimentologists, both in hyperarid and arid regions (Fig.1 and Table 1). Many of them are present in playas and undergo dynamic cycles of dissolution during the rainy season and recrystallization during the dry season. In contrast, precipitation events in hyperarid regions where rainfall is less than 100 mm $year^{-1}$ are too infrequent and insufficient to fully dissolve salt accumulation. This prolonged moisture deficit allows for the growth of thick indurated surface horizons from evaporating water.

The location of the horizon within the profile is dependent on the direction of water movement. Well-drained soils with downward migrating water develop petrosalic horizons in the subsurface. This is the case for soils #4 - 9 in Table 1. Alternatively, an upward movement of water concentrates very soluble salts at the surface where the petrosalic horizon forms (soils 10 - 13 in Table 1). Nitric horizons are widespread in the Atacama Desert, the Dry Valleys of Antarctica, and the Gobi Desert. The origin of these salt deposits has been traced to atmospheric deposition, and the presence of such large deposits signifies great antiquity (Qin et al., 2012).

The lack of nitric and petrosalic horizons in the current Soil Taxonomy makes it very difficult to determine the distribution of soils with these horizons, as there is no means to denote their presence using the taxonomic nomenclature. As demonstrated in Table 1, a variety terms have been used to describe them both by pedologists and sedimentologists. Regardless of the absence of these diagnostic horizons in the Soil Taxonomy, some authors have still chosen to use the terminology 'petrosalic' (Amit and Yaalon, 1996; Backheim, 1997; Moghiseh and Heidari, 2012).

A Case Study of Hyperarid Pedogenesis: The Atacama Desert

Climate and Geology

The aridity of the Atacama Desert is truly astounding. Geomorphic studies suggest that the Atacama has experienced a near-continuous hyperarid climate since the late Pliocene (Hartley and Chong, 2002; Amundson et al., 2012). Almost all of the land between 15 and 30 °S from sea level to 3500 m above sea level is considered hyperarid, which amounts to an area of ~150,000 km^2 (Houston and Hartley, 2003). There are a number of factors that conspire to maintain this extreme climate, including cold upwelling ocean currents, a rain-shadow from the Andes, and a subtropical high-pressure belt (Houston, 2006). It is not uncommon for areas in the region to receive precipitation only once every 10 years or more. Its tropical latitude leads to small temperature changes between winter and summer months.

While the full diversity of soils in the Atacama Desert is far from understood, this section provides an overview of typical features. Due to long-term and relatively continuous hyperaridity, the Atacama possesses suites of alluvial fans and terraces that are commonly Tertiary in age. Water is limiting for many common pedogenic processes. Even on Pliocene-aged soils chemical weathering, as measured by the formation of Bw or Bt horizons, is almost negligible. The slow but continuous deposition of dust and aerosols infills and physically expands the soils, while the rare rainfall events dissolve the incoming sulfate, chloride, nitrate salts and create soil horizons ordered by solubility of the salt (Ewing et al., 2006). Additionally, carbonates are nearly absent due to the lack of biological soil CO_2 and the dominance of the sulfate anion (Ewing et al., 2006; Quade et al., 2007). In the heart of the Atacama Desert at elevations of 1000 to 1500 m, sulfate horizons overly subsurface horizons enriched in soluble salts, dominantly NaCl with lesser quantities of $NaNO_3$. On older surfaces, both the sulfate and halite/nitrate horizons are indurated (Ewing et al., 2006).

These well-drained fans and terraces dominate the landscape and many terminate in internally drained basins. During cooler periods these basins may have formed pluvial lakes from Andean runoff, but as a result of tectonic deformation and prolonged hyperaridity they are now distinctive salt-covered flats or playas known in Spanish as salars. Due evaporative losses of the upward migrating water table, these salars are covered by a dense NaCl crust that continues to react with atmospheric humidity (Ericksen and Salas, 1990). Occasionally due to wind deflation of salts these crusts also are found extending beyond the playa "boundary".
In the Atacama Desert the subsurface pedogenic concentration of salts in the Bzm horizons on well-drained surfaces, particularly nitrates and iodates, are economically mineable resources. Soils containing caliche ore deposits (the local name for nitrate-rich horizons) are estimated to cover 2.8 million hectares of Chilean deserts. These deposits are the only natural source of nitrate in economically significant quantities, and the most concentrated horizons contain 6.5-8.5% $NaNO_3$ by weight (Harben and Theune, 2006). From the 19^{th} to the early 20^{th} century these horizons were mined heavily and became one of the largest sources of nitrate (Ericksen, 1981). Additionally, indurated salic horizons contain anomalously high concentrations of iodine (I) and chromium (Cr). Many of these indurated salic horizons contain I concentrations 3-4 orders of magnitude higher than average continental crust and currently serve as the greatest source of mined I in the world (Perez-Fodich et al., 2014).

In summary, there are two (though likely more) distinctive and widespread pedohydrological regimes: (1) alluvial fans and related terraces dominated by sparse downward soil water movement, and (2) dry lake beds or nearby environs impacted by the upward migration of waters. As we will discuss, being able to distinguish these settings taxonomically is an important objective.
.

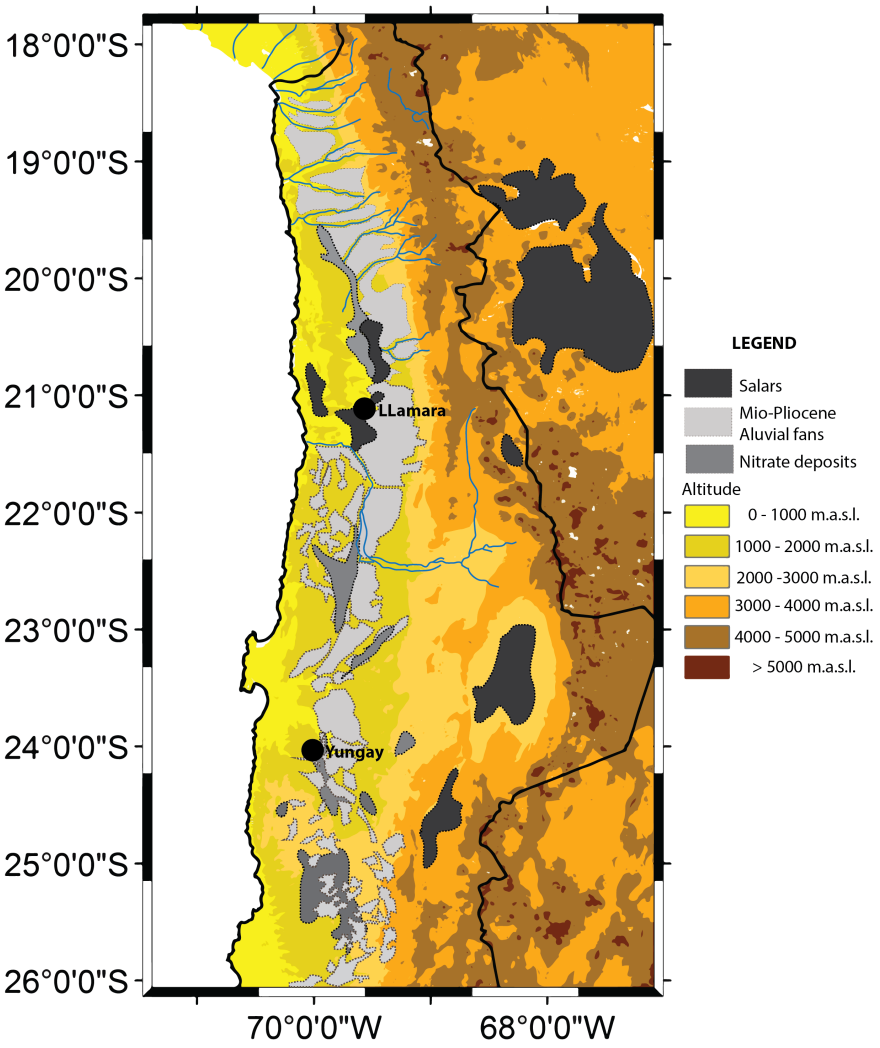

Figure 2. A map of the Atacama Desert with the location of the Yungay site and the Salar de Llamara sites. Salar deposits are shown in black, nitrate deposits in gray, and Mio-Pliocene alluvial fans in light gray.

Soil Descriptions

Here we discuss three soil pits from the Atacama Desert in nothern Chile representative of the two distinctive geomorphic surfaces described above (Fig. 2). The first soil is from a well-drained, post-Miocene alluvial fan in the Yungay region located near Antofagasta, Chile (Fig. 3). It was first described and reported by Ewing et al., 2006. Rare rainfall events occurring over the past millions of years have distributed atmospheric-derived salts through the profile as a function of their solubility. Porous and very soft gypsic horizons ~20 to 30 cm thick are commonly found on the surface (Table 2). These overly an indurated Petrogypic horizon that extends from 39-71 cm. Beneath the Petrogypsic horizon is a salic horizon (85-102 cm), and an indurated salic horizon from122-146 cm. The indurated salic horizon contains ~ 16 kg nitrate m^{-2} and 90 kg chloride m^{-2} (Fig. 5). The current classification of this soil to the subgroup level is a Petrogypsic Haplosalid.

The other two soils are from the Salar de Llamara near Iquique, Chile and represent a short chronosequence of Pleistocene and mid-Holocene soils (Fig. 4). These soil pits were excavated and characterized using standard pedological methods in June 2013 (Soil Survey Staff, 1999). Splits of each horizon were sent to ALS Geochemistry in Reno, NV for total chemical analysis and water extracts were analyzed for SO_4^{2-} and Cl^- using a Thermo Scientific Dionex ICS1500 with an AS25 analytical column (ion chromatography) at UC Berkeley. Both soils have an indurated salic horizon at the surface comprised almost entirely of halite, which varies in thickness from 51 cm at the Pleistocene site to 22 cm at the Holocene site. Below these horizons are gypsic and a calcic horizons (Fig. 6, Table 2). In contrast to the Yungay site, these soils have experienced a long history of upward migrating water driven by evaporation. This has resulted in a reverse order of salt accumulation with halite on the surface and sulfate deeper in the profile. Both of these soils are classified as Gypsic Haplosalids.

In the present Soil Taxonomy, the well-drained, post-Miocene soils in the Atacama Desert are commonly classified as Petrogypsic Haplosalids or Typic Petrogypsids depending on the depth of the salic (Bzm) horizon. These designations are insufficient because they confer no information about the presence of an indurated salic horizon, or the mineable quantities of nitrate or iodate. The soils we have observed within the salars are classified as Gypsic Haplosalids. Similarly, these designations provide no insight into the dense and nearly impenetrable halite crust that covers the surface, or the orientation of the gypsic and salic horizons relative to that in the more common well-drained soils. The inclusion of all three of these soils into Haplosalids is problematic. First, it would be highly desirable to distinguish the different soil forming environments and soil characteristics (Fig. 5 vs 6). Second, both soil types are greatly impacted by indurated salic horizons – the excavation of all of these soils requires the use of a jack hammer. Third, the presence of a rugged and indurated salic horizon on the soil surface is a feature of both pedogenic and practical interest.

Yungay - Pliocene[†] Petrogypsic Haplosalid			**Salar de Llamara - Holocene** Gypsic Haplosalid				**Salar de Llamara - Pleistocene** Gypsic Haplosalid			
Horizon	Depth (cm)	Cl^- (mmol/ g soil)	Horizon	Depth (cm)	SO_4^{2-} (mmol/ g soil)	Cl^- (mmol/ g soil)	Horizon	Depth (cm)	SO_4^{2-} (mmol/ g soil)	Cl^- (mmol/ g soil)
Bcyk	0-2	0.01	Bzm	0-22	3.07	7.90	Bzm1	0-3	0.23	8.10
Byk1	2-3	0.00	Bz	22-31	4.46	1.07	Bzm2	3-30	1.07	9.06
Byk2	3-12	0.01	Byk1	31-37	3.38	0.14	Bzm3	30-51	0.99	11.28
Byk3	12-26	0.01	Byk2	37-48	3.10	0.06	Bykz	51-65	2.46	0.65
By	26-39	0.01	Byk3	48-61	1.68	0.03	Ck1	65-82	0.55	0.79
Byknzm	39-71	0.19	Bk	61-73	0.28	0.03	Ck2	82-99	0.62	0.54
Bynzk	71-85	0.12	Cky1	73-78	3.19	0.00	Ck3	99-109	0.34	0.23
Byknz	85-102	0.26	Cky2	78-89	3.21	0.00				
Bnzyk	102-122	1.62	Cky3	89-94	3.08	0.03				
Bnzm	122-146	11.58								
Cnzky1	146-154	5.38								
Cknzy1	154-180	0.09								
Cknzy2	180-192	0.06								
Cknzy3	192-211	0.07								
Cknzy4	211-232	0.08								

Table 2. Horizon descriptions and soluble ion concentrations from the Yungay soil and the Holocene and Pleistocene soils in the Salar de Llamara.
[†]Data for the Yungay soil was taken from Ewing et al., 2006.

Figure 3. The Yungay site, a well-drained Mio-Pliocene alluvial fan. This is a very common landscape in the hyperarid Atacama Desert.

Figure 4. The Pleistocene site in the Salar de Llamara, a dried lake. The surface is now covered in a rough and indurated halite crust formed through prolonged hyperaridity and evaporative loss of the water table.

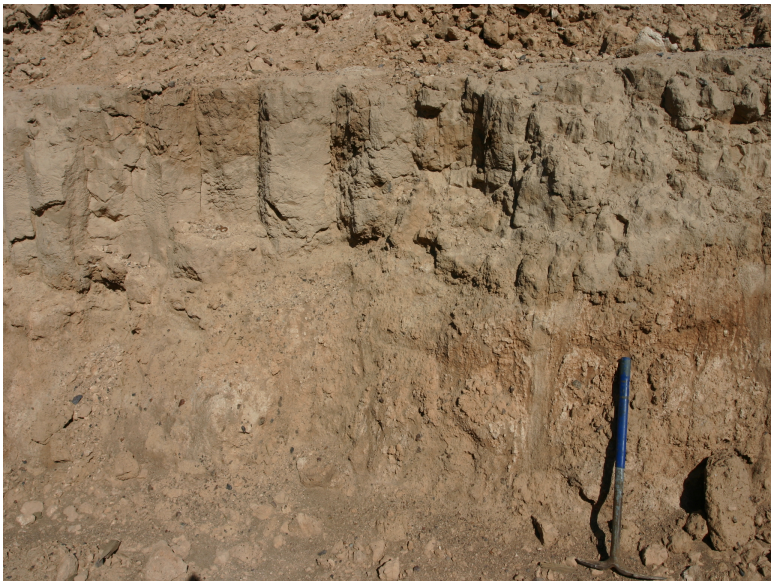

Figure 5. An example of a soil profile from a well-drained alluvial fan in the Atacama Desert. Large sulfate polygons are present at the surface overlying a nitrate rich horizon and an indurated salic horizon deeper in the profile.

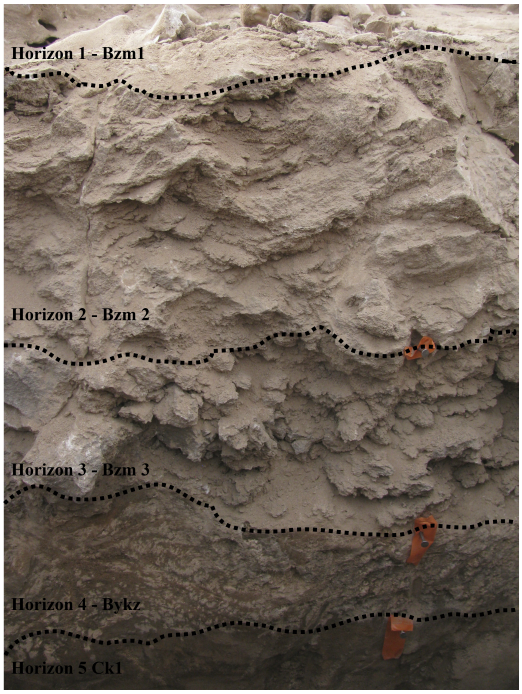

Figure 6. Soil profile from the Pleistocene site in the Salar de Llamara. The first 3 horizons (0-51cm) are hard, dense halite crust. These overly a sulfate-rich horizon at 51- 65 cm.

Proposed Amendments to the Soil Taxonomy

To better classify the diversity of desert soils such as those described above, and to effectively communicate the management best suited for them, we propose that the Soil Taxonomy be amended to better represent soils in hyperarid regions. This includes the addition of (1) a petrosalic diagnostic subsurface horizon, (2) a nitric diagnostic subsurface horizon, and (3) a Petrosalids great group in the Aridisols order. Additionally, we advocate for the definition and adoption of a Hyperaridic SMR. We suggest that the new diagnostic subsurface horizons be defined as described below.

Petrosalic horizon (Bzm)

A horizon at least 10 cm thick which must be cemented or indurated by salts more soluble that gypsum, and because of lateral continuity, roots can penetrate only along vertical fracture with a horizontal spacing of 10 cm or more.

This definition is analogous to that used for the definition of petrogypsic and petrocalcic horizons. The need for a diagnostic petrosalic horizon has been expressed in the past by others (eg. Bockheim, 1997) and was adopted by the International Union of Soil Scientists in 2007 (IUSS Working Group WRB, 2007). The lack of inclusion in the Soil Taxonomy thus far may stem from a belief that petrosalic horizons are rare or will slake in water. However these horizons occur in numerous regions of Earth (Table 1) and due to the prolonged extreme aridity under which they have formed will not slake in water.

Nitric horizon (Bz or Bzm)

A horizon 15 cm or more thick with 12 cmol(-)/L nitrate in 1:5 soil:water extract and in which the product of its thickness (in cm) and its nitrate concentration is $\geq$ 3,500.

This is the current criteria used to designate a Nitric Anhyorthel in Soil Taxonomy (Soil Survey Staff, 1999), and the same definition suggested for a nitric horizon by the International Committee on Permafrost Affected Soils (Bockheim, 1997). For a soil with a bulk density of 1.5 g cm^{-3} this is equivalent to 2.5% nitrate.

To accommodate these new diagnostic subsurface horizons we also propose the addition of a Petrosalids great group in the suborder Salids, and five subgroups to the new Petrosalids great group (Epi Petrosalids, Petrogypsic Petrosalids, Gypsic Petrosalids, Nitric Petrosalids, and Typic Petrosalids). We suggest that the new key for the Salids be as follows:

Petrosalids Great Group

Key to Great Groups

GBA. Salids that are saturated with water in one or more layers within 100 cm of the mineral soil surface for 1 month or more in normal years.

Aquisalids

GBB. Salids that have a petrosalic horizon within 200 cm of the soil surface.

Petrosalids

GBC. Other Salids.

Haplosalids

Petrosalids
Key to Subgroup
GBBA. Petrosalids that have a petrosalic horizon at the soil surface.

Epi Petrosalids

GBBB. Petrosalids that have a petrogypsic horizon within 100 cm of the soil surface.

Petrogypsic Petrosalids

GBBC. Petrosalids that have a gypsic horizon within 100 cm of the soil surface.

Gypsic Petrosalids

GBBD. Petrosalids that contain a horizon 15 cm or more thick with 12 cmol(-)/L nitrate in 1:5 soil:water extract and in which the product of its thickness (in cm) and its nitrate concentration is ≥ 3,500.

Nitric Petrosalids

GBBE. Other Petrosalids.

Typic Petrosalids

Hyperaridic Soil Moisture Regime (SMR)
Finally, we suggest that a fundamental way to distinguish pedogenesis in hyperarid climates is lacking. The creation of a Hyperaridic SMR would provide a critical means to distinguish between pedogenesis occurring in arid and hyperarid environments. This SMR should consider soils that experience rainfall averages incapable of removing soluble salts from the upper 150 cm over long time scales, therefore allowing the formation of indurated horizons. Such a revision to the Soil Taxonomy would require an international effort to arrive at an appropriate definition and classification system, however it would greatly enhance the usefulness of the Soil Taxonomy. To limit the need for major revisions to Aridisols, we suggest that the Hyperaridic SMR could be indicated at the family level (eg. coarse-gypseous, isothermic, shallow, hyperaridic Typic Petrogypsid).

Impact of Proposed Changes
With these proposed changes the well-drained, post-Miocene soils in the Atacama Desert would change from their current designation as Petrogypsic Haplosalids to Petrogypsic Petrosalids, and the salar soils would change from their present designation as Gypsic Haplosalids to Epi Petrosalids. Additionally, all of the indurated salic horizons described in Table 1 would be classified as petrosalic horizons and the horizons enriched with nitrate classified as nitric horizons. Changes to the classification of these soils would vary depending on other individual factors of the soil, however many of them would change at the Great Group and/or Subgroup level to incorporate the new additions proposed here. These changes would also facilitate a more accurate description of future soil surveys and analysis in other hyperarid locations.

Conclusions

As new research is compiled, it is becoming clear that soils of hyperarid regions have unique features and processes not occurring in the more humid deserts. Horizons present in hyperarid regions are not included as diagnostic horizons in the Soil Taxonomy and as a result these soils are not adequately identified by the current Aridisols architecture. We propose that the Soil Taxonomy be amended to include a petrosalic diagnostic subsurface horizon, nitric diagnostic subsurface horizon, and a Petrosalids great group within the Aridisols order. Additionally, future research to define a new Hyperaridic SMR should be considered. The goal of this paper is to present the pedological characteristics of hyperarid soils to a broad audience and begin a larger discussion of possible changes to the Soil Taxonomy. The changes proposed here would create a more encompassing classification system.

References

Amit, R., and D. Yaalon. 1996. The Micromorphology of Gypsum and Halite in Reg Soils - The Negeve Desert, Isreal. Earth Surface Processes and Landforms 21: 1127–1143.

Amundson, R., W. Dietrich, D. Bellugi, S. Ewing, K. Nishiizumi, G. Chong, J. Owen, R. Finkel, A.M. Heimsath, B. Stewart, and M. Caffee. 2012. Geomorphologic evidence for the late Pliocene onset of hyperaridity in the Atacama Desert. Geological Society of America

Aref, M., E. El-Khoriby, and M. Hamdan. 2002. The role of salt weathering in the origin of the Qattara Depression, Western Desert, Egypt. Geomorphology 45: 181–195.

Bockheim, J.G. 2014. Antarctic Soil Properties and Soilscapes. p. 293-315. In Cowan, D.A. (ed.), Antarctic Terrestrial Microbiology. Springer-Verlag Berlin Heidelberg.

Bockheim, J.G. 1997. Properties and Classification of Cold Desert Soils From Antarctica. Soil Science Society of America Journal 61: 224–231.

Bockheim, J.G., and M. McLeod. 2008. Soil distribution in the McMurdo Dry Valleys, Antarctica. Geoderma 144(1-2): 43–49.

Ericksen, G.E. 1981. Geology and Origin of the Chilean Nitrate Deposits. U.S. Geologic Survey Professional Paper 1188.

Ericksen, G.E., and R.O. Salas. 1990. Geology and Resources of Salars in the Central Andes. p. 151–164. In Ericksen, G.E., Canas Pinochet, M.T., Reinemund, J.A. (eds.), Geology of the Andes and its relation to hydrocarbon and mineral resources. Circum-Pacific Council for Energy and Mineral Resources, Houston, Texas.

Ewing, S.A., B. Sutter, J. Owen, K. Nishiizumi, W. Sharp, S.S. Cliff, K. Perry, W. Dietrich, C.P. McKay, and R. Amundson. 2006. A threshold in soil formation at Earth's arid–hyperarid transition. Geochimica et Cosmochimica Acta 70(21): 5293–5322.

Goodall, T., C. North, and K. Glennie. 2000. Surface and subsurface sedimentary structures produced by salt crusts. Sedimentology 47: 99–118.

Harben, P., and C. Theune. 2006. Nitrogen and Nitrates. p. 671–678. In Kogel, J., Trivedi, N., Barker, J., Krukowsk, S. (eds.), Industrial Minerals and Rocks: Commodities, Markets, and Uses. 7 ed. Society for Mining, Metallurgy, and Exploration, Inc.

Hartley, A., and G. Chong. 2002. Late Pliocene age for the Atacama Desert: Implications for the desertification of western South America. Geology 30: 43–46.

Houston, J. 2006. Variability of Precipitation in the Atacama Desert: Its Causes and Hydrological Impact. International Journal of Climatology 26: 2181–2198.

Houston, J., and A. Hartley. 2003. The Central Andean West-Slope Rainshadow and Its Potential Contribution to the Origin of Hyper-Aridity in the Atacama Desert. International Journal of Climatology 23: 1453–1464.
Hunt, C., T. Robinson, W. Bowles, and A. Washburn. 1966. Hydrologic Basin Death Valley California. Geological Survey Professional Paper 494-B.
IUSS Working Group WRB. 2007. World Reference Base for Soil Resources, 2006. FAO,Rome.
Khresat, S.A., and E.A. Qudah. 2006. Formation and properties of aridic soils of Azraq Basin in northeastern Jordan. Journal of Arid Environments 64(1): 116–136.
Moghiseh, E., and A. Heidari. 2012. Polygenetic saline gypsiferous soils of the Bam region, Southeast Iran. Journal of Soil Science and Plant Nutrition 12: 729–746.
Perez-Fodich, A., M. Reich, F. Alvarez, G.T. Snyder, R. Schoenberg, G. Vargas, Y. Muramatsu, and U. Fehn. 2014. Climate change and tectonic uplift triggered the formation of the Atacama Desert's giant nitrate deposits. Geology 42(3): 251–254.
Qin, Y., Y. Li, H. Bao, F. Liu, K. Hou, D. Wan, and C. Zhang. 2012. Massive atmospheric nitrate accumulation in a continental interior desert, northwestern China. Geology 40(7)
Quade, J., J.A. Rech, C. Latorre, J.L. Betancourt, E. Gleeson, and M.T.K. Kalin. 2007. Soils at the hyperarid margin: The isotopic composition of soil carbonate from the Atacama Desert, Northern Chile. Geochimica et Cosmochimica Acta 71(15): 3772–3795.
Rech, J.A., B.S. Currie, G. Michalski, and A.M. Cowan. 2006. Neogene climate change and uplift in the Atacama Desert, Chile. Geology 34(9): 761.
Rech, J.A., J. Quade, and W.S. Hart. 2003. Isotopic evidence for the source of Ca and S in soil gypsum, anhydrite and calcite in the Atacama Desert, Chile. Geochimica et Cosmochimica Acta 67(4): 575–586.
Schimel, J., and O. Chadwick. 2013. What's in a name? The importance of soil taxonomy for ecology and biogeochemistry. Frontiers in Ecology and the Environment 11(8): 405–406.
Soil Survey Staff. 1999. Soil Taxonomy: A Basic System of Soil Classification for Making and Interpreting Soil Surveys. 2nd ed. United States Department of Agriculture - Natural Resources Conservation Service.
UNEP. 1997. World Atlas of Desertification. 2nd ed. United Nations Environmental Programme, Nairobi, Kenya.
Warren-Rhodes, K.A., K.L. Rhodes, S.B. Pointing, S.A. Ewing, D.C. Lacap, B. Gómez-Silva, R. Amundson, E.I. Friedmann, and C.P. McKay. 2006. Hypolithic Cyanobacteria, Dry Limit of Photosynthesis, and Microbial Ecology in the Hyperarid Atacama Desert. Microb Ecol 52(3): 389–398.
Watson, A. 1983. Evaporite sedimentation in non-marine environments. p. 163–185. In Goudie, A., Pye, K. (eds.), Chemical Sediments and Geomorphology. Academic Press Inc., London, England.
Yaalon, D. 1995. The soils we classify: Essay review of recent publications on soil taxonomy. Catena 24: 233–241.
Zomer, R., D. Bossio, A. Trabucco, L. Yuanjie, D. Gupta, and V. Singh. 2007. Trees and Water: Smallholder Agroforestry on Irrigated Lands in Northern India. International Water Management Institute (IWMI Research Report 112), Colombo, Sri Lanka.
Zomer, R., A. Trabucco, D. Bossio, O. van Straaten, and L. Verchot. 2008. Climate Change Mitigation: A Spatial Analysis of Global Land Suitability for Clean Development Mechanism Afforestation and Reforestation. Agriculture Ecosystems and Environment 126: 67–80.

Chapter 2:
Rates and Processes of Soil Formation in Salars of the Atacama Desert, Chile

Introduction

Geochemical processes in the Atacama Desert are limited by water. Most of the region consists of uplands and alluvial fans dependent on sparse rainfall (< 2 mm y^{-1}) to drive soil and geochemical processes. However, the region also contains closed basins that receive both surface runoff and subsurface flow from the adjacent High Andes. Once a lake or wetland is desiccated, the evaporation of shallow groundwater by capillary flow promotes an upward movement of solutes, a direction that is the reverse of the normal water trajectory of most desert soils (Finstad et al., 2014). Studies of soil formation in these geological settings are very limited, and none have been conducted in northern Chile.

In Chile, salt covered evaporitic basins are called salars and are distinguishable by the hard salt crusts commonly found on their surfaces (Chong, 1984; Ericksen and Salas, 1990). Approximately half of the salars in northern Chile contain halite (NaCl) crusts, an area of more than 4,000 km^2 (Stoertz and Ericksen, 1974). Most of the salars are located in the Andes, with only a handful in the Central Depression near to the Pacific coast. Salars in this region of the world are of growing significance. First, fluid migration and chemical fractionation have locally deposited economically viable concentrations of iodine, boron, and other salts (Boschetti et al., 2007; Perez-Fodich et al., 2014; Chong et al., 2000). Second, somewhat paradoxically, salt crusts on the surface of salars can harbor microbial communities persisting on liquid water obtained through the deliquescence of halite (Davila et al., 2013). Presently, there is only a preliminary understanding of the geological evolution of these crusts and on how these processes influence the microbial communities (Artieda et al., 2015). The observation of microorganisms surviving in a hyperarid salt environments such as the Atacama Desert is relevant to Mars, where halite-rich outcrops have been identified (Osterloo et al., 2008).

A pedogenic process-oriented understanding of salar evolution is still lacking. To address some of these issues, we examined the chemical and isotopic profiles of salts in the Salar Llamara within the Central Depression. We focus on two sites, one 15,484 cal yr BP and one 19,348 cal yr BP, to understand the rates of geochemical processes, and the resulting nature and properties of the unique soils in these locations.

Geological setting

The Salar Llamara lies in the Central Depression in northern Chile (Fig. 1). Since the Miocene the area has been part of an evaporitic basin, one whose area has decreased over time due to the development of drainage systems to the Pacific (Pueyo et al., 2001; Saez et al., 1999). Geological maps and fieldwork conducted as part of this study identified what are apparently some of the most recent major fresh water lakes. The lakes or wetlands were likely formed during episodes of increased Andean runoff (Gayo et al., 2012; Nester et al., 2007; Rech et al., 2002), and their subsequent drying has formed a distinctive salar.

One of the sites is located on a younger unit of lacustrine origin, mapped as PlHs (undifferentiated Pleistocene-Holocene saline deposits of halite, sulfate, and nitrates). The other site is slightly higher in elevation and is either lacustrine in origin or formed on the distal end of an alluvial fan, and is mapped as PlHa(p) (Pleistocene-Holocene alluvial deposits of antiquity, playa facies) (Quezada et al., 2012) (Fig. 2). For simplicity, we refer to them here as Qh and Qp, respectively. The sediment underlying the halite crust in both locations is a very fine-grained, laminated sediment consistent with a lacustrine setting or distal alluvial fans. Occasional strata of what appear to be freshwater marls are also present. Radiocarbon dating of organic matter within the sediments revealed a generally declining age with decreasing depths, and distinctive age differences between the two sites. Samples from the Qh site are 12,209-15,484 cal yr BP and samples from the Qp site are 19,144-19,348 cal yr BP (Table 1).

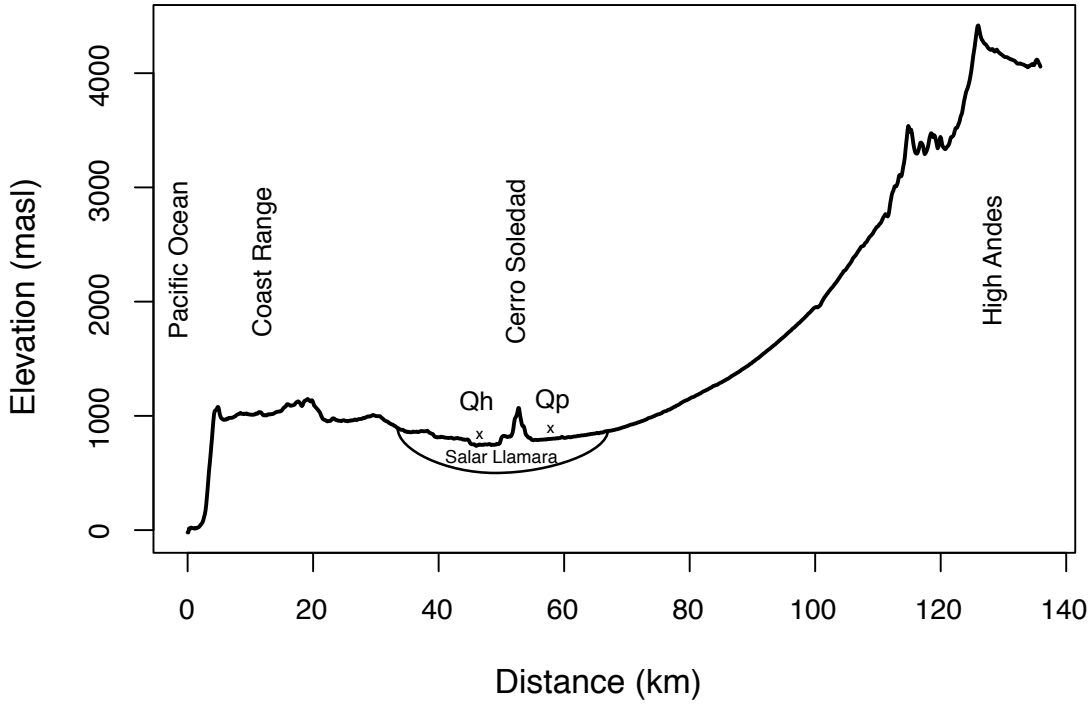

Figure 1. Elevation profile of the Salar Llamara and field sites. The Salar Llamara sits in the Central Depression created by the High Andes to the east and Coast Range to the west. Digital elevation model (DEM) was taken from GeoMapApp (www.geomapapp.org).

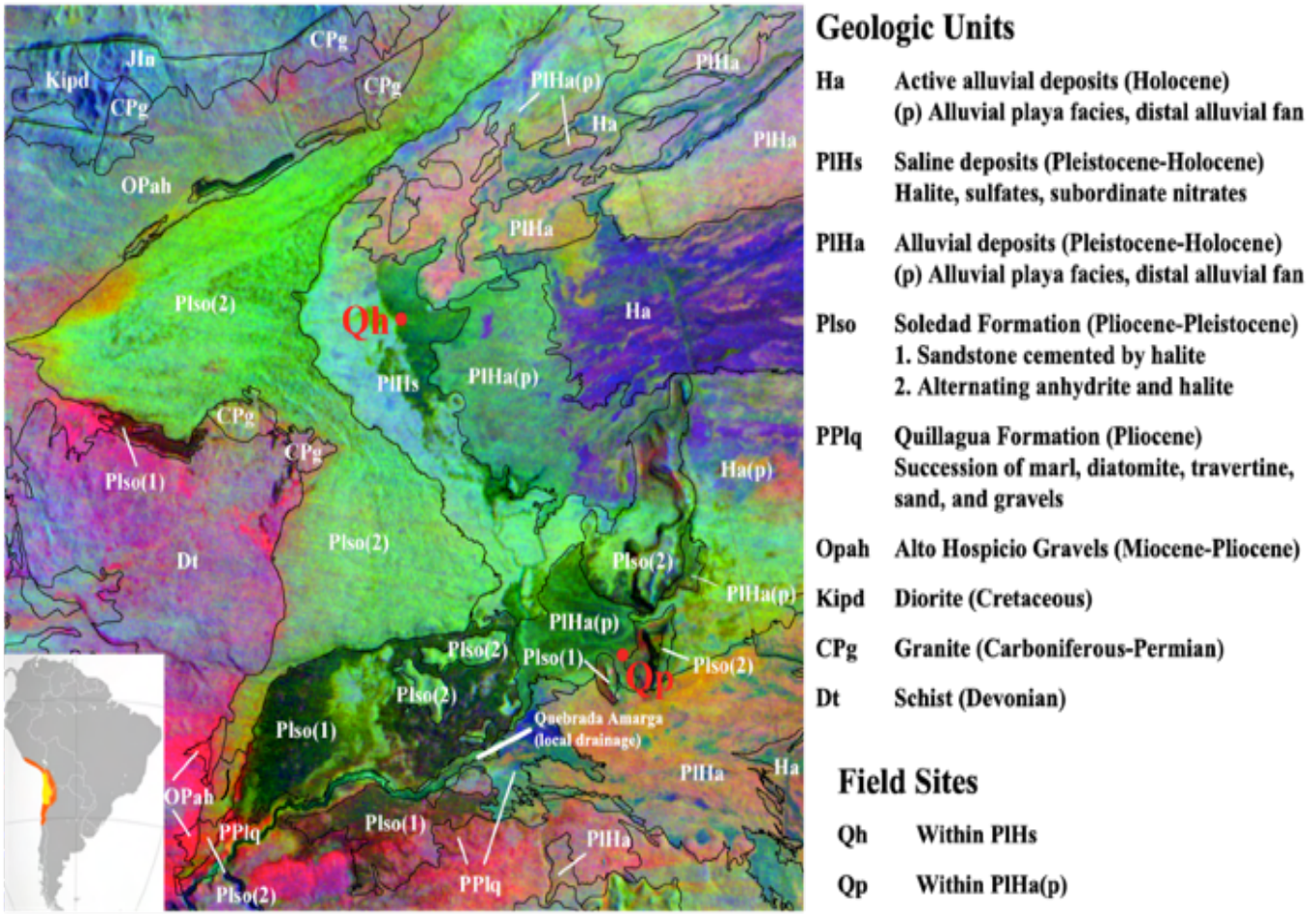

Figure 2. Location of fieldsites within the Salar Llamara in the hyperarid region of the Atacama Desert, Chile. Geological units were taken from Quezada et al. (2012). The geologic map is overlaid with a decorrelation stretch of Advanced Spaceborne Thermal Emission and Reflection Radiometer (ASTER) infrared bands 13, 12, and 11 highlighting the distribution of halite in green (image courtesy of Matthew C. Jungers).

Methods

Site description and soil sampling
Soils were excavated to depths of ~1 m with the assistance of a portable jackhammer. Soil features were identified and described using methods outlined in the USDA Soil Survey Manual (Soil Survey Staff, 1999). Bulk soil samples of identified horizons were placed in zip lock bags and transported back to the lab. Subsamples were taken in ~5 cm increments from the Bzm horizons at each site for $\delta^{37}Cl$ analysis. Three halite nodules from each site were also collected for subsequent study, and a groundwater sample was obtained from a backhoe trench that had been emplaced near the Qh site.

Environmental monitoring
Decagon Devices Inc. (Pullman, WA) microclimate monitoring systems were installed at each site to track hourly fluctuations in air temperature, pressure, and relative humidity, and a leaf wetness sensor was installed to detect fog and dew condensation. Because it did not rain during the year of study, we assume that any "wetness" recorded by the leaf wetness sensor is due to dew formation on the surface. A value of 475 counts was chosen as the threshold for the presence of dew, which according to the manufacturer is a conservative threshold. Monitoring began June 2013 and ran continuously for 14 months.

Seven Onset HOBO® Pro v2 (U23-002) temperature and relative humidity (T/RH) sensors were installed within halite nodules at each site, following the approach of Davila et al. (2008). Halite nodules were bored using an electric drill, and T/RH sensors (~1 cm) were inserted in the boreholes. Once a sensor was inserted into the crust, the hole was sealed with epoxy. The sensors were installed into the crust using slightly different methods at the two sites. At the Qh site, boreholes were made directly into the side of halite nodules. At the Qp site, an electric saw was first used to cut the nodule in half before sensor emplacement (Fig. 3). Removing half of the nodule using the saw (at the Qp site) allowed for the monitoring of denser crust located deeper within the nodule than would otherwise be accessible without first removing outer layers (at the Qh site).

An additional sensor was positioned just beneath the surface of one of the common surface polygons (parallel to the surface) at each site. Three additional T/RH sensors were placed at different depths within each soil, horizontally installed from the excavation walls. In total, the two uppermost soil sensors were inserted within the cemented halite horizons, while the lower two were in the fine-grained sediments. At the Qh site they were placed at 2, 20, 60, and 98 cm, and at the Qp site at 2, 37, 58, and 119 cm. All sensors recorded hourly fluctuations in T and RH beginning in June 2013 and ran continuously for 14 months.

In June 2013, the entire covering of halite nodules and surface crust was removed from a 1.5 m^2 plot at the Qh site. A Bushnell 119636C camera was then positioned to take a photograph every hour of the site to record the development and regeneration of new material. The camera was allowed to run for 2 years before photos were downloaded. After 14 months, a sample of the regenerated crust was removed and taken back to the lab for analysis.

Figure 3. Installation of temperature and relative humidity sensors within the halite nodules at each site. Sensors were installed directly into the side of nodules at the Qh site (a), and installed deeper within the nodule at the Qp site (b) after section the nodule with an electric saw. Approximate size of sensor is 1 cm diameter.

Analytical methods

Soil chemistry and exchangeable salts

Soil samples were dried, sieved to < 2 mm, and pulverized with a mortar and pestle. Splits of each soil horizon were sent to ALS Geochemistry in Reno, NV for major and rare earth element concentration (CCP-PKG01) and measurement of Cl concentrations by nitric acid digestion and titration (CL-VOL66). Water extracts of the soil samples and the material that was removed from the regenerated surface crust at the Qh experimental plot were analyzed for SO_4^{-2} and Cl^- using a Thermo Scientific Dionex ICS1500 with an AS25 analytical column (ion chromatography) at UC Berkeley. Pulverized soil was dissolved in excess deionized water and shaken for 4 hours to completely dissolve all salts. The samples were then filtered through a 0.2 μm filter and stored in a refrigerator at 2 °C for less than one week prior to analysis. Standards made from the Dionex Seven Anion Standard (No. 05790) were analyzed along with the samples. Calcium, potassium, and sodium in water extracts were determined using an ICP-OES in the College of Natural Resources at UC Berkeley. For these analyses, a portion of the water extracts prepared above was diluted in 2% HNO_3. Standards were created using Inorganic Ventures ICP standards CGNA1, CGK1, and CGCA1 and used to calculate final sample concentrations. The relative standard deviation (RSD) are better than 2% for each element based on daily analysis.

Radiocarbon measurements

Three halite nodule samples from each site were prepared for radiocarbon analysis by first removing inorganic carbon and excess salts. 20 g of pulverized halite was soaked in 1 M HCl for 24 hours with intermittent shaking to agitate the solution, followed by centrifuging and decanting the acidic supernatant. To ensure complete removal of HCl, the samples underwent alternating soaking and shaking in deionized water for 24 hours, then they were centrifuged and the supernatant discarded. This washing process with deionized water was repeated twice before samples were dried at 60 °C. A similar procedure was used to prepare two soil samples from each soil pit, with the exception that pulverized soil was soaked in 0.5 M HCl solution for inorganic carbonate removal. One carbonate sample from a marl lens near the Qh site was prepared for analysis by acid etch. The material was washed in deionized water to remove associated organic sediment and debris, then crushed and repeatedly subjected to HCl etches to eliminate secondary carbonate components.

Radiocarbon analysis of the soil pit and halite samples was performed on the Van de Graaff FN accelerator mass spectrometer (AMS) at the Center for Accelerator Mass Spectrometry at Lawrence Livermore National Laboratory, Livermore CA. Approximately 0.5 g of washed sample was prepared for ^{14}C measurement by sealed-tube combustion to CO_2 in the presence of CuO and Ag, and then reduced into iron powder in the presence of H_2 at 570 °C (Vogel et al., 1984). Beta Analytic Inc. analyzed the carbonate sample from nearby the Qh pit by using an accelerator mass spectrometer (AMS) after the reduction of sample carbon to graphite. The University of California, Irvine Keck Carbon Accelerator Mass Spectrometry facility analyzed the tree trunk sample from the coppice dune on a 500 kV compact AMS unit from National Electrostatics Corporation. $\delta^{13}C$ values were used to correct for fractionation and ^{14}C isotope values are reported in $\Delta^{14}C$ notation and corrected for ^{14}C decay since 1950 (Stuiver and Polach, 1977). Radiocarbon ages were calibrated to calendar yr BP using the CALIBomb online program

(http://calib.qub.ac.uk/CALIBomb/) with the dataset and extension curve corresponding to our study region (SH_CAL13; SHZ1_2) (Hogg et al., 2013; Hua et al., 2013).

Sulfate stable isotope ratios

Sulfate S stable isotope ratio analysis was performed in the Laboratory for Environmental and Sedimentary Isotope Geochemistry at the Department of Earth and Planetary Science, UC Berkeley. Soil sulfate was dissolved in water by shaking pulverized soil for 4 hours in excess deionized water. Sediment was then removed by filtering through a 0.2 μm paper filter. Sulfate was precipitated as $BaSO_4$ by adding excess 1 M $BaCl_2$ to the solution, then dried at 65 °C (following the protocol outlined in Michalski et al. (2004)).The same procedure was used to measure the groundwater sulfate S from the Qh site. Approximately 50-200 μg of $BaSO_4$ sample was run in duplicate on a GV Isoprime isotope ratio mass spectrometer and a Eurovector Elemental Analyzer (EuroEA3028-HT). The analytical precision of the measurement is better than 0.2‰. Values are reported as $\delta^{34}S$ relative to CDT.

Chlorine stable isotope ratios

The chlorine stable isotope composition of soil leachates and groundwater samples were determined in the Department of Geological Sciences, University of Texas at Austin. Chlorine was extracted from pulverized soil by shaking in excess ultrapure (18 MΩ) deionized water for 4 hours, then filtering through a 0.2 μm filter. Samples were prepared following the procedures of Eggenkamp (1994) as modified by Barnes and Sharp (2006) and Sharp et al. (2007). Sulfur was removed as H_2S by adding 8 mL of 50% HNO_3 and heating for 3 hrs at 80 °C. 4 mL of 1M KNO_3 was then added to reach high ionic strength, followed by 1 mL of 0.4 M $AgNO_3$. AgCl was allowed to precipitate overnight in the dark then filtered through a glass fiber filter. The filter and precipitate were then inserted into a Pyrex tube and pumped to vacuum. Samples were reacted with 10 μL CH_3I to produce CH_3Cl. The tubes were sealed and allowed to react at 80 °C in the dark for 48 hours before analysis. $\delta^{37}Cl$ values were measured on a ThermoElectron MAT 253 mass spectrometer and are reported in standard per mil notation vs. SMOC (Standard Mean Ocean Chloride; $\delta^{37}Cl$ SMOC = 0‰). Several duplicate samples from each site were run along with seawater standards. The analytical precision is ± 0.14‰ based on the analyses of in-house seawater standards over the past year.

Carbonate stable isotope ratios

Carbonate C and O stable isotope analysis was performed in the Laboratory for Environmental and Sedimentary Isotope Geochemistry at the Department of Earth and Planetary Science, UC Berkeley. Pulverized soil samples were washed 3 times with deionized water to remove excess salts then dried at 50 °C overnight. 10-100 μg of calcite was analyzed using a GV IsoPrime mass spectrometer with a Dual-Inlet and MultiCarb system. Each unknown sample was run in duplicate and several replicates of the international standard (NBS19) and two internal lab standards (CaCO3-I & II) were measured during the run. The overall external analytical precision is ±0.04‰ for $\delta^{13}C$ values and ±0.07‰ for $\delta^{18}O$ values. $\delta^{13}C$ values are reported relative to V-PDB and $\delta^{18}O$ values relative to V-SMOW.

Results and discussion

Geological setting

While some of the NaCl crusts in salars of the region are of Tertiary origins, field observations and radiocarbon dating of the soils examined here reveal that they have formed over late Pleistocene lacustrine deposits (see dating discussion which follows). Surrounding the outlines of the Qh salar, and in some places within the salar, there are salt-encrusted coppice dunes. A radiocarbon date from the carbonized trunk of a bush on one of these nearby dunes was 547 cal yr BP (Table 1). This suggests that both that the loss of surface water and the formation of salt indurated landscapes can occur over a short geologic time frame.

Based on the boundary between flat lying sediments and salt encrusted coppice dunes, the "shoreline" of the Qh salar is located at ~760 m.a.s.l. Two radiocarbon constraints are available for this former wetland or lake. First, a radiocarbon measurement of a marl lens obtained from an excavation at about 50 cm depth at the wetland periphery yields an age of 7,343 cal yr BP (Table 1). Second, organic matter embedded in the apparently lacustrine sediments from our soil pits provided ages of 12,209 and 15,484 cal yr BP (Table 1).

The Qh landform is incised 10 to 15 m into remnants of an older lacustrine or marsh-like setting present at ~ 775 m.a.s.l. Organic material in fine-grained sediments exposed in the soil excavation yielded radiocarbon ages of 19,144 and 19,348 cal yr BP (Table 1). This unit has been dissected by streams draining to the present basin low point (Qh), as indicated by alluvial fans that cut through this geological unit. The reasons for incision likely include both the ongoing tectonic tilting of the region (Allmendinger et al., 2005; Jordan et al., 2014) and the ongoing incision of the Quebrada Amarga, the drainage system that connects the Rio Loa to the regional base level. The ages of the organic material in the soils coincides with two well-documented wet periods known as the Central Andean Pluvial Events (CAPE), which activated stream discharge of the tributaries of the Salar Llamara (Quade et al., 2008).

Facility	Facility #	GPS	Site	Sample	Depth cm	$\delta^{13}C$ (‰)	$\Delta^{14}C$	±	^{14}C age cal yr BP	±
CAMS	166850	21°11'59.43"S 69°40'38.42"W	Qh	halite	surface	-25.44	9.3	3.0	modern	-
CAMS	166851	21°11'59.77"S 69°40'37.19"W	Qh	halite	surface	-24.77	8.8	3.3	modern	-
CAMS	166852	21°12'1.02"S 69°40'36.52"W	Qh	halite	surface	-24.89	7.4	3.0	modern	-
CAMS	165364	21°12'2.12"S 69°40'38.90"W	Qh	Qh 4	37 - 48	-27.43	-733.9	10.3	12209	817
CAMS	165162	21°12'2.12"S 69°40'38.90"W	Qh	Qh 10	94 - 96	-27.70	-801.4	1.9	15484	270
CAMS	166846	21°20'46.41"S 69°34'36.68"W	Qp	halite	surface	-29.41	-281.0	2.5	2546	54
CAMS	166847	21°20'46.92"S 69°34'36.18"W	Qp	halite	surface	-27.01	-623.5	2.9	8521	117
CAMS	166849	21°20'46.63"S 69°34'35.14"W	Qp	halite	surface	-25.99	-234.2	2.5	1995	68
CAMS	165159	21°20'45.46"S 69°34'37.56"W	Qp	Qp 5	65 - 82	-27.17	-865.2	2.0	19348	328
CAMS	165161	21°20'45.46"S 69°34'37.56"W	Qp	Qp 8	109 - 120	-26.80	-861.5	2.0	19144	302
UCIAMS	165230	21°12'26.81"S 69°38'19.97"W	near Qh	coppice dune bush trunk	surface	-	-72.4	1.8	547	17
Beta	263666	21°10'27.2"S 69°37'01.9"W	near Qh	marl lens	50	0.90	-	-	7343	79

Table 1. Radiocarbon dates from two samples from within the soil pits and three halite nodules from the surface. Additional dating was done from near the Qh site from a trunk of a carbonized bush on a salt encrusted coppice dune and from carbonate sample taken from a marl lens near the periphery of the shoreline. Radiocarbon ages were calibrated to calendar yr BP using the CALIBomb online program (http://calib.qub.ac.uk/CALIBomb/) with the dataset and extension curve corresponding to our study region (SH_CAL13; SHZ1-2) (Hogg et al., 2013; Hua et al., 2013).

Soil profiles

Both soils are classified as Gypsic Haplosalids according to the USDA Soil Taxonomy (Fig. 4; Table 2). They each have a continuous cemented halite layer (Bzm) on the surface, though the thickness of this layer differs between sites. At the Qh site it spans 0-22 cm, and at the Qp site 0-51 cm. Beneath the Bzm layers the soil material appears to be of lacustrine origin, with varying degrees of sand, silt, and clay. From 22-73 cm in the Qh profile, moist and soft layers of reddish silt and sand-rich material containing visible sulfate crystals were present. Further below this, yellowish calcite containing horizons were found at 73-94 cm, with loose sand below this at 94-96 cm.

The Qp site has a similar soil chemical sequence. Beneath the Bzm horizon, soft sulfate concentrations were observed from 51-65 cm. Deeper in the profile from 65-99 cm, organic material and charcoal pieces were present within moist and soft layers of variegated black, orange, and grey. A horizon of loose sandy material was observed from 99-109 cm, and 109-120 cm was comprised of variegated brown material with calcite seams.

Most playas and saltpans undergo repeated cycles of wetting and drying as the surface receives precipitation during seasonally wet months and evaporation of this water during the dry months. This cycle is well-documented to create stratigraphic profiles with alternating mud from the flooding of the surface, and halite layers deposited during evaporation (Lowenstein and Hardie, 1985). The sequence of soil horizons described above from the Qh and Qp sites do not show this alternating pattern, rather they have evaporitic horizons concentrated at the surface and lacustrine material concentrated deeper in the profile. This is indicative that this salar has not undergone repeated cycles of wetting and drying, but instead has been continuously drying since the final stages of lake/marsh evaporation.

A groundwater lens was present at the Qh excavation, and a nearby backhoe pit suggests that the local water table is at ~2.5 m below the surface. In contrast, groundwater was not observed at the Qp location and is greater than 5 m below the surface based on the absence of water in stream channels incised nearby into the landform. However, both the soil excavation and natural exposures along the incised stream channels revealed moist sediment. Rates of evaporation are highly dependent on the depth of the groundwater, with shallower water leading to more rapid evaporation (Houston, 2006). A more detailed discussion on the rates of salt accumulation and evaporation can be found later in sections 4.3 and 4.4.

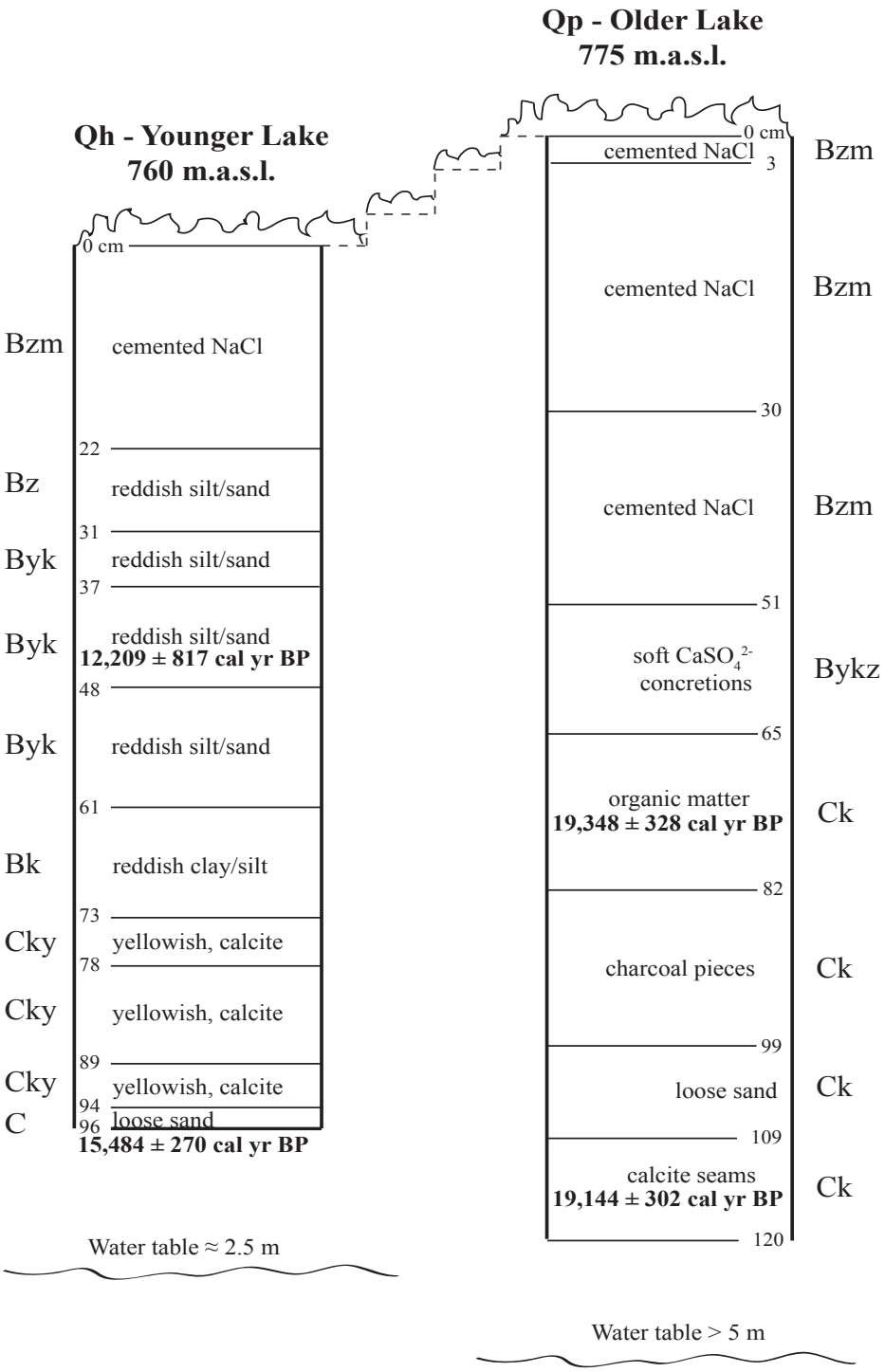

Figure 4. Soil profiles from the Qh (younger) and Qp (older) sites. Soil features were identified and described using methods outlined in the USDA Soil Survey Manual (Soil Survey Staff, 1999) and both are classified as Gypsic Haplosalids. The water table at the Qh site was visible in a nearby backhoe trench at ~2.5 m. At the Qp site, the water table is believed to be > 5 m. Radiocarbon dating details can be found in Table 1.

Sample	Horizon	Depth	Na^+	K^+	Ca^{2+}	Cl^-	SO_4^{2-}	Cl	S	C	Al_2O_3	Fe_2O_3	SiO_2	TiO_2	CaO	K_2O	MgO	Na_2O	As	Se	Mo
		cm	mmol / g	mmol / g	mmol / g	mmol / g	mmol / g	wt%	wt%	wt%	wt%	wt%	wt%	wt%	wt%	wt%	wt%	wt%	ppm	ppm	ppm
			Water extracts					Total chemistry													
Qh 1	Bzm	0-22	9.30	0.16	1.43	7.91	3.07	31.50	1.89	0.04	2.26	0.82	8.03	0.09	4.68	1.61	1.35	38.40	98.0	1.5	96
Qh 2	Bz	22-31	4.73	0.07	1.77	1.08	4.46	2.53	14.45	0.13	4.70	1.82	15.60	0.18	16.10	1.23	2.33	14.05	>250	0.7	87
Qh 3	Byk1	31-37	0.14	0.02	2.62	0.15	3.38	0.50	14.20	0.48	5.60	2.18	17.60	0.21	27.30	1.32	1.67	1.68	190.0	0.7	9
Qh 4	Byk2	37-48	0.05	0.02	2.60	0.06	3.10	0.12	16.25	0.37	4.11	1.60	13.05	0.15	30.70	0.94	1.24	0.54	146.5	0.5	2
Qh 5	Byk3	48-61	0.01	0.02	1.45	0.02	1.68	0.04	6.30	0.38	12.60	4.81	38.30	0.50	12.75	2.65	2.26	0.95	171.0	0.5	3
Qh 6	Bk	61-73	0.00	0.02	0.17	0.03	0.28	0.03	0.77	1.31	15.60	6.11	49.90	0.63	7.72	3.21	2.73	1.22	171.5	0.7	6
Qh 7	Cky1	73-78	0.00	0.00	2.68	0.01	3.19	0.02	15.90	2.40	1.34	0.62	5.39	0.05	40.10	0.30	0.76	0.19	143.5	0.6	3
Qh 8	Cky2	78-89	0.00	0.00	2.70	0.01	3.21	0.02	17.00	2.21	0.66	0.31	3.34	0.03	40.60	0.15	0.64	0.12	95.7	0.4	2
Qh 9	Cky3	89-94	0.00	0.00	2.61	0.01	3.08	0.03	14.50	0.96	3.92	1.49	18.50	0.18	30.50	0.75	0.86	0.74	95.2	0.5	7
Qh 10	C	94-96	0.00	0.01	1.30	0.03	1.51	0.03	4.72	0.14	11.55	4.13	53.00	0.56	9.75	2.30	1.54	1.69	91.6	0.6	5
Qp 1	Bzm1	0-3	7.06	0.00	0.12	8.09	0.23	15.60	0.36	0.25	9.35	2.30	49.60	0.30	3.49	1.81	0.77	16.35	21.8	1.9	5
Qp 2	Bzm2	3-30	10.64	0.07	0.07	9.06	1.07	29.40	1.44	0.32	5.56	1.87	19.45	0.22	2.02	1.34	0.82	33.30	15.7	3.4	15
Qp 3	Bzm3	30-51	16.76	0.04	0.11	11.27	0.99	18.35	1.61	0.35	7.84	2.58	33.40	0.31	2.67	1.73	0.98	23.30	20.8	2.7	12
Qp 4	Bykz	51-65	4.98	0.01	0.11	0.66	2.46	1.21	6.77	0.55	10.85	3.81	38.20	0.44	3.26	1.97	1.66	14.85	29.5	1.4	5
Qp 5	Ck1	65-82	1.15	0.00	0.05	0.80	0.55	1.40	1.57	0.76	14.30	5.05	52.30	0.63	4.67	2.31	2.06	6.06	32.2	1.2	6
Qp 6	Ck2	82-99	0.99	0.00	0.16	0.54	0.62	0.87	1.86	0.61	13.85	4.70	55.60	0.57	4.89	2.53	1.92	5.37	34.4	1.2	7
Qp 7	Ck3	99-109	0.24	0.00	0.18	0.22	0.34	0.36	1.01	0.40	12.80	3.31	65.90	0.41	4.17	2.45	1.16	3.90	21.9	0.7	4
Qp 8	Ck4	109-120	0.41	0.00	0.23	0.55	0.41	0.80	1.24	0.61	13.65	4.55	56.80	0.58	5.06	2.52	1.87	3.63	42.8	1.2	7

Table 2. Soil chemistry data from excavations at both sites. Cation and anion concentrations from soil water extracts were measured at UC Berkeley using IC and ICP. Bulk soil major and trace elements concentrations are from ALS Chemex in Reno, NV.

Soil water flux

There are strong water gradients in the upper 1.5 m of both soils as revealed by the RH sensors placed within the excavation pits. It is apparent that the Qh site has a higher water content at all measured depths than the Qp site (Table 3; Fig. 5). The RH sensors show that from 60 cm and below, the Qh soil maintains 100% RH year-round. In comparison, sensors in the Qp soil indicate an average yearly RH of 79% at 58 cm and 87% at 119 cm depths. The RH profiles in both soils are indicative of upward water flow from evaporative removal of groundwater, with a higher rate of evaporation at the Qh site.

	Dec - Feb		**Mar - May**		**Jun - Aug**		**Sep - Nov**		**Entire year**	
	avg T ˚C	avg RH %	avg T ˚C	avg RH %	avg T ˚C	avg RH %	avg T ˚C	avg RH %	avg T ˚C	avg RH %
Qh 2 cm	26	32	21	37	15	47	22	34	20	38
Qh 20 cm	26	68	21	71	16	75	22	72	21	72
Qh 60 cm	24	100	22	100	18	100	21	100	21	100
Qh 98 cm	23	100	22	100	19	100	20	100	21	100
Qp 2 cm	29	25	24	32	18	37	24	25	23	30
Qp 37 cm	26	62	22	65	16	68	22	64	21	65
Qp 58 cm	26	79	23	79	18	79	22	79	22	79
Qp 119 cm	25	87	24	86	20	88	22	88	23	87

Table 3. Average seasonal temperature and relative humidity from within the soil pits. Onset HOBO® Pro v2 (U23-002) sensors were installed at 2, 20, 60, and 98 cm at the Qh site, and at 2, 37, 58, and 119 cm at the Qp site in June 2013 and run for 14 months.

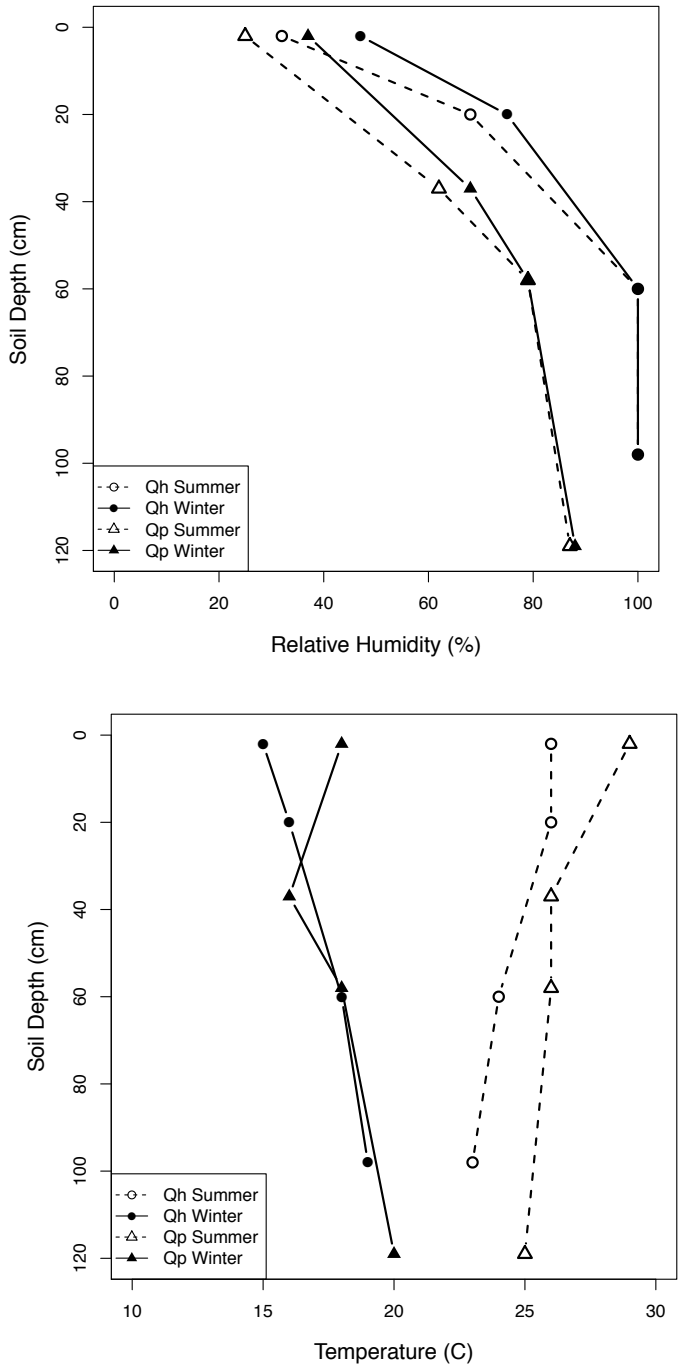

Figure 5. Average relative humidity (a) and temperature (b) profiles in the soil pits from sensors at 2, 20, 60, 98 cm at the Qh site and 2, 37, 58, 119 cm at the Qp site. Summer includes Dec, Jan, and Feb, winter includes Jun, Jul, Aug.

To quantify this, Fick's law was used to calculate the isothermal vertical transport of water vapor in each soil (Bittelli et al., 2008):

$$q'_v = -D_v\left(\frac{dc_v}{dz}\right) \quad \text{(Eq. 1)}$$

where D_v is the vapor diffusivity in soil ($m^2\ s^{-1}$) and c_v is the soil vapor concentration ($g\ m^{-3}$) calculated as

$$c_v = hc'_v \quad \text{(Eq. 2)}$$

where h is the fractional RH and c'_v is the saturation vapor concentration ($g\ m^{-3}$). The average RH values from soil pit sensors over the 14-month monitoring period were used to determine c_v, using Eq. 2 with a c'_v of 17.29 ($g\ m^{-3}$) at 20 ˚C. Calculations for q'_v were done assuming a D_v of 2.39×10^{-5} ($m^2\ s^{-1}$) (Weisbrod and Dragila, 2006). With these parameters, Eq. 1 yielded q'_v values of -0.044 and -0.028 L m^{-2} d^{-1} at the soil-atmosphere interface from the Qh and Qp soils, respectively (Table 4). These estimated flux values are discussed further in the following section.

Site	Soil age	Total Cl deposition	Cl deposition rate	Total water evaporated	Water evaporation rate	dC_v/dz	q'_v
	cal yr B.P.	g m^{-2}	g m^{-2} y^{-1}	L m^{-2}	mm m^{-2} d^{-1}	g m^{-2}	L m^{-2} d^{-1}
	Measured	Calculated from %Cl	Calucated from salt accumluation rates			Calculated from Fick's Law	
Qh	15,484	135,450	8.75	150,500	0.027	21.39	-0.044
Qp	19,348	197,393	10.20	219,325	0.031	13.76	-0.028
Experimental	1.17	536	458	510	1.19	-	-

Table 4. Rates of water evaporation from both soils calculated from Cl accumulation and Fick's Law. Total Cl deposition was calculated assuming a bulk density of 1.50 g cm^{-2} and using total % Cl (Table 2). Rates of Cl deposition was calculated using the max ages from each soil pit (Table 1). Rates of water evaporation were calculated assuming a groundwater Cl concentration of 0.9 g/L as measured from the Qh groundwater and the max ages from each soil pit. Calculations for dC_v/dz were done at z = 0 using gradients of relative humidity from sensors (Table 3), and q'_v was calculated assuming a D_v of 2.39 X 10^{-5} ($m^2\ s^{-1}$) (Weisbrod and Dragila, 2006).

Rates of soil formation and groundwater evaporation

By making inventories of the total salt accumulation divided by the age of the soils, we can estimate the long-term rates of evaporation and associated salt deposition, and compare these values to the estimates made using vapor diffusion above. We use maximum ages of 15,484 and 19,348 cal yr BP for the Qh and Qp sites, respectively, while recognizing that lake/wetland cessation may have occurred much later than when the sediment itself accumulated. Horizon depth and Cl concentration data were used to determine the mass of NaCl in each soil (Table 2). Assuming a bulk density of 1.50 g cm^{-2}, there are 135,450 g Cl m^{-2} at Qh, and 197,393 g Cl m^{-2} at Qp, which is equivalent to 222,550 and 324,758 g NaCl, respectively. These data suggest that the soils have both accumulated NaCl at similar rates over geologic time (~9 g m^{-2} y^{-1} and ~10 g m^{-2} y^{-1}).

It is likely, however, that evaporation rates have not remained constant over time. Kampf et al. (2005) suggested that rates of groundwater evaporation from playas may slow over time as the thickness of the salt crust increases. To test this hypothesis, and to better understand the present dynamics of this environment, we removed (as completely as possible using a jackhammer) an area of the halite crust in the vicinity of site Qh and monitored its renewal over a multi-year period using both time-lapse photography and salt accumulation measurements. After one year a subsample of this newly formed crust was removed and taken back to the lab for analysis. Approximately half of the material was salt, with 0.26 g Cl^- and 0.21g SO_4^{2-} per gram of crust. This very short-term rate of halite accumulation was approximately 458 g m^{-2}, a rate ~38x faster than the estimated geological rate of accumulation.

The Cl^- in the groundwater near the Qh site has a concentration of 0.9 g L^{-1}, 4x higher than a nearby spring at 0.2 g L^{-1} (Magaritz et al., 1989). At the measured concentration of 0.9 g L^{-1}, the evaporation of over 219,000 L m^{-2} of water is required to accumulate the current mass of NaCl at Qp, over 150,000 L m^{-2} of water at Qh, and 510 L m^{-2} at the Qh experimental site. This is equivalent to rates of evaporation of 0.027 mm m^{-2} d^{-1} at the Qh site, 0.031 mm m^{-2} d^{-1} at the Qp site, and 1.19 mm m^{-2} d^{-1} at the experimental site (Table 4). These values are well aligned with the values for water flux calculated using RH gradients and Fick's law in section 4.3. Kampf et al. (2005) reported a range of evaporation rates from the Salar de Atacama in Chile, a salar at a much higher and more inland elevation that the Salar Llamara. Sites with thick salt crusts showed negligible evaporation and were considered to be hydrologically sealed, whereas unvegetated sites with bare soil had evaporation rates of 1 mm d^{-1}. Our results are generally consistent with these rates and their conclusions from the Salar de Atacama data that show that evaporation rates are time dependent.

To better understand the rate and processes of surface crust formation we installed a time-lapse camera to take pictures of the experimental site on a regular basis (Fig. 6). The photo time series visually reveals how rapidly the salt crust can be generated from a relatively thin starting point. The photos shown here are all taken from approximately the same time of day. It is apparent that wetting occurs on a regular basis from fog or dew. Areas impacted by wetting are noted with circles and boxes on the photographs, and appear to be concentrated on relatively higher areas. These areas also appear to show the fastest growth or visual modification. Once an area begins to form a crust, it appears to be preferentially wetted during subsequent fog events, possibly because it is higher off the ground than surrounding areas and/or is purer in NaCl. As time

passes, the amount of surface area that appears wet in each photograph continues to grow. In the final picture, cracks filled with salt are becoming apparent (noted with arrows), with fresh salt deposits evident by the bright white color.

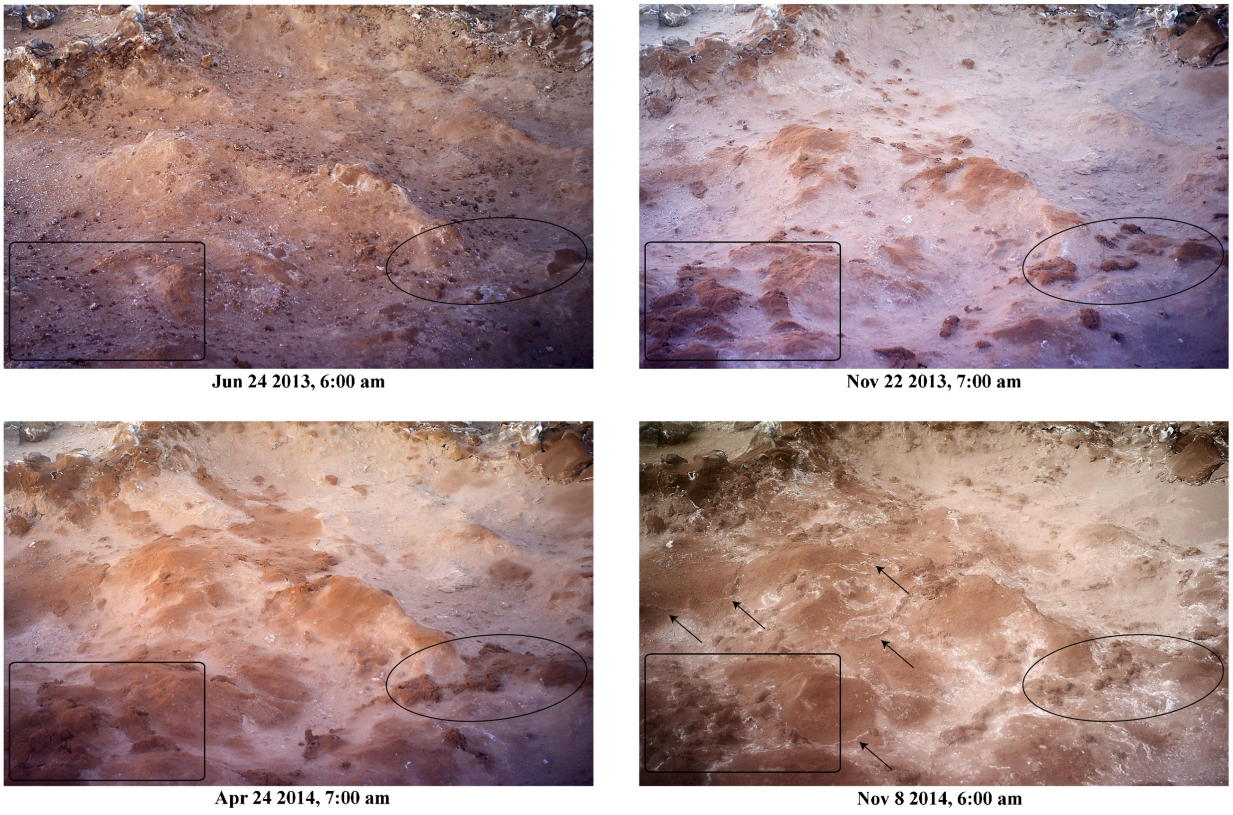

Figure 6. Selected images from time-lapse camera placed at Qh experimental site. Surface crust was completely removed from a 1.5 m^2 plot in June 2013. Photos were taken hourly for 2 years to record development and regeneration of new material. Locations of fastest growth are indicated with circle/square outlines. Cracks filled with fresh (white) salt are noted with arrows.

Observed and modeled salt profiles

Profiles of salt minerals

The RH profiles in the soils indicate upward transport of water vapor. Evaporative vapor movement and capillary liquid flow are the main mechanisms by which salt moves and precipitates (Ericksen and Salas, 1990). As water moves upward and is removed by evaporation, salts are deposited as their solubility coefficients are exceeded. Carbonates are deposited first, followed by sulfates, and finally halides. This sequence also occurs in well-drained desert soils, but there the water flow is downward and the depth sequence is reversed (Finstad et al., 2014). Water extracts of the soil reflect the pore water chemistry, and reveal the distribution of pore water salts with depth (Fig. 7; Table 2). Both soils have a dense, cemented halite soil horizon on the surface and have decreasing water extractable sodium and chloride concentrations with decreasing depth (halite solubility = 360 g L^{-1}). The maximum extractable sulfate concentration occurs beneath the halite layer. In the Qh soil, soluble sulfate peaks at 22 - 48 and 73 - 94 cm, and soluble calcium concentrations mirrors the sulfate throughout the profile (gypsum solubility = 2.1 g L^{-1}). Soluble sulfate in the Qp soil reaches maximum values at 30 - 65 cm. In this soil, there is a weaker correlation between sulfate and calcium, and soluble calcium is mostly invariant with depth. Sodium is the only soluble cation present in large quantities within the sulfate layer, suggesting that mirabilite ($NaSO_4 \bullet 10H_2O$) may be forming in the Qp soil (mirabilite solubility = 274 g L^{-1}).

Carbonates were observed in the lower segments of the soils. In the Qh soil, carbonate peaks at 61 - 94 cm, with > 2% total carbon in the solid phase, and soluble Ca mirrors this trend, indicating that $CaCO_3$ is the dominant mineral (calcite solubility = 0.05 g L^{-1}). In the Qp soil, carbonate was present in low concentrations (0.3 – 0.8% C) throughout much of the profile, though the highest concentrations are found from 51 - 99 cm (0.6 – 0.8% C). We recognize that not all the carbonate is likely to be pedogenic, since observations of these sediments show that they contain lacustrine carbonate (see section 4.5.4.). Isotopes from all these salts can provide more information on their origin, and provide insights into the transport processes that have emplace them in the soils.

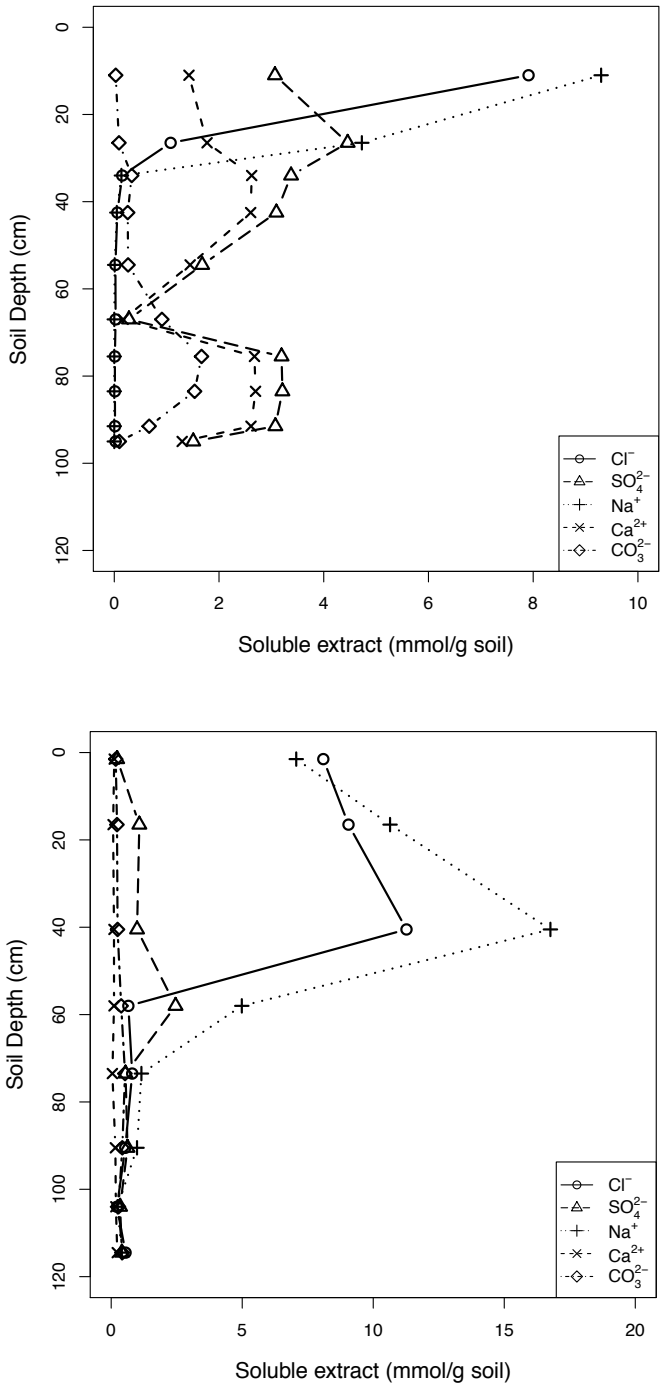

Figure 7. Depth profiles of ions in the Qh soil (a) and Qp soils (b). Chloride and sulfate concentrations in water extracts were analyzed by IC. Sodium and calcium concentrations in water extracted were analyzed by ICP. Carbonate concentrations were calculated from total wt% C data (Table 2).

Sample	Depth	δ^{37}Cl Chlorine	δ^{34}S Sulfate	δ^{34}S Sulfate	δ^{13}C Carbonate	δ^{18}O Carbonate
	(cm)	(‰, SMOC)	(‰, CDT) Measured	(‰, CDT) Modeled	(‰, VPDB)	(‰, VSMOW)
Qh 1	0-22	-	5.13	4.85	-5.29	23.92
Qh 1a	1	-0.34	-	-	-	-
Qh 1a	1	-0.40	-	-	-	-
Qh 1b	6	-0.16	-	-	-	-
Qh 1c	11	-0.27	-	-	-	-
Qh 1d	16	0.27	-	-	-	-
Qh 2	22-31	-	5.71	6.16	-2.48	21.63
Qh 2a	25	-0.12	-	-	-	-
Qh 2b	25	-0.31	-	-	-	-
Qh 2b	30	-0.43	-	-	-	-
Qh 3	31-37	-	6.49	7.09	-1.68	34.33
Qh 4	37-48	-0.57	6.60	7.11	0.35	36.24
Qh 5	48-61	-	7.48	7.73	-0.21	34.44
Qh 6	61-73	-1.44	6.27	9.31	0.61	35.65
Qh 6	61-73	-1.26	-	-	-	-
Qh 7	73-78	-	8.12	8.24	-0.15	35.63
Qh 8	78-89	-0.35	8.10	7.88	1.03	35.43
Qh 9	89-94	-	7.19	8.70	-1.05	33.83
Qh 10	94-96	-	6.63	10.05	-4.71	27.76
Qh GW	~ 2.5 m	0.19	5.54	-	-	-
Qp 1	0-3	-0.18	2.74	-	-3.60	24.85
Qp 1	0-3	-0.29	-	-	-	-
Qp 2	3-30	-	0.72	0.57	-3.42	23.69
Qp 2a	7	-0.46	-	-	-	-
Qp 2b	13	0.56	-	-	-	-
Qp 2c	18	0.12	-	-	-	-
Qp 2d	23	0.63	-	-	-	-
Qp 2e	28	0.79	-	-	-	-
Qp 3	30-51	-	0.15	1.78	-3.01	24.85
Qp 3a	33	-0.42	-	-	-	-
Qp 3a	33	0.01	-	-	-	-
Qp 3b	38	-0.50	-	-	-	-
Qp 4	51-65	-0.05	2.70	2.03	-3.00	24.54
Qp 5	65-82	-	2.19	3.29	-2.55	24.60
Qp 6	82-99	-0.01	2.25	3.40	-2.64	25.10
Qp 6	82-99	-0.06	-	-	-	-
Qp 7	99-109	-	3.24	4.41	-3.48	24.05
Qp 8	109-120	-0.62	4.12	4.29	-3.16	24.40

Table 5. Stable isotope compositions with depth, including δ^{37}Cl and δ^{34}S from the Qh groundwater. δ^{37}Cl and δ^{34}S values are from extracted soil water, δ^{13}C and δ^{18}O are from bulk soil. Subsamples from the Bzm (cemented halite) horizon were included for Cl isotope analysis to capture smaller scale fractionation (~5 cm). Modeled δ^{34}S values were calculated using Rayleigh fractionation following Ewing et al. (2008).

Sulfate stable isotope ratios

The sulfate dissolved in groundwater near the Qh site has a $\delta^{34}S$ value of 5.54‰ (Table 5). Possible sulfate sources to these soils are weathering of Andean volcanic rock and marine inputs. Rech et al. (2003) report that Andean mantle and juvenile rocks have $\delta^{34}S$ values of -5 to +5‰. In contrast, biogenic marine sulfates have $\delta^{34}S$ values of +13 to +22‰, and seawater sulfate a $\delta^{34}S$ value of about +21‰ (Bao et al., 2000). In the region of the soils discussed here, there are large outcrops of Miocene-aged anhydrite that are part of the locally important Soledad formation (Pueyo et al., 2001). This ancient sulfate accumulated at the terminal end of the ancestral Rio Loa, which likely obtained most of its solutes from Andean sources. Thus, the groundwater sulfate we measured appears to largely reflect lithological sources of S.

The $\delta^{34}S$ value of sulfate in both soils generally increases with depth (Fig. 8; Table 5). The weighted average $\delta^{34}S$ value of sulfate in the exposed profiles is 6.47‰ and 1.71‰ for the Qh and Qp sites, respectively. $\delta^{34}S$ values in the Qh soil ranged from 5.1‰ to 8.1‰, and the Qp ranged from 0.2 to 4.1‰. For comparison, both of these soils have $\delta^{34}S$ values within the range reported by Ewing et al. (2008), who studied a soil formed on an alluvial fan south of the Salar Llamara. There, the total soil sulfate averaged 3.7‰, and ranged from 0 to 9.6‰, with values decreasing with increasing depth. The sulfur inputs in that location are from atmospheric deposition, as opposed to the groundwater sources as examined here. However, the similarity in average values between these two studies emphasizes the overwhelming impact of volcanic sulfur on the regional sulfur cycle in the interior of the desert.

The stable S isotope composition of sulfates provides evidence of the direction of solute flow (Amundson et al., 2012; Ewing et al., 2008). Due to small isotopic differences between the dissolved and solid phases of sulfate, combined with the downward migration of remaining soluble sulfate, the S isotope composition of solid phase sulfate tends decrease in the direction of fluid flow, a trend that can be described by a Rayleigh fractionation model. Ewing et al. (2008) were able to apply this model to mimic the S isotope profile of a Pliocene-aged soil formed by the downward migration of infrequent rainfall. The soil displayed a nearly 10‰ decrease in $\delta^{34}S$ values with depth, due to the downward movement of water and the preferential transport of ^{32}S to greater depths over time.

Here, we use this model to determine where these processes apply in the case of upward migrating water and solutes. Following Ewing et al. (2008), sulfate fractionation was calculated using a Rayleigh model (Criss, 1999):

$$\delta_{solid}(z) = \left(\delta_{inputs}(z) + 1000\right) f^{\alpha_{w-s}-1}) - 1000 \quad \text{(Eq. 3)}$$

where $\delta_{solid}(z)$ is the δ value for the solid at depth z, $\delta_{inputs}(z)$ is the δ value of the dissolved inputs at depth z, f is the sulfate inventory at z as a fraction of the total inventory above depth z, and α_{w-s} is the fractionation factor for precipitated sulfate (1.65‰ at 21 °C; Thode and Monster (1965)). $\delta_{inputs}(z)$ was calculated by mass balance:

$$\delta_{inputs}(z+1) = \frac{\delta_{inputs}(z)SO_{4\,inputs}^{2-}(z) - \delta_{solid}(z)SO_{4\,solid}^{2-}(z)}{SO_{4\,diss}^{2-}(z)} \quad \text{(Eq. 4)}$$

where $SO_{4\ inputs}^{2-}(z)$ is the mass of sulfate per area being added, $SO_{4\ solid}^{2-}(z)$ is the mass of sulfate per area precipitated as a solid, and $SO_{4\ diss}^{2-}(z)$ is the mass of sulfate per area remaining in the dissolved phase. Since water movement (and therefore solute transport) is assumed to be rising up through the profile, calculations were performed using the base of the soils at z = 0. The input at z = 0 is the total inventory of salt in the soil and its weighted mean isotopic composition.

The model calculations are compared to the measured $\delta^{34}S$ values in Fig. 8 and Table 5. Both soils show marked decreases in $\delta^{34}S$ values with decreasing depth. The model results mirror the depth trend for the Qp soil, and also closely mimic the $\delta^{34}S$ values of the Qh soil in the upper 55 cm. Below this depth, the model less accurately reflects the $\delta^{34}S$ values. One possible explanation for the divergence from the model at the greater depths is the high and constant soil moisture. The Rayleigh model is based on the assumption that the $\delta^{34}S$ values are driven by repeated deposition and reprecipitation as the soil undergoes wetting and drying cycles. RH sensors indicate that from 50 cm and below, this soil is at 100% RH year-round, which would impede dissolution and reprecipitation.

When the two sites are compared, the greatest difference is that the $\delta^{34}S$ in the Qp soil is approximately 5‰ more negative than that of the Qh. One explanation for this is the different lengths of chemical evolution pathways for the soils (e.g., depth to water table). Sulfate must migrate from much greater depths at the Qp site, and therefore undergoes chemical evolution over a greater distance. Possibly supporting this notion is the observation that the Qp soil has about half the concentration of sulfate as the Qh soil. Alternatively, there could be a slight difference in ground water sources in the basin, but we are unable to test this possibility.

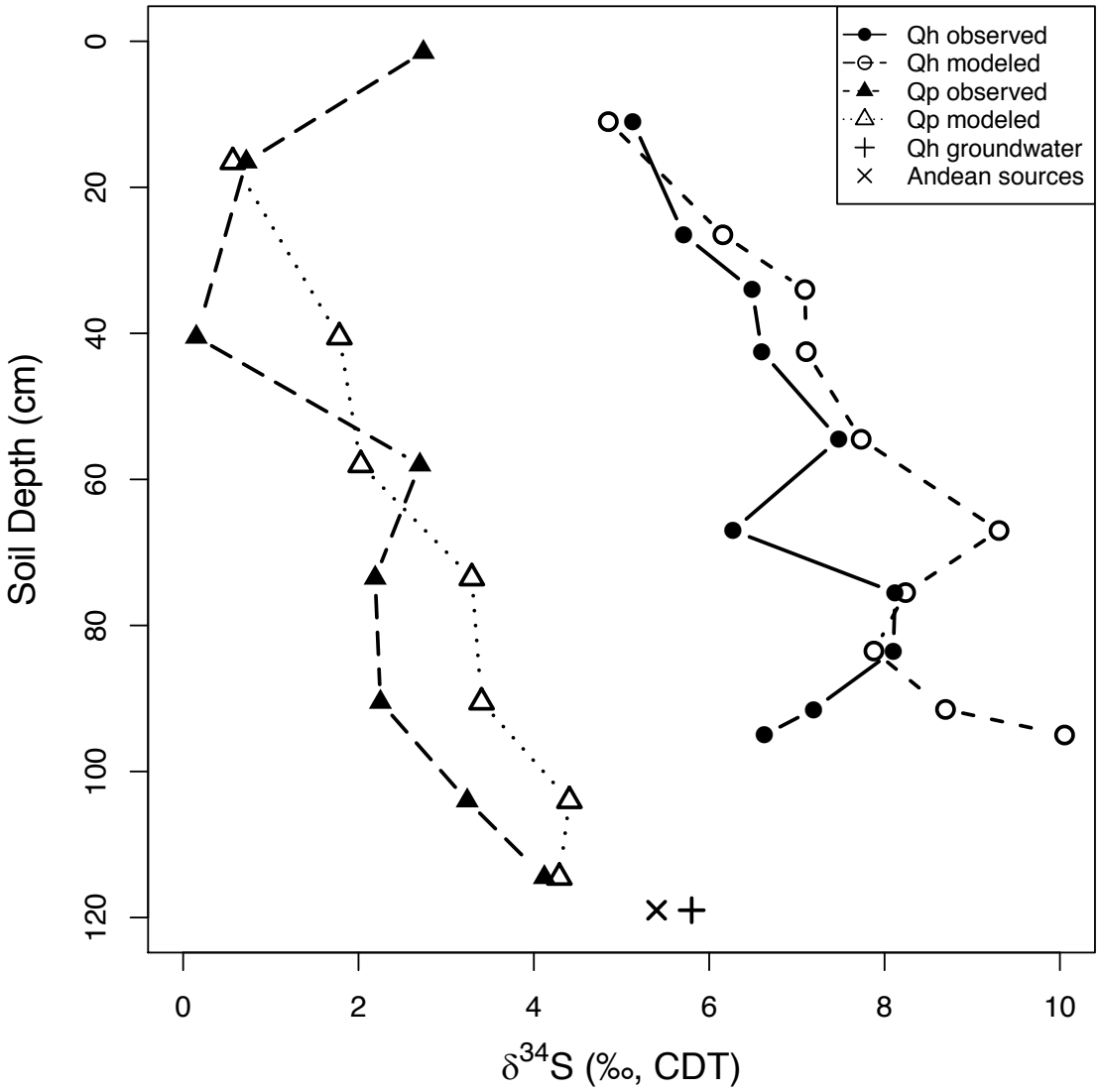

Figure 8. Measured and modeled $\delta^{34}S$ values from extractable sulfate at both sites with depth. A groundwater sample from the Qh site is included, as well as Andean weathering sources from Rech et al. (2003). Modeled values were calculated using Rayleigh fractionation following Ewing et al. (2008). All values are reported relative to CDT.

Chlorine stable isotope ratios

The stable chlorine isotope composition of NaCl provides information on the geologic source of the chlorine and, in certain geochemical settings, information on the mechanism and direction of soil water flow (Amundson et al., 2012). Amundson et al. (2012) found that in a cold desert of Antarctica where brines move along thermal gradients, diffusional movement of chlorine imparts distinctive depth profiles in $\delta^{37}Cl$ values, with δ values decreasing in the opposite direction of advective water flow. In comparison, the authors found that in well-drained soils of warm deserts, brine movement is downward due to rare rainfalls, which appear to cause small fractionations from Rayleigh-like processes. There, the dissolution and reprecipitation of NaCl is identifiable as a consistent decrease in $\delta^{37}Cl$ values with depth (as described above in section 4.5.2). The isotope fractionation factor between NaCl and a saturated solution is 0.26 ± 0.7‰ at 22 ± 2 °C (Eggenkamp et al., 1995). Halite formed from seawater (0.00‰) via equilibrium fractionation is reported to have values ranging from -0.6 to +0.4‰ due to multiple precipitation and dissolution events. Values > 0.4‰ cannot arise from evaporation of seawater and imply an alternative mechanism of formation, such as influx of a non-zero ‰ fluid (Eastoe and Peryt, 1999). The $\delta^{37}Cl$ values of chlorine in the Qh site ranged from -1.4 to 0.3‰, and from -0.6 to 0.8‰ in the Qp soil. The groundwater from the Qh site has a value of 0.19‰ (Fig. 9; Table 5). The weighted average of the chlorine is -0.2‰ and 0.0‰ at the Qh and Qp sites, respectively. Over 90% of the soil chlorine is in the cemented halite layers on the surface of the soils: 22 cm thickness at Qh and 51 cm thickness at Qp (Fig. 7; Table 2).

Given what we know about these sites, key processes that may impact chlorine distribution and isotopic composition include:

1. Long-term net migration of NaCl upwards via capillary rise and evaporation of groundwater. This would be an advective process and should result in little isotopic fractionation.
2. Downward diffusion of chlorine in response to concentration gradients induced by evaporation and deposition of salts higher in the soil profile. Due to differences in diffusivities among isotopologues, this would cause a decrease in $\delta^{37}Cl$ with depth as ^{35}Cl diffuses quicker than ^{37}Cl (Desaulniers et al., 1986).
3. Inputs to the crust from aeolian redistribution of Miocene halite and from sea salt deposition. Given the isotopic similarity between the two sources, it may not be possible to isotopically differentiate these.
4. Repeated dissolution and reprecipitation of the crust driven by deliquescence and efflorescence associated with fog events (section 4.6.). This may cause small spatial scale variations in chlorine isotope ratios. However, detecting this would require precise sampling along presumed growth features, which we did not attempt.
5. Ion filtration in which a negatively charged membrane (e.g., a clay layer) repels Cl^- in an advective flow regime. Because ^{35}Cl has a higher ionic mobility than ^{37}Cl, it tends to become enriched behind the membrane relative to the direction of flow (Phillips and Bentley, 1987). This is likely not a factor for these soils as no significant "membrane" layer is present, and regions of higher Cl concentration are not associated with lower $\delta^{37}Cl$, as would be expected if ion filtration were occurring.

Below ~20 cm, $\delta^{37}Cl$ values decrease 1.3‰ with depth at both sites. Among the five processes listed above, the isotope fractionating process we anticipated to be operable is #2, which should

cause a decrease in $\delta^{37}Cl$ values with increasing depth as a result of chlorine diffusion along concentration gradients in pore water.

In the upper ~10 cm, the $\delta^{37}Cl$ values are nearly identical at -0.30 ± 0.13‰ (n=3) and -0.24 ± 0.08‰ (n=2) at the Qh and Qp sites, respectively. For comparison, two samples from the Salar de Atacama averaged -0.21 ± 0.11‰ (n=4) and -0.13 ± 0.12‰ (n=3), and one sample from the Salar Grande averaged -0.28 ± 0.14‰ (n=2) (Amundson et al., 2012). Given the similarity in all of these values, we hypothesize that the surface crusts receive inputs from both sea salt and recycled Andean material, and become relatively homogenized due to fog water and (very rare) rainwater (processes #3 and #4 above). Below this homogenized and "active" zone, the declining $\delta^{37}Cl$ values with depth are consistent with process #2 above.

Although chlorine isotope research in hyperarid soils is only in its infancy, and the fractionation seen here is modest, the data provide support for two important processes impacting the halite accumulation in salars: (1) dynamic and semi-continuous alteration of the surficial "active" zone of the crusts and (2) a net downward ionic diffusion and isotope fractionation along chlorine concentration gradients.

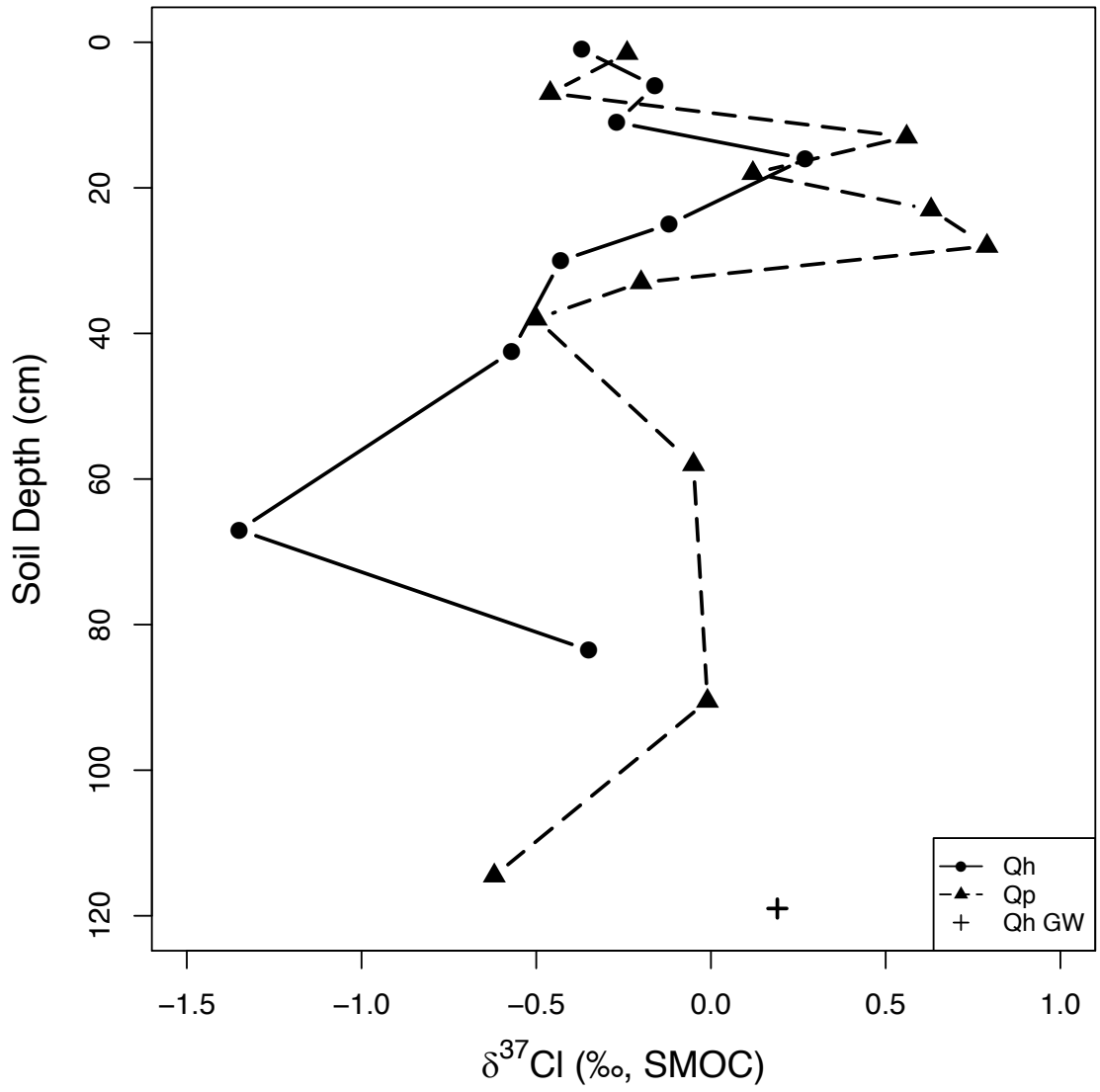

Figure 9. $\delta^{37}Cl$ values of extracted soil water at both sites with depth. A groundwater sample from the Qh site is included and ~5 cm subsamples of the Bzm horizons (cemented halite). All samples are reported relative to SMOC.

Carbonate stable isotope ratios

Well-drained soils in the hyperarid Atacama Desert contain little or no carbonate due to a combination of high sulfate concentrations and low soil pCO_2 levels (Ewing et al., 2006; Quade et al., 2007). In these salar soils, carbonate is present in varying amounts at different depths and between the sites (Fig. 7; Table 2). Since the soils contain little organic matter, we use total %C as a proxy for $\%CO_3$. At site Qp, the %C is fairly constant throughout the profile, ranging from 0.25% to 0.76%. However, at the Qh site the %C is more variable, increasing from 0.04% at the surface to >2% deeper in the profile. The carbonate in these soils is likely derived both from sediment deposition (e.g., fresh water marls), and from pedogenic processes after the drying of the lakes/wetlands. In particular, the large and irregular concentrations of carbonate within the Qh soil are presumed to largely reflect pre-soil forming processes that occurred within the lacustrine/wetland environment. Therefore, much of the carbonate between 37 and 94 cm in the Qh soil is likely lacustrine in origin, unlike the carbonate at the Qp site which may reflect pedogenic processes that occurred after lake drying. This is important when considering the stable isotope composition of the carbonate at the two sites.

When pedogenic carbonates form they incorporate carbon from soil CO_2, which is a mix from both biological and atmospheric sources. The $\delta^{13}C$ value of carbonates therefore can be used to determine the proportion of each source present at the time of formation (Cerling and Quade, 1993). Quade et al. (2007) showed that carbonates that form in the near absence of biological activity have $\delta^{13}C$ values of +4‰, whereas carbonates formed under the influence of plants and microbial processes can attain values as low as -14‰ (Cerling and Quade, 1993).

In the Qh profile, the $\delta^{13}C$ value of carbonate in the surface horizon is -5.29‰, and increases steadily with depth to ~ 0‰ at 37 cm. Values remain constant to 94 cm, and then quickly decline to -5‰ at the base of the soil (Fig. 10; Table 5). There is a very low concentration of carbonate in the surficial halite crust. The surprisingly negative $\delta^{13}C$ values can be attributed to the in situ biological activity of the microbial communities living there, and the associated small amount of carbonate forming in the vicinity of this biological respiration. The remaining carbonate in the Qh profile likely is a variable mix of sedimentary and pedogenically formed minerals.

The $\delta^{13}C$ values of carbonate in the Qp profile average -3.1‰ and vary little with depth. Assuming that the carbon isotopes are derived from diffusing soil CO_2, this reflects steady state $\delta^{13}C$ values of about -17.5‰. The lack of a depth trend in C isotopes may reflect the dense halite cap on the soil, facilitating a very sharp transition between the soil and overlying atmospheric CO_2.

Further insight into the carbonate forming environments can be gained from the $\delta^{18}O$ values. While the $\delta^{13}C$ value of pedogenic carbonate reflects the soil CO_2 at the time of formation, the $\delta^{18}O$ values of the carbonates reflects the $\delta^{18}O$ value of the soil water. Aravena et al. (1989) determined that the $\delta^{18}O$ values of groundwater in the region range from -5.9 to -4‰ and fog water ranges from -2.7 to -1‰. The groundwater largely reflects runoff and subsurface flow derived from rainfall at higher elevations to the east. At both of the Qh and Qp sites, the carbonates at the surface have $\delta^{18}O$ values of ~24‰ SMOW (Fig. 10; Table 5). After accounting for the fractionation between liquid water and carbonates (29.1‰ at 20 °C; Kim and O'Neil

(1997)), the surface carbonate values reflect water sources that have $\delta^{18}O$ values of -4.26‰ and -5.2‰ at the Qh and Qp sites, respectively.

At the Qp site, the $\delta^{18}O$ value is fairly constant and does not change significantly with depth. In contrast, at the Qh site the $\delta^{18}O$ value decreases slightly to +21.6‰ in the layer below the surface, then sharply increases to +34.3‰ at 37 cm. The values remain constant until the base of the soil when they decrease to ~27.8‰. At the Qh site, the $\delta^{13}C$ and $\delta^{18}O$ isotope trends mirror each other with depth. The $\delta^{13}C$ and $\delta^{18}O$ values increase with depth, and the high concentrations of carbonate between ~ 20 - 100 cm are interpreted as reflecting lacustrine origins (Table 2). The very positive $\delta^{18}O$ values reflect formation waters of about ~6‰, which would require considerable evaporation from the present groundwater values. Consistent with this interpretation, the $\delta^{13}C$ values indicate a CO_2 source of ~ -9 to -10‰, which indicates a low percentage of biologically processed CO_2. In general, for the Qh soil, we interpret the upper three layers have experienced varying degrees of alteration or pedogenic carbonate formation – with the surface layer especially reflecting in situ isotopic signatures derived from the biotic-rich halite crust. The carbonate-rich layers from ~40 - 90 cm, due to the high carbonate concentrations and the highly enriched $\delta^{13}C$ and $\delta^{18}O$ values, appear to reflect formation in a highly evaporated lake setting. The $\delta^{18}O$ values in Qp are all consistent with unevaporated groundwater, and the $\delta^{13}C$ values reflect a CO_2 source of about -12 to -13‰.

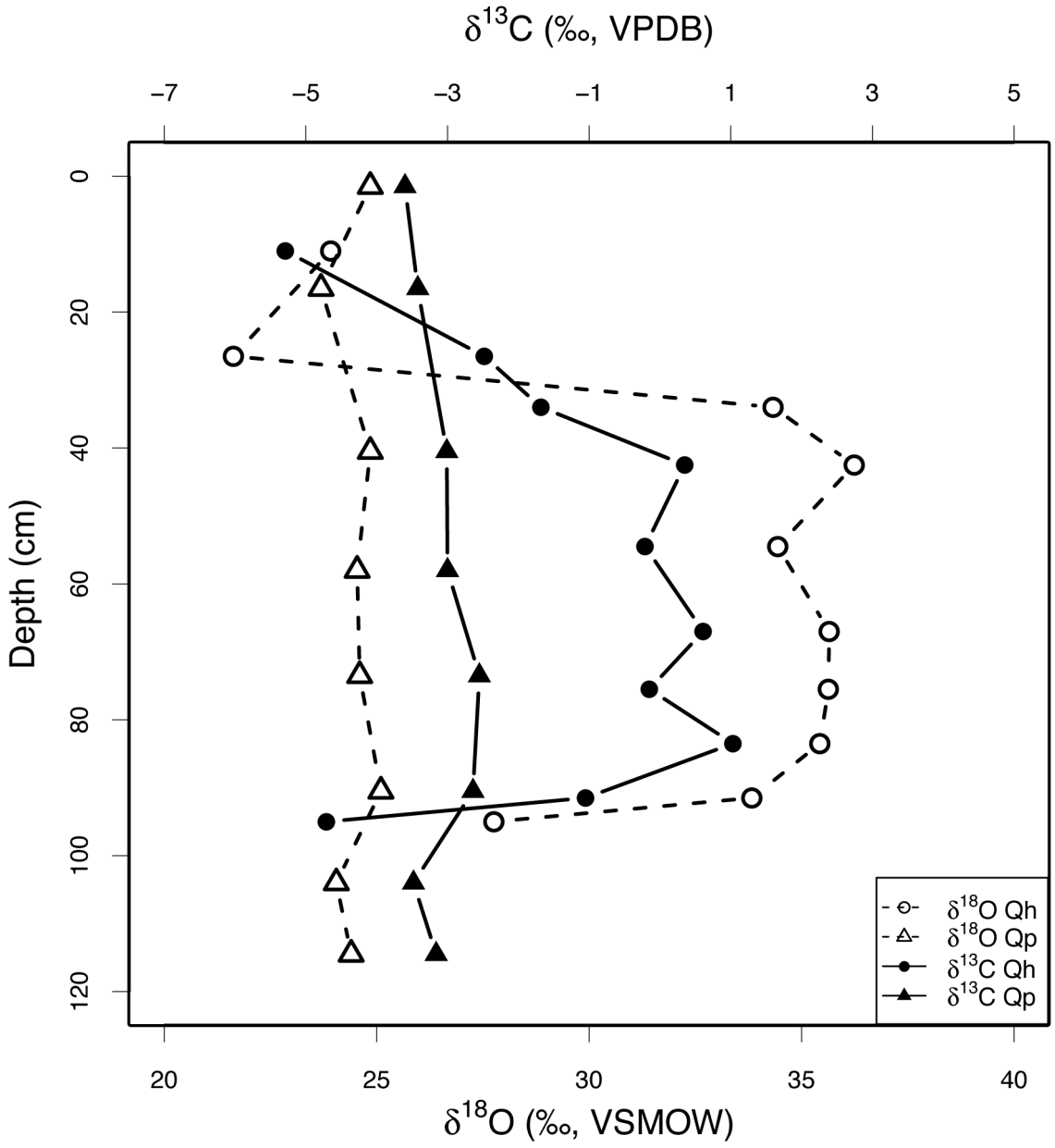

Figure 10. $\delta^{13}C$ and $\delta^{18}O$ values of carbonates at both sites with depth. $\delta^{13}C$ (top axis) is reported relative to VPDB and $\delta^{18}O$ (bottom axis) is reported relative to VSMOW.

Trace metal concentrations

Both the Qh and Qp soils have high levels of arsenic, selenium, and molybdenum, with ranges of 21 – 250 ppm, 0.4 – 3.4 ppm, and 2 – 96 ppm, respectively (Table 2). Arsenic is depth invariant in both soils, but found at concentrations 3x greater in the Qh soil than in the Qp soil. Selenium and molybdenum have pronounced increases in concentration near the surface in both soils (within the halite (Bzm) horizons). Selenium concentrations are similar between the two sites, and molybdenum is similar in low levels between the sites, but 6x greater at the surface of Qh than the Qp soil. High concentrations of these metals/metalloids in the regional groundwater and surface water are well documented and linked to volcanic activity (Bhattacharya et al., 2002; Leybourne and Cameron, 2008; Demergasso et al., 2007; Romero et al., 2003). Cameron and Leybourne (2005) studied soils in the northern Atacama Desert and similarly found high levels of arsenic, selenium, and molybdenum and concluded that they are dissolved as anions in the groundwater and are evapo-concentrated in the soils. This process has been known to occur in agricultural evaporation ponds in the San Joaquin Valley of California (Ong et al., 1997). We conclude that this process is also occurring here, concentrating selenium and molybdenum at the surface and arsenic throughout the profiles. Differences in concentrations between the sites are likely due to differences in groundwater concentrations or length of chemical evolution path (depth to groundwater).

Dynamics of salt crust modification and microbial activity

One of the most distinctive features of the salt encrusted landscape of the Atacama Desert is its rugged, and nearly impenetrable, physical nature. Artieda et al. (2015) described the crust morphology and inferred the development pattern of four salars in the Atacama Desert, ranging from salars which receive ample fog and whose crusts are therefore frequently able to deliquesce, to those which do not receive regular fog and do not deliquesce often. One of their "wet" end members was the Salar Llamara, which is described here. Here, we add to this previous work with an in-depth examination of the climatic conditions, both inside and outside the salt crusts, and an assessment of the environment's ability to support microbial life within the crusts.

The crusts in our field areas display desiccation polygons surrounded by halite nodules jutting up from the ground along the polygon cracks (Fig. 11). Though these surfaces are largely sealed, we have shown earlier that the cracks and fissures in the crusts allow upward movement of groundwater. Surface nodules are capable of deliquescing when the RH exceeds 75%, further shaping the hydrology and physical nature of the crusts (Davila et al., 2008). To better understand the frequency of these processes, we examine micrometeorological observations of these landscapes.

Figure 11. Picture of the Qp site illustrating the surface cracking and polygonal shape. Halite nodules are observed surrounding the polygons coming up from the surface cracks.

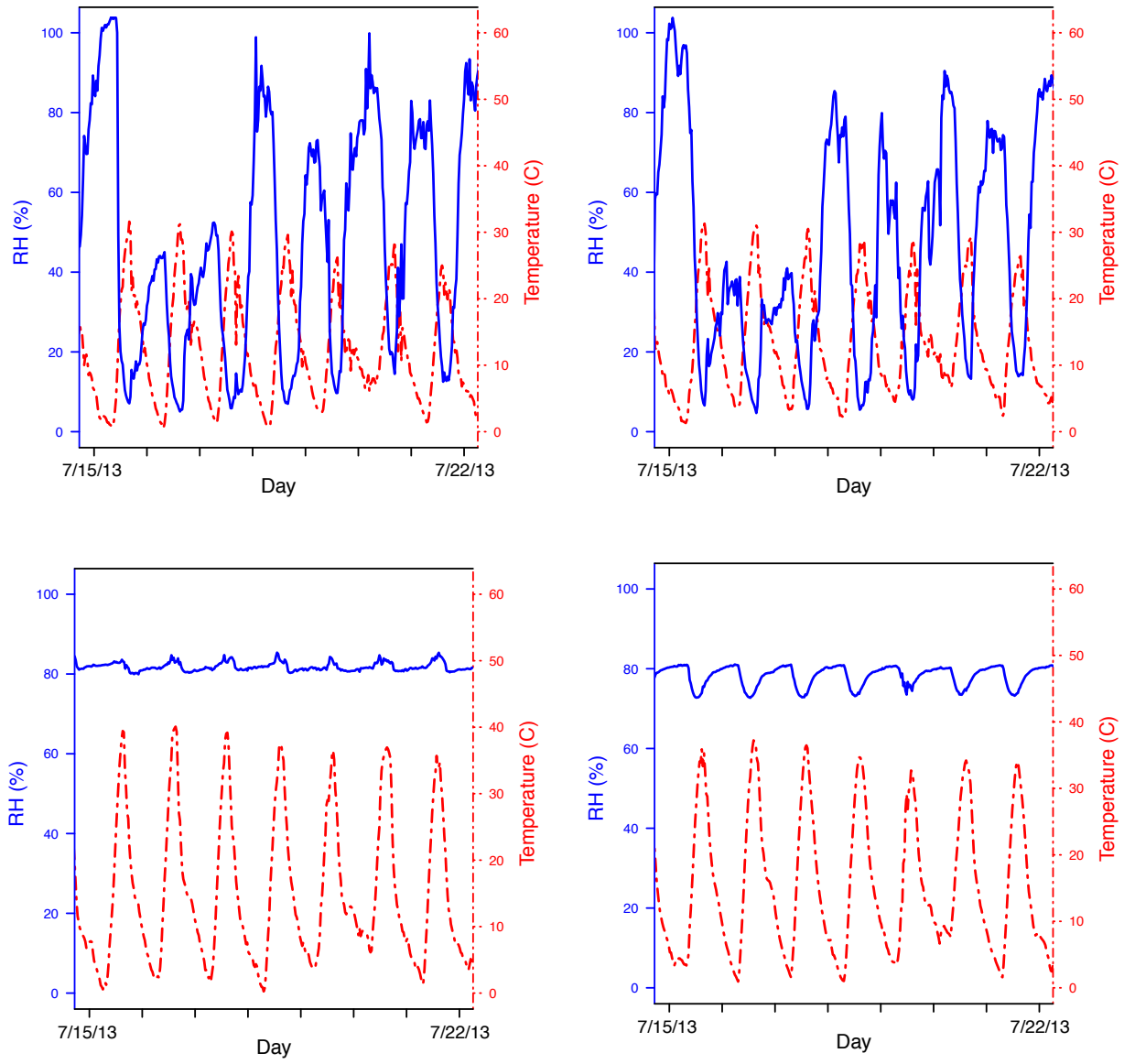

Figure 12. Temperature and relative humidity data for one week in July 2013. Each tick mark on x-axis indicates 24 hrs. Atmospheric conditions from the Qh site (a), atmospheric conditions from Qp site (b), a selected halite nodule from Qh (c), and a selected halite nodule from Qp (d). RH within halite nodules (c and d) remains constant even when atmospheric RH (a and b) are below 50%.

Site meteorological conditions
At the Qp site 14 months of meteorological data were recorded, but at the Qh site the weather station stopped recording T and RH after three months. During the three-month period with overlapping data, both the Qh and the Qp sites had very similar T and RH diurnal cycles. T often varied from 0 - 30 °C over a 24 h period, with the maximum between 1:00 - 3:00 pm and minimum between 5:30 - 8:30 am. RH often fluctuated between 10 - 90%, peaking in the early mornings between 1:00 - 8:30 am, and reaching minimum values between 1:00 - 3:00 pm (Fig. 12).

The T at the two sites does not appear to be significantly different, though there were small differences in the RH. The median RH at the Qh site is 61%, whereas the median RH at the Qp site is 56%. The leaf wetness sensors support the finding that the Qp site is less humid than the Qh on average. It appears from our data that the leaf wetness sensors roughly correlate with sustained atmospheric RH ≥ 75% at T's ranging from 0-7 °C. Over the entire year of observation, the Qh leaf wetness sensor measured 1,567 hours of moisture and the Qp leaf wetness sensor measured 901 hours of moisture (out of a possible 9,504 hours).

Microclimate conditions within the crusts
Previous work has shown that microbial communities are capable of colonizing halite crusts due to liquid water made available during deliquescence (Davila et al., 2013; 2008; Wierzchos et al., 2012). As the RH reaches and exceeds 75%, halite within the salt crusts converts to a liquid brine solution. The sensors installed in the crusts at our sites reveal the duration and temporal patterns of deliquescence. A detailed discussion of the atmospheric conditions can be found in the above section 4.6.1. Briefly, we have concluded that the atmospheres above both the Qh and Qp sites were at or above deliquescence RH (75%) for at least 34% of the year.

Here we focus on the conditions within the crusts, derived from seven T and RH sensors at each site (Fig. 3). Temperature within the crusts at both sites varies on a diurnal cycle from ~ 0 to 40 °C, and there is no significant difference between temperatures at the two sites. The sensors also reveal that the internal crust environment has a RH ≥ 75% for most of the study period (14 months). On average, the sensors at the Qh site were below 75% RH only 19% of the time, while the Qp sensors were below 75% RH only 3% of the time. Fig. 12 illustrates in detail a typical week within the crust during July 2013. Even when the atmospheric RH drops well below 75% the crusts are able to maintain an internal RH ≥ 75%. Wierzchos et al. (2012) similarly found this to be true at their study site, and noted that once a nodule reaches a RH > 75%, it is able to maintain this conditions for prolonged periods of time regardless of the external RH.

Table 6 provides the details of how long each individual sensor was below 75%, and which season this drop in RH occurred. Summer months (Dec – Feb) experienced the most intensive drying out of the crusts at both sites. At the Qh site, fall (Mar – May) and spring (Sep – Nov) experienced similar drops in crust RH, while at the Qp site spring (Sep – Nov) was much drier than fall (Mar – May). The differences between the sites may be due to differences in site metrological conditions or to differences in installation techniques. As discussed in section 3.2, sensors at the Qp site were installed in nodules that were first sectioned using an electric hand saw, while the sensors at the Qh site were installed directly into whole nodules (Fig. 3). We are

unable to definitively determine if this had any effect on the results, though we note that the sensors at the Qp site were placed within a much more dense salt mass than at the Qh site.

Davila et al. (2008) conducted a similar experiment at the Yungay field station located at higher elevations and further inland. In general, fog and the intrusion of marine air is less pronounced there due to its geographical location. They found that the RH within the halite crusts at Yungay were > 75% for only 214 hours during the study year and reported an average atmospheric RH of 37%. Another study in the region by Wierzchos et al. (2012) reported RH > 75% within halite nodules for 3909 hours over the year.

We conclude that the nodules at the Qh and Qp sites are able to strongly buffer diurnal changes in atmospheric RH and almost never fully dry out, unlike some nodules further inland. At our sites in the Salar Llamara, likely only the very outer layers of the nodules undergo daily cycles of deliquescence and efflorescence, though due to the size of our sensors, we were unable to capture these conditions.

Sensor	**Max T (˚C)**	**Avg T (˚C)**	**Min T (˚C)**	**Max RH (%)**	**Avg RH (%)**	**Min RH (%)**	**Hours RH < 75%**	**Timing of RH < 75% events (as a % of all events)**			
	All year						%	Dec - Feb	Mar - May	Jun - Aug	Sep - Nov
Qh 1	48	19	-5	83	77	14	17	36	19	24	20
Qh 2	50	19	-6	79	74	60	33	44	44	2	10
Qh 3	50	19	-6	84	79	35	1	100	0	0	0
Qh 4	48	18	-4	82	76	17	22	46	20	20	15
Qh 5	48	19	-5	81	77	25	15	53	13	22	12
Qh 6	49	19	-6	84	78	21	7	38	16	32	15
Qh 7	48	18	-5	80	74	18	37	45	25	12	19
Qp 1	48	19	-4	82	79	21	2	90	5	0	4
Qp 2	47	19	-4	81	77	20	8	68	23	1	8
Qp 3	49	19	-3	87	80	56	3	72	0	16	11
Qp 4	48	19	-4	86	80	75	0	0	0	0	0
Qp 5	49	19	-5	84	79	21	4	61	0	2	37
Qp 6	48	19	-4	82	79	26	3	72	0	0	28
Qp 7	48	19	-4	82	79	21	3	74	6	0	20

Table **6.** Average temperature and relative humidity within the halite nodules. Seven Onset HOBO® Pro v2 (U23-002) sensors were installed at each site. The number of hours recorded with RH < 75% was calculated and are presented as a percent of hours recorded (9504 total). The timing of these RH < 75% events is given by season as percent of the total RH < 75% events. Installation techniques were slightly different at each site (Fig. 2), allowing for measurement deeper within the nodules at the Qp site.

Rates of biological activity and crust formation

The halite crusts contain prominent green pigments from microbial communities (Fig. 13). To gain an understanding of the rate of carbon turnover in these crusts, organic carbon from three halite nodules on the surface at each site was dated. All of the samples from the Qh site are radiocarbon "modern", indicating the accumulation of organic carbon in the past few decades, and active photosynthesis and organic carbon cycling. However at the Qp site, the radiocarbon ages of occluded organic carbon are 2546, 8521, and 1995 cal yr BP (Table 1). This indicates not only that microbial communities appear far less active here with a much slower carbon cycling rate, but also that these nodules (or at least the organic carbon within them) have been on the surface of this playa for well over 2000 years. Though this suggests that at least portions of these salt crusts are highly stable features, there is also ample evidence that shows that some portions of the crusts are physically dynamic and subject to alteration. Wind and water both sculpt and modify the crusts, while evaporation of groundwater likely continues – at least at the Qh site with a thinner crust – to add salt at the crust base and heave the overlying material upward.

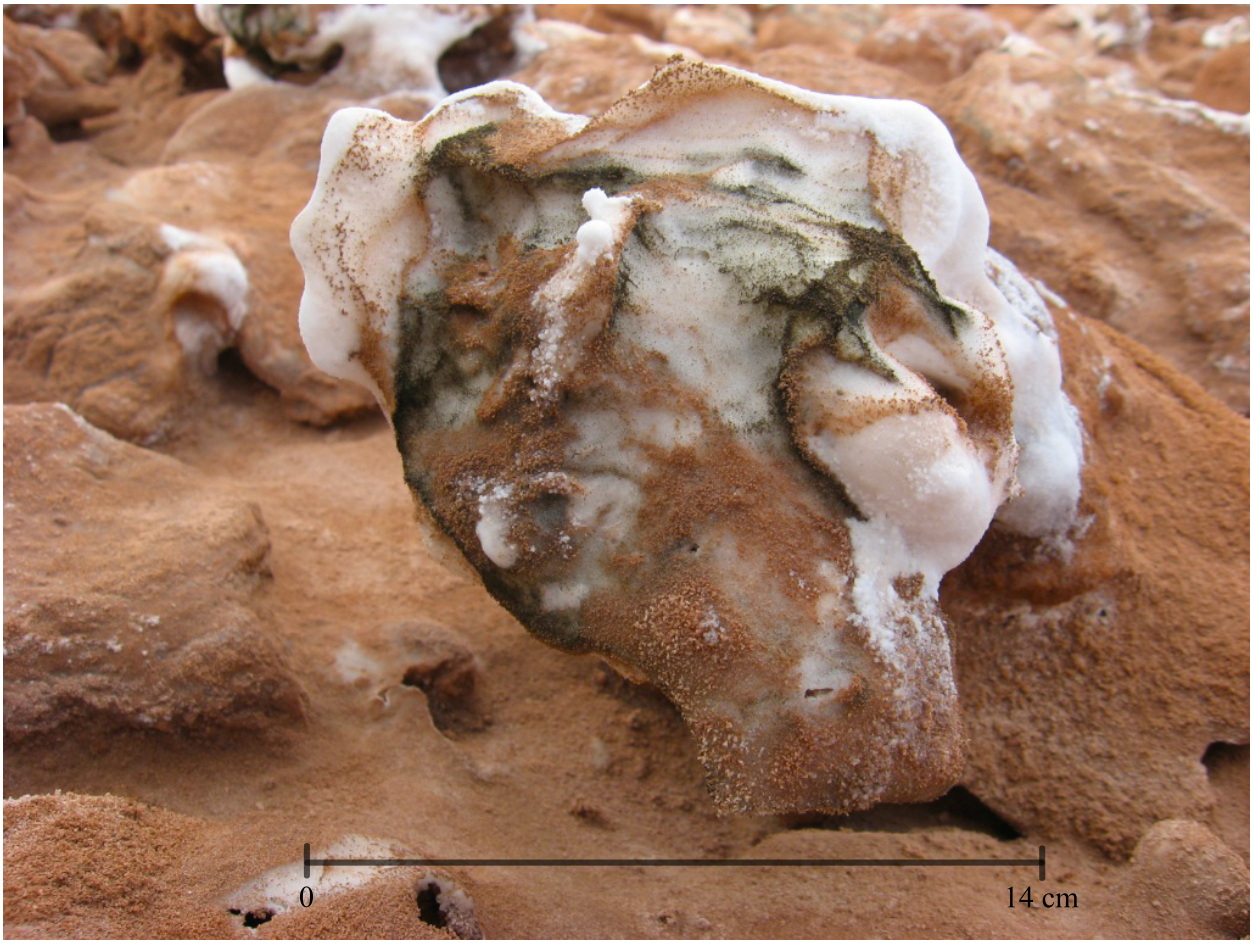

Figure **13.** Halite nodule with visible growth of microbial communities (dark green banding on surface).

Proposed conceptual model of salt crust formation

From our observations we propose the following conceptual model for salt crust formation in this salar. First, lake abandonment due to climate change and/or tectonics leads to the lowering of the water table. Capillary rise from evaporation of shallow groundwater leads to the deposition of salts on the surface of the soil. A solid layer of salt crust eventually forms, and is pushed up and physically modified as salts continue to accumulate. Evaporative stress and thermal drying create cracking polygons, and salts begin to accumulate faster in the regions around the polygon edges. Salts continue to increase and form protrusions around the polygons. These nodules evolve geomorphically as wind and water sculpt them. Simultaneously, atmospheric RH rises beyond a threshold RH for deliquescence within the nodules. This deliquescence provides liquid water available for microbial communities. After reaching a large enough size, the internal environment of the nodules are able to buffer diurnal changes in atmospheric RH, allowing for a sustained habitable microenvironment.

Conclusions

Evaporation of shallow groundwater in salars of the Atacama Desert drives the geochemical evolution of these soils, currently classified as Gypsic Haplosalids. In a previous paper, we suggest taxonomic changes that would classify the soils as Epi Petrosalids, emphasizing both the indurated surface and the relative direction of fluid and surface salt accumulation (Finstad et al., 2014). Rates of evaporation are shown to average ~0.03 mm m^{-2} d^{-1} over geologic time at both sites in this salar. This continuous process leads to the accumulation and growth of salt crusts on the soil surface, which in turn decreases the rate of groundwater evaporation. Rates of evaporation from the experimental plot at the Qh site were observed to be 38x faster than the calculated geologic rate. This upward movement of water and its dissolved solutes produces a salt profile with the most soluble salts on the surface and the least soluble at the base, as salts are deposited as their solubility coefficients are exceeded. This is the opposite trajectory observed in other desert soils and well-drained soils in the Atacama Desert.

Stable isotope ratios of sulfate, chloride, and carbonate were used to infer geochemical processes occurring within the soils. The $\delta^{34}S$ profile from sulfate was consistent with the upward water movement and followed an expected pattern of Rayleigh-like fractionation associated with repeated dissolution and precipitation, concentrating heavier sulfur isotopes at the base and lighter sulfur isotopes near the surface of the soil profiles. $\delta^{37}Cl$ values of soil water indicated that the surface crusts are dynamic and provided evidence for ionic diffusion that counters the upward advective movement of water and solutes. $\delta^{13}C$ and $\delta^{18}O$ values of carbonate suggest that the uppermost halite layers contain surprisingly small amounts of carbonate with a strong biological isotope signature, reflecting the effects of microbial communities within the deliquescing halite. The carbonate-rich layers from ~40 - 90 cm provide evidence for highly evaporitic lake conditions that persisted during the late stages while sediments were accumulating.

This unique pedogenic setting is actively undergoing soil development. Unlike other playas that undergo cycles of wetting and drying, the Salar Llamara has experienced continuous evaporation since the final stages of lake/marsh drying, as evident by the thick surface salt crust. Evaporation appears to continue to add salt, and modification of the land surface results in a rapid re-

development of crusts by increased rates of evaporation. Despite no recorded rainfall, the internal surface crust environment has a RH at or above deliquesce RH (75%) the majority of the 14-month period of observation. We conclude that these crusts are able to buffer diurnal changes in atmospheric RH and almost never fully dry out, unlike nodules further inland. This maintenance of liquid water results in active microbial communities, and radiocarbon measurements indicate that carbon cycling is occurring at decadal time scales in one of our field areas. The carbon dating also shows that nodules may exist in the salars for well over 2000 years.

References

Allmendinger, R.W., González, G., Yu, J., Hoke, G., Isacks, B., 2005. Trench-parallel shortening in the Northern Chilean Forearc: Tectonic and climatic implications. Geological Society of America Bulletin. 117, 89.

Amundson, R., Barnes, J., Ewing, S.A., Heimsath, A.M., Chong, G., 2012. The stable isotope composition of halite and sulfate of hyperarid soils and its relation to aqueous transport. Geochimica et Cosmochimica Acta. 99, 271–286.

Aravena, R., Suzuki, O., Pollastri, A., 1989. Coastal fog and its relation to groundwater in the IV region of northern Chile. Chemical Geology. 79, 83–91.

Artieda, O., Davila, A.F., Wierzchos, J., Buhler, P., Rodríguez-Ochoa, R., Pueyo, J., Ascaso, C., 2015. Surface evolution of salt-encrusted playas under extreme and continued dryness. Earth Surface Processes and Landforms. 40, 1939–1950.

Bao, H., Campbell, D.A., Bockheim, J.G., Thiemens, M., 2000. Origins of Sulphate in Antarctic Dry-Valley Soils as Deduced From Anomalous ^{17}O Compositions. Nature. 407, 499–502.

Barnes, J., Sharp, Z.D., 2006. A Chlorine Isotope Study of DSDP/ODP Serpentinized Ultramafic Rocks: Insights Into the Serpentinization Process. Chemical Geology. 228, 246–265.

Bhattacharya, P., Frisbie, S.H., Smith, E., Naidu, R., Jacks, G., Sarkar, B., 2002. Arsenic in the environment: a global perspective, in: Sarkar, B. (Ed.), Handbook of Heavy Metals in the Environment. Marcell Dekker Inc, New York, pp. 147–215.

Bittelli, M., Ventura, F., Campbell, G.S., Snyder, R.L., Gallegati, F., Pisa, P.R., 2008. Coupling of heat, water vapor, and liquid water fluxes to compute evaporation in bare soils. Journal of Hydrology. 362, 191–205.

Boschetti, T., Cortecci, G., Barbieri, M., Mussi, M., 2007. New and past geochemical data on fresh to brine waters of the Salar de Atacama and Andean Altiplano, northern Chile. Geofluids. 7, 33–50.

Cameron, E.M., Leybourne, M., 2005. Relationship between groundwater chemistry and soil geochemical anomalies at the Spence copper porphyry deposit, Chile. Geochemistry - Exploration, Environment, Analysis. 5, 135–145.

Cerling, T., Quade, J., 1993. Stable Carbon and Oxygen Isotopes in Soil Carbonates, in: Swart, P.K., Lohmann, K.C., McKenzie, J., Savin, S. (Eds.), Climate Change in Continental Isotope Records. American Geophysical Union, Washington, DC, pp. 217–231.

Chong, G., 1984. Die salare in Nordchile — geologie struktur und geochemie. Geotekton. Forsch. 67, 1–146.

Chong, G., Pueyo, J., Demergasso, C., 2000. The borate deposits in Chile. Revista Geologica de Chile. 27, 99–119.

Criss, R.E., 1999. Principles of stable isotope distribution. Oxford University Press, pp. 1 – 254.

Davila, A.F., Gómez-Silva, B., de los Rios, A., Ascaso, C., Olivares, H., McKay, C.P.,

Wierzchos, J., 2008. Facilitation of Endolithic Microbial Survival in the Hyperarid Core of the Atacama Desert by Mineral Deliquescence. Journal of Geophysical Research. 113, 1–9.
Davila, A.F., Hawes, I., Ascaso, C., Wierzchos, J., 2013. Salt deliquescence drives photosynthesis in the hyperarid Atacama Desert. Environmental Microbiology Reports. 5, 583–587.
Demergasso, C.S., Guillermo, C.D., Lorena, E.G., Mur, J.J.P., Pedros-Alio, C., 2007. Microbial Precipitation of Arsenic Sulfides in Andean Salt Flats. Geomicrobiology Journal. 24, 111–123.
Desaulniers, D.E., Kaufmann, R.S., Cherry, J.A., 1986. ^{37}Cl-^{35}Cl variations in a diffusion controlled groundwater system. Geochimica et Cosmochimica Acta. 50, 1757–1764.
Eastoe, C.J., Peryt, T.M., 1999. Stable Chlorine Isotope Evidence for Non-Marine Chloride in Badenian Evaporites, Carpathian Mountain Region. Terra Nova. 118–123.
Eggenkamp, H.G.M., 1994. The geochemistry of chlorine isotopes. Ph.D. Thesis. Universiteit Utrecht, pp. 1-151.
Eggenkamp, H.G.M., Kreulen, R., Koster Van Groos, A.F., 1995. Chlorine stable isotope fractionation in evaporites. Geochimica et Cosmochimica Acta. 59, 5169–5175.
Ericksen, G.E., Salas, R.O., 1990. Geology and Resources of Salars in the Central Andes, in: Ericksen, G.E., Canas Pinochet, M.T., Reinemund, J.A. (Eds.), Geology of the Andes and Its Relation to Hydrocarbon and Mineral Resources. Circum-Pacific Council for Energy and Mineral Resources, Houston, Texas, pp. 151–164.
Ewing, S.A., Sutter, B., Owen, J., Nishiizumi, K., Sharp, W., Cliff, S.S., Perry, K., Dietrich, W., McKay, C.P., Amundson, R., 2006. A threshold in soil formation at Earth's arid–hyperarid transition. Geochimica et Cosmochimica Acta. 70, 5293–5322.
Ewing, S.A., Yang, W., DePaolo, D.J., Michalski, G., Kendall, C., Stewart, B.W., Thiemens, M., Amundson, R., 2008. Non-biological fractionation of stable Ca isotopes in soils of the Atacama Desert, Chile. Geochimica et Cosmochimica Acta. 72, 1096–1110.
Finstad, K., Pfeiffer, M., Amundson, R., 2014. Hyperarid Soils and the Soil Taxonomy. Soil Science Society of America Journal. 78, 1845–1851.
Gayo, E.M., Latorre, C., Jordan, T.E., Nester, P.L., Estay, S.A., Ojeda, K.F., Santoro, C.M., 2012. Late Quaternary hydrological and ecological changes in the hyperarid core of the northern Atacama Desert (~21°S). Earth-Science Reviews. 113, 120–140.
Hogg, A., Hua, Q., Blackwell, P., Niu, M., Buck, C., Guilderson, T., Heaton, T., Palmer, J., Reimer, P., Reimer, R., Turney, C., Zimmerman, S., 2013. SHCAL13 southern hemisphere calibration, 0–50,000 years cal bp. Radiocarbon. 55, 1889–1903.
Houston, J., 2006. Evaporation in the Atacama Desert: An empirical study of spatio-temporal variations and their causes. Journal of Hydrology. 330, 402–412.
Hua, Q., Barbetti, M., Rakowski, A., 2013. Atmospheric radiocarbon for the period 1950–2010. Radiocarbon. 55, 2059–2072.
Jordan, T.E., Kirk-Lawlor, N.E., Blanco, N.P., Rech, J.A., Cosentino, N.J., 2014. Landscape modification in response to repeated onset of hyperarid paleoclimate states since 14 Ma, Atacama Desert, Chile. Geological Society of America Bulletin. 126, 1016–1046.
Kampf, S.K., Tyler, S.W., Ortiz, C.A., Muñoz, J.F., Adkins, P.L., 2005. Evaporation and land surface energy budget at the Salar de Atacama, Northern Chile. Journal of Hydrology. 310, 236–252.
Kim, S.T., O'Neil, J.R., 1997. Equilibrium and nonequilibrium oxygen isotope effects in synthetic carbonates. Geochimica et Cosmochimica Acta. 61, 3461–3475.

Leybourne, M.I., Cameron, E.M., 2008. Source, transport, and fate of rhenium, selenium, molybdenum, arsenic, and copper in groundwater associated with porphyry–Cu deposits, Atacama Desert, Chile. Chemical Geology. 247, 208–228.
Lowenstein, T.K., Hardie, L., 1985. Criteria for the recognition of salt-pan evaporites. Sedimentology. 32, 627–644.
Magaritz, M., Aravena, R., Peña, H., Suzuki, O., Grilli, A., 1989. Water chemistry and isotope study of streams and springs in northern Chile. Journal of Hydrology. 108, 323–341.
Michalski, G., Bohlke, J.K., Thiemens, M., 2004. Long term atmospheric deposition as the source of nitrate and other salts in the Atacama Desert, Chile: New evidence from mass-independent oxygen isotopic compositions. Geochimica et Cosmochimica Acta. 68, 4023–4038.
Nester, P.L., Gayo, E.M., Latorre, C., Jordan, T.E., Blanco, N., 2007. Perennial stream discharge in the hyperarid Atacama Desert of northern Chile during the latest Pleistocene. Proceedings of the National Academy of Sciences. 104, 19724–19729.
Ong, C., Herbel, M., Dahlgren, R., Tanji, K., 1997. Trace Element (Se, As, Mo, B) Contamination of Evaporites in Hypersaline Agricultural Evaporation Ponds. Environ. Sci. Technol. 31, 831–836.
Osterloo, M.M., Hamilton, V.E., Banfield, J.F., Glotch, T.D., Baldridge, A.M., Christensen, P.R., Tornabene, L.L., Anderson, F.S., 2008. Chloride-Bearing Materials in the Southern Highlands of Mars. Science. 319, 1651–1654.
Perez-Fodich, A., Reich, M., Alvarez, F., Snyder, G.T., Schoenberg, R., Vargas, G., Muramatsu, Y., Fehn, U., 2014. Climate change and tectonic uplift triggered the formation of the Atacama Desert's giant nitrate deposits. Geology. 42, 251–254.
Phillips, F.M., Bentley, H.W., 1987. Isotopic fractionation during ion filtration: I. Theory. Geochimica et Cosmochimica Acta. 51, 683–695.
Pueyo, J.J., Chong, G., Jensen, A., 2001. Neogene evaporites in desert volcanic environments: Atacama Desert, northern Chile. Sedimentology. 48, 1411–1431.
Quade, J., Rech, J.A., Betancourt, J.L., Latorre, C., Quade, B., Rylander, K.A., Fisher, T., 2008. Paleowetlands and regional climate change in the central Atacama Desert, northern Chile. Quaternary Research. 69, 343–360.
Quade, J., Rech, J.A., Latorre, C., Betancourt, J.L., Gleeson, E., Kalin, M.T.K., 2007. Soils at the hyperarid margin: The isotopic composition of soil carbonate from the Atacama Desert, Northern Chile. Geochimica et Cosmochimica Acta. 71, 3772–3795.
Quezada, A., Vasquez, P., Sepulveda, F., White, N., Tomlinson, A., 2012. Mapa compilación geológica área Quillagua-Salar Grande, Región de Tarapacá.
Rech, J.A., Quade, J., Betancourt, J.L., 2002. Late Quaternary paleohydrology of the central Atacama Desert (lat 22-24 S), Chile. GSA Bulletin. 114, 334–348.
Rech, J.A., Quade, J., Hart, W.S., 2003. Isotopic evidence for the source of Ca and S in soil gypsum, anhydrite and calcite in the Atacama Desert, Chile. Geochimica et Cosmochimica Acta. 67, 575–586.
Romero, L., Alonso, H., Campano, P., Fanfani, L., Cidu, R., Dadea, C., Keegan, T., Thornton, I., Farago, M., 2003. Arsenic enrichment in waters and sediments of the Rio Loa (Second Region, Chile). Applied Geochemistry. 18, 1399–1416.
Saez, A., Cabrera, L., Chong, G., 1999. Late Neogene lacustrine record and palaeogeography in the Quillagua–Llamara basin, Central Andean fore-arc (northern Chile). Palaeogeography, Palaeoclimatology, Palaeoecology. 151, 5–37.

Sharp, Z.D., Barnes, J., Brearley, A.J., Chaussidon, M., Fischer, T.P., Kamenetsky, V.S., 2007. Chlorine isotope homogeneity of the mantle, crust and carbonaceous chondrites. Nature. 446, 1062–1065.
Soil Survey Staff, 1999. Soil Taxonomy: A Basic System of Soil Classification for Making and Interpreting Soil Surveys. 2nd edition. Natural Resources Conservation Service. US Department of Agriculture Handbook 436.
Stoertz, G.E., Ericksen, G.E., 1974. Geology of Salars in Northern Chile. Geological Survey Professional Paper 811.
Stuiver, M., Polach, H., 1977. Reporting of 14C data. Radiocarbon. 19, 355–363.
Thode, H.G., Monster, J., 1965. Sulfur Isotope Geochemistry of Petroleum, Evaporites, and Ancient Seas, American Association of Petroleum Geologists, Memorial 4, 367–377.
Vogel, J.S., Southon, J.R., Nelson, D.E., Brown, T.A., 1984. Performance of catalytically condensed carbon for use in accelerator mass spectrometry. Nuclear Instruments and Methods in Physics Research. B5, 289–293.
Weisbrod, N., Dragila, M.I., 2006. Potential impact of convective fracture venting on salt-crust buildup and ground-water salinization in arid environments. Journal of Arid Environments. 65, 386–399.
Wierzchos, J., Ascaso, C., McKay, C.P., 2006. Endolithic Cyanobacteria in Halite Rocks from the Hyperarid Core of the Atacama Desert. Astrobiology. 6, 415–422.
Wierzchos, J., Davila, A.F., Sánchez-Almazo, I.M., Hajnos, M., Swieboda, R., Ascaso, C., 2012. Novel water source for endolithic life in the hyperarid core of the Atacama Desert. Biogeosciences. 9, 2275–2286.

Chapter 3:
Halophilic microbial communities along a fog-delivered moisture gradient in the hyperarid Atacama Desert, Chile

Introduction

Microbial life has an amazing ability to survive extreme conditions. Environments once thought to be lifeless are now known to harbor organisms adapted to withstand a variety of physical and chemical challenges (Rothschild and Mancinelli, 2001). The hyperarid Atacama Desert is one such example. Often described as the driest place on Earth, the region receives less than two mm of precipitation annually and was suggested by some to be the dry limit to life on Earth (McKay et al., 2003; Navarro-Gonzalez, 2003; Warren-Rhodes et al., 2006). More recently, relatively vibrant microbial communities have been observed colonizing translucent salt crusts on the surface of evaporitic deposits known as salars (Wierzchos et al., 2006). The key to this microbial habitat is that halite deliquesces at an atmospheric relative humidity greater than 75%, creating a highly saline solution in its mineral pores (Wierzchos et al., 2012). Due to the frequency of marine fog intrusions in the hyperarid region, these salt crusts deliquesce on a regular basis (Cereceda et al., 2008). There is now considerable interest in the microbial community membership and structure of this ultra-dry environment (e.g. de los Ríos et al., 2010; Stivaletta et al., 2012; Robinson et al., 2014; Crits-Christoph et al., 2016), as it offers novel insights into biological adaptations and evolution in a hyperarid and hypersaline environment.

Here, we conduct the most in-depth analysis of the microbial communities in salt crusts of the Atacama Desert to date. Metagenomic techniques are utilized along a spatial gradient at three sites to determine what organisms are present, their metabolic capabilities, and the structure of the microbial communities. Additionally, we discuss how fog-delivered moisture may be influencing community membership.

Methods

Field sites and sample collection

The field sites are halite crusts found within the Salar Llamara of northern Chile. Three sites along a west to east transect are examined here (Fig. 1). The wettest site is 25.5 km from the coast, the intermediate site 44.1 km, and the driest site 54.2 km. At these sites, rugged and dynamic halite crusts have formed due to the interaction of salt with fog. The origin of the salt is either from the evaporation of ground water in late Pleistocene or Holocene dry lake beds (intermediate and driest sites) or from fog reaction with regional Miocene halite deposits (wettest site). Regardless of the salt source, the surface crusts are indistinguishable due to the similar processes that form and maintain them.

Samples were collected in June 2013. At each site, three halite samples were selected from within three 9-m^2 plots positioned 20 - 70 m apart from each other, totaling 9 samples per site. Samples in within the plots were chosen at random and removed from the crust layer using a sterilized rock hammer. Samples were stored in bags at room temperature for ~14 days before reaching the lab at which point they were placed in a -20 °C freezer until processing.

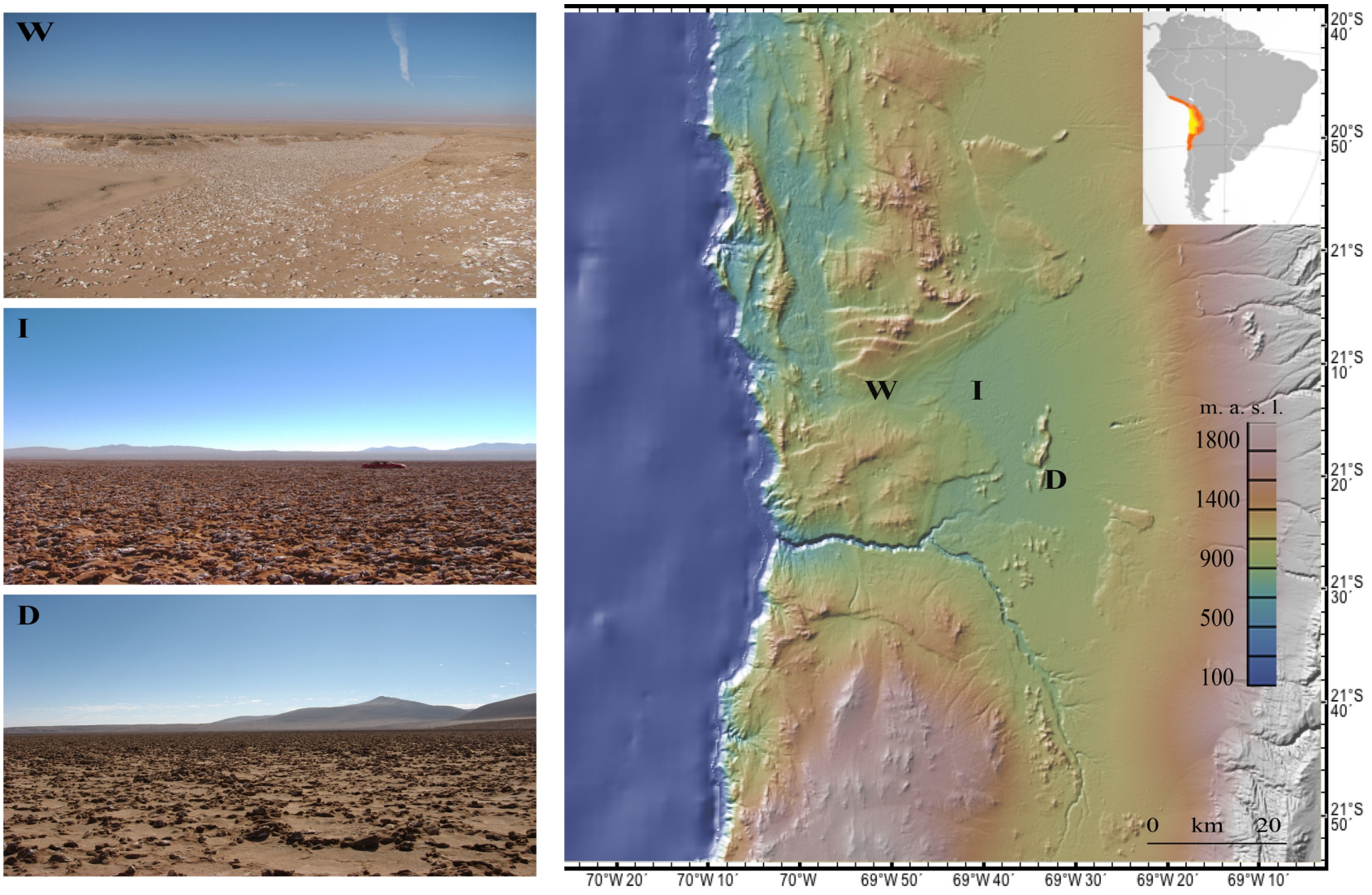

Figure 1. Location of sites within the Salar Llamara basin in northern Chile. Wettest site (W) is 25.5 km from the Pacific coast, the intermediate site (I) is 44.1 km from the coast, and the driest site (D) is 54.2 km from the coast.

A Decagon Devices Inc. leaf wetness sensor was installed at each site in June 2013 and allowed to run for 14 months. The leaf wetness sensors served as a proxy measurement for fog and dew accumulation. Because it did not rain during the year of study, we have assumed that any "wetness" events recorded by the leaf wetness sensor are from dew or fog. A value of 460 counts from the sensor was chosen as the threshold to report wetness, which according to the manufacturer is a conservative value.

DNA extraction and sequencing
Using autoclaved tools, samples were removed from their bag and placed on a sterilized surface. Samples were sectioned in half and 20 g of material from the interior was removed (to ensure no contamination). Samples were dissolved in nuclease-free water in sterile falcon tubes then filtered through 30,000 NMWL centrifugal filters. A MoBio PowerSoil kit was used to extract the DNA from the filter. Extractions were completed within 5 weeks of collection in the field.

The quality of DNA extracted was evaluated using a Nanodrop. All samples had a 260/280 ratio between 1.6 to 2.0. Samples were run in a 1% agarose gel with the DNA Molecular Weight Marker II (0.12 – 23.1 kbp) to screen for DNA degradation. The quantity of DNA extracted was measured using a Qbit 2.0. Sequencing was performed at the UC Berkeley QB3 Sequencing Center. The library size was 600 -1000 base pairs. Samples were run on an Illumina HiSeq2000 with 100 base paired end reads.

Assembly and genome reconstruction
Reads were trimmed and quality checked using SICKLE Version 1.21 (http://github.com/najoshi/sickle) using default parameters then assembled into scaffolds using IDBA_UD (Peng et al., 2012). Open reading frames were predicted using the prodigal software (meta function) (Hyatt et al., 2010). Genomes from metagenomes were binned using differential coverage information as described in Sharon et al. (2013). In brief, coverage of each scaffold was determined by cross-mapping against the entire sample set. Genomes were binned using emergent self-organizing maps (ESOMs with a window size of 3 kb). Genomes were then curated using GC content, coverage information in each single sample, and taxonomic classification of all scaffolds (Wrighton et al., 2012).

De-replication of genomes at species level
In order to determine the abundance patterns of microbial species across samples, the recovered genomes with at least 70% completeness were de-replicated at least 98% nucleotide identity (Probst et al., 2016). If genomes shared more than 50% scaffold identity, they were collapsed and the best representative was chosen based on the number of single copy genes and multiple single copy genes. Only the most complete representative genome was used for further analysis.

Statistical analysis of metagenomics data
Relative abundances of microbial species were determined by cross mapping metagenomic reads onto the de-replicated set of genomes. Reads with more than three mismatches (i.e. less than 98% similarity to the template) were removed from the analysis. Coverage per nucleotide of each genome was determined and then sum normalized across all samples using the total number of reads used for the mapping.

Multivariate analyses of the community data were performed as described in Weinmaier et al. (2015). In brief, community dissimilarities were calculated using the Bray-Curtis index. Community structure was displayed using non-metric multidimensional scaling (NMDS). Abiotic factors influencing the community were elucidated using a BioENV and PERMANOVA (Adonis). A Mantel test was performed (n repeats = 999) with matrices of sample distance based on GPS sampling coordinates and dissimilarities from the Bray-Curtis index.

16S rRNA gene analysis using PhyloChip G3

16S rRNA gene analysis for bacterial and archaeal communities was performed on nine samples, one from each plot at each. In brief, two ng of genomic DNA template were used in each of four tubes for bacterial 16S rRNA gene amplification using primers 27F (5'-AGAGTTTGATCCTGGCTCAG -3') and 1492R (5'- GGTTACCTTGTTACGACTT -3') in a temperature gradient PCR (50-56 °C). Two ng of template were used for archaeal amplifications using primers 4Fa (5' -TCCGGTTGATCCTGCCRG -3') and 1492R.

For amplifications, 25 µL reactions were prepared as follows (final concentrations): 1x Ex Taq Buffer with 2 mM MgCl 2 , 200 nM each primer (27F or 4Fa and 1492R), 200 µM each dNTP (TaKaRa Bio, Inc., through Fisher Scientific, Pittsburg, PA), 25 µg bovine serum albumin (Roche Applied Science, Indianapolis, IN), and 1.25 U Ex Taq (TaKaRa Bio). DNA was amplified using an iCycler (Bio-Rad, Hercules, CA) and the following thermocycling conditions: 95°C for 3 m for initial denaturation, 25 cycles of 95 °C for 30 s, 50, 52, 54, or 56°C (annealing temperature gradient, 4 temperatures per sample) for 30 s, and 72°C for 2 m, and then final extension for 10 m at 72° C. PCR products from the 4-tube annealing temperature gradient for a sample were combined and the total volume was concentrated to 12 µL using a MinElute PCR purification kit (Qiagen, Valencia, CA). One microliter of purified, concentrated PCR product was quantified on a 2% agarose E-gel using the Low Range Quantitative DNA Ladder (Invitrogen, Carlsbad, CA). Samples for PhyloChip analysis were prepared and processed similarly to Brodie et al. (2006), Brodie et al. (2007), and DeSantis et al. (2007). Two hundred fifty ng of bacterial PCR product and 50 ng archaeal PCR product were applied to a G3 PhyloChip TM (Second Genome, South SF, CA) following previously described procedures Hazen et al. (2010). Briefly, the 16S rRNA amplicons and a mix of amplicons at known concentrations (spike-mix) were combined, fragmented using DNAse (Invitrogen, Carlsbad, CA), and biotin-labeled. Labeled products were hybridized overnight at 48 °C and 60 rpm. The arrays were washed, stained, and scanned as described previously. Details on probe selection, probe scoring, data acquisition, and preliminary data analysis are presented elsewhere (Hazen et al., 2010). Data obtained from the CEL files (produced from GeneChip Microarray Analysis Suite, version 5.1) were scaled by setting the spike-mix mean intensity to 4,000 to compensate for slight differences in probe responses on different chips.

Sinfonetta (Second Genome) was used to process the data with the following parameters: Bacterial array Stage1 cutoffs: pf 0.92, min_q1 0.8, min_q2 0.93, min_q3 0.98; post-Stage 2 cutoffs: min_q1 0.22, min_q2 0.40, min_q3 0.42; Archaeal array Stage 1cutoffs: pf 0.01, min_q1 0.5, min_q2 0.93, min_q3 0.98; post-Stage 2 cutoffs: min_q1 0, min_q2 0, min_q3 0.1. Sequences were classified into eOTU (empirically-determined operational taxonomic units) and probe intensities were rank normalized.

Auto-fluorescent cell count

Two to three samples from each site were collected and sectioned into three parts: upper, middle, and lower. A weighed piece of sample from each section was placed in a Falcon tube with a measured volume of water containing 1% TWEEN-20 and stirred for 1 hour. One mL of the solution was then filtered using a Millipore polycarbonate filter and the filter mounted with a drop of mounting oil (Vecta-Shield) on a coverslip. The sample was observed in an Olympus FV1000 confocal microscope, Inverted IX81 microscope with 100x/1.4 oil immersion objective at the Center for Biotechnology at the Universidad Catolica del Norte in Antofagasta, Chile. Samples were illuminated with blue light (<450 nm) and / or green light (<540 nm) and total auto-fluorescent cells were counted in an area of 100 x100 μm.

Radiocarbon measurements

Three halite nodule samples from each site were prepared for radiocarbon analysis by first removing inorganic carbon and excess salts. 20 g of pulverized halite was soaked in 1 M HCl for 24 hours with intermittent shaking to agitate the solution, followed by centrifuging and decanting the acidic supernatant. To ensure complete removal of HCl, the samples underwent alternating soaking and shaking in deionized water for 24 hours, then they were centrifuged and the supernatant discarded. This washing process with deionized water was repeated twice before samples were dried at 60 °C.

Radiocarbon analysis was performed on the Van de Graaff FN accelerator mass spectrometer (AMS) at the Center for Accelerator Mass Spectrometry at Lawrence Livermore National Laboratory, Livermore CA. Approximately 0.5 g of washed sample was prepared for ^{14}C measurement by sealed-tube combustion to CO_2 in the presence of CuO and Ag, and then reduced into iron powder in the presence of H2 at 570 °C (Vogel et al., 1984). $\delta^{13}C$ values were used to correct for fractionation and ^{14}C isotope values are reported in $\Delta^{14}C$ notation and corrected for ^{14}C decay since 1950 (Stuiver and Polach, 1977). Radiocarbon ages were calibrated to calendar year BP using the CALIBomb online program (http://calib.qub.ac.uk/CALIBomb/) with the dataset and extension curve corresponding to our study region (SH_CAL13; SHZ1_2) (Hogg et al., 2013; Hua et al., 2013).

Results

Fog gradient

A leaf wetness sensor was used as a proxy for the presence of dew and/or fog at the sites. The results show that the west site received 3,113 hours of fog, the middle site received 1,560 hours of fog, and the east site received 8,91 hours of fog during the 9,504 hours of monitoring (Fig. 2). This is proportional to fog being present 33%, 16%, and 10% of the time at the sites, respectively, and confirms that the incidence of fog decreases along the west to east transect.

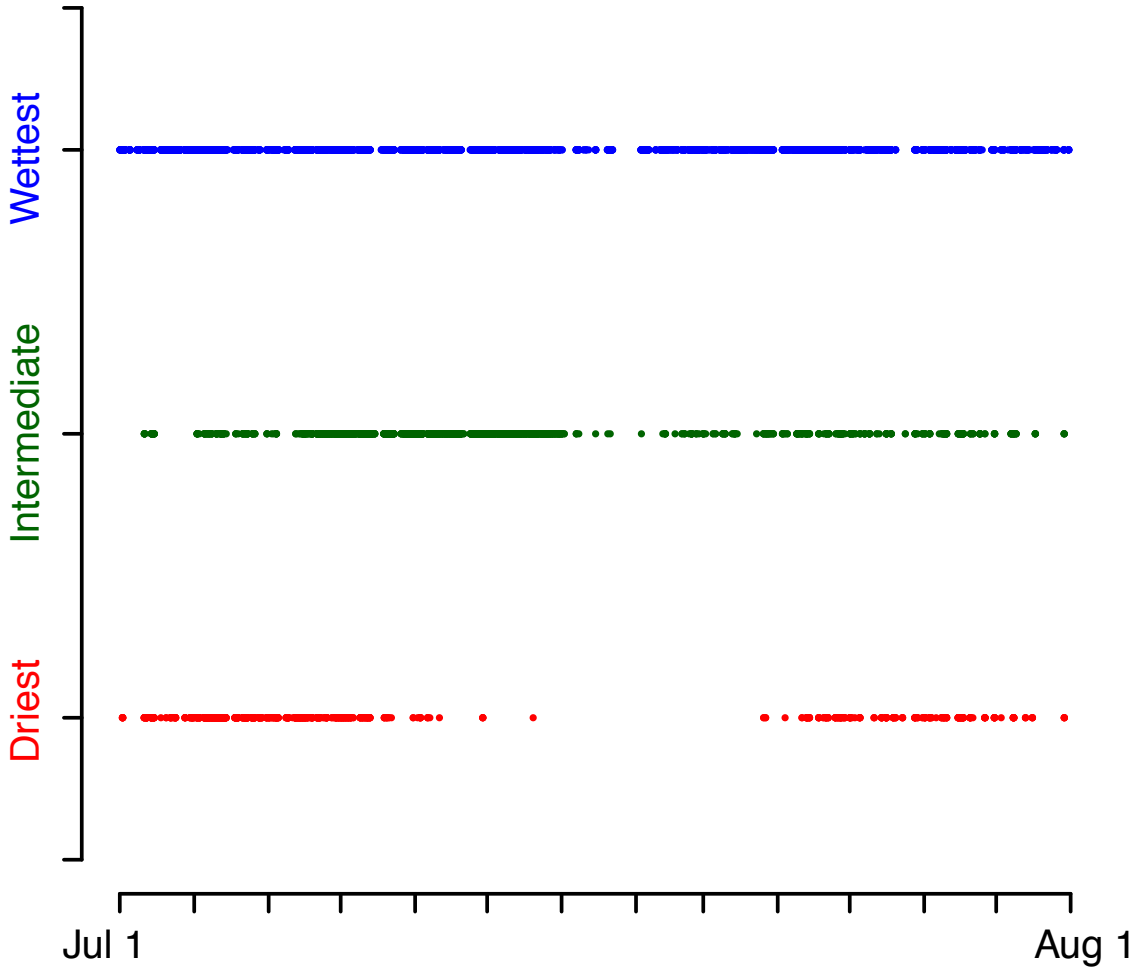

Figure 2. Occurrence of wetness events recorded by the leaf wetness sensors at each site. Each point represents the presence of moisture during a 1-hour interval on the sensor. Samples for microbial community analysis were collected during June 2013, the month before monitoring began.

Community composition

We reconstructed 124 distinct (de-replicated) draft quality genomes (>70% complete, 44 bacteria, 71 archaea), including 53 high quality draft genomes (>90% complete, 18 bacteria and 35 archaea) and one complete genome. 43% of the 10^9 reads from all samples are accounted for by these genomes. In addition, we identified and taxonomically characterized 386 unique 16S rRNA gene sequences from the samples.

At all three sites, communities are comprised of typical halophilic archaea and bacteria as well as some microbial eukaryotes (Fig. 3 and 4). The dominant organisms are Halobacteriales, Salinibacter, and Cyanobacteria. The same genomically-defined cyanobacterial population from the genus Halothece is present in all communities at all sites. Distinct flanking populations of other cyanobacterial populations are also present at the wettest and at the driest sites.

In strong contrast to the low cyanobacterial diversity, the communities show an extremely high variety of halophilic archaeal species, mostly Halobacteriales (Table 1 - 2). We reconstructed 68 draft genomes and identified 226 different 16s rRNA sequences within this group. While there appears to be large overlap across sites in the genomically-defined organisms (66% are found at all sites), all of the 16S rRNA strains of Halobacteriales are restricted to a single sample. Similarly, we reconstructed 34 draft genomes and identified 44 16S rRNA-strains of Bacteroidetes Order II. Incertae sedis, and while 65% of the genomically-characterized organisms were found at all sites, only 1 of the 16S rRNA-defined organisms was.

At lower abundance and to varying degrees, we detected Nanohaloarchaea, OD1, and TM7 in all communities. This is the first report of these Candidate Phyla representatives (OD1 and TM7) in hypersaline environments. Eight 16S rRNA of Nanohaloarchaea were identified and we were able to reconstructed five draft genomes, completely closing one. We reconstructed seven draft genomes of Candidate Phyla Parcubacteria OD1 and identified 15 unique 16s rRNA sequences. Additionally, three draft genomes of Candidate Phyla Saccharibacteria TM7 bacterium were reconstructed. A near-complete genome of a highly novel Thermoplasmatales archaeon was also reconstructed, with the closest identity to Marine Group II. Two 16s rRNA sequence from other closely related strains were detected at the wettest site.

While the majority of the community is composed of bacteria and archaea, we found a low variety of eukaryotes in all samples. A total of 13 strains of the phylum Chlorophyta were identified based on 16S rRNA sequences, and two of these strains were found across all sites. Naegleria gruberi, an amoeba, was found only at the wettest and intermediate sites. We identified nine distinct strains of the amoeba, four found only at the wettest site, three found only at the intermediate site, and two shared between those two sites.

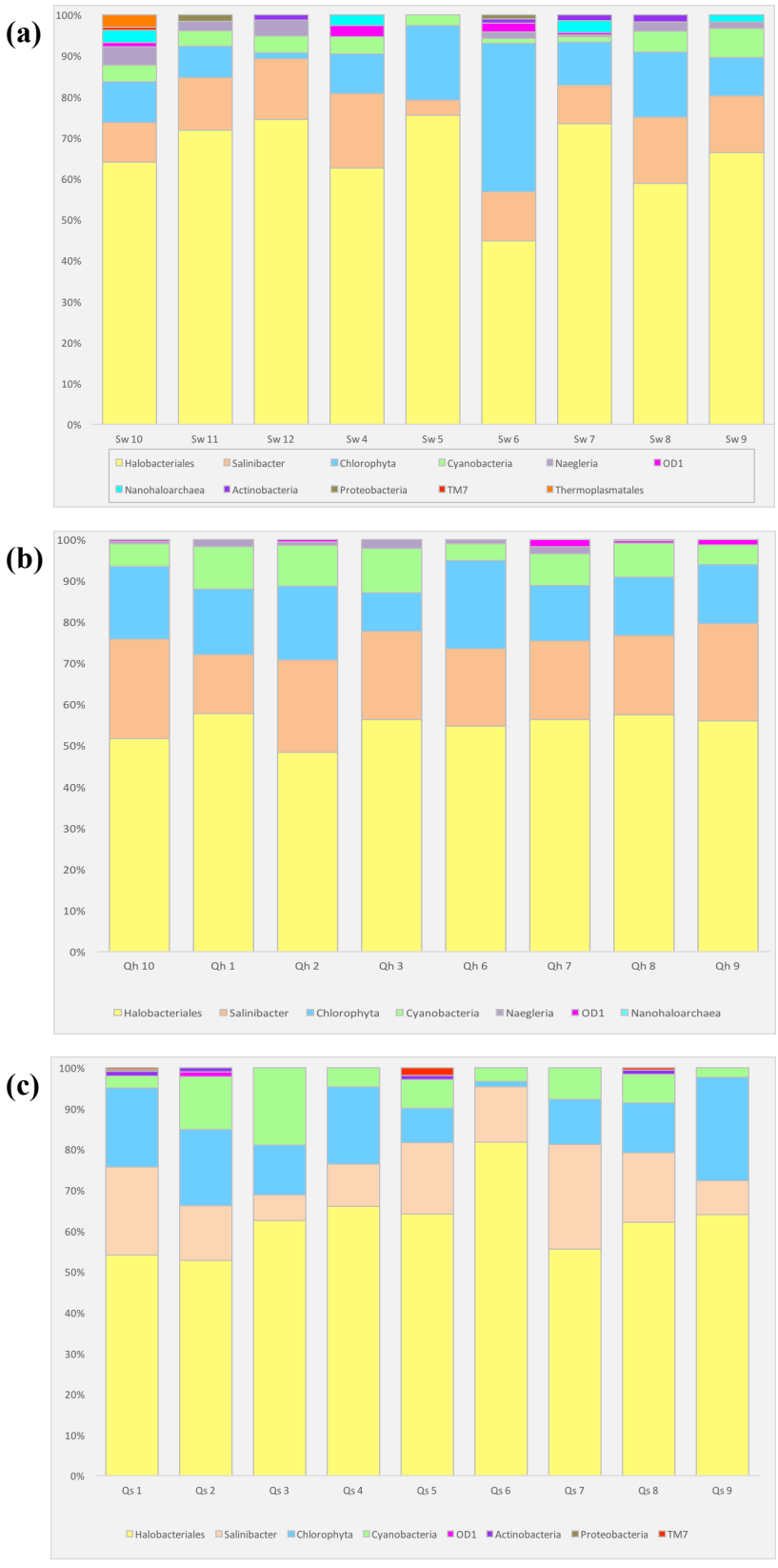

Figure 3. Community composition determined from ribosomal protein S3 coverage for the wettest site (a), intermediate site (b), and driest site (c).

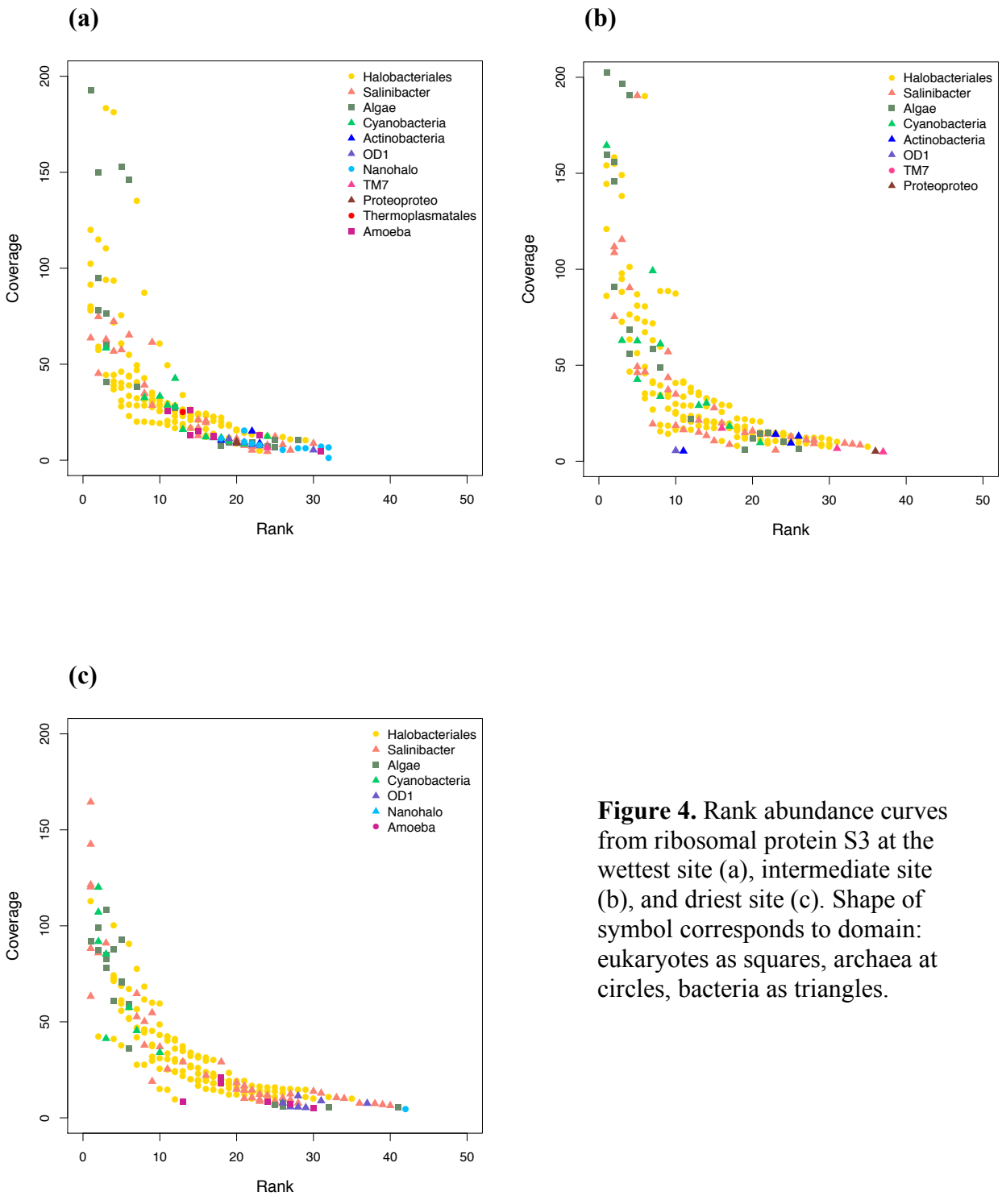

Figure 4. Rank abundance curves from ribosomal protein S3 at the wettest site (a), intermediate site (b), and driest site (c). Shape of symbol corresponds to domain: eukaryotes as squares, archaea at circles, bacteria as triangles.

Group	Total	Wet only	Interm only	Dry only	All sites	Wet & Inter	Inter & Dry	Dry & Wet
Halobacteriales	68	2	1	8	45	11		1
Salinibacter	34	3	2		22	5		2
OD1	7	4	1	1		1		
Actinobacteria	2				2			
Nanohaloarchaea	5	4	1					
Cyanobacteria	3	1		1	1			
Thermoplasmatales	1	1						
Gammaproteobacteria	1					1		
TM7	3			2	1			
All dereplicated genomes	124	15	5	12	71	18	0	3

Table 1. Distribution of genome defined species

Group	Total	Wet only	Interm only	Dry only	All sites	Wet & Inter	Inter & Dry	Dry & Wet
Halobacteriales	226	70	75	81				
Salinibacter	44	15	12	16			1	
Alphaproteobacteria	33	15	12	6				
OD1	15	8	6	1				
Actinobacteria	14	4	5	5				
Algae	13	5	4	2	2			
Amoeba	9	4	3			2		
Nanohaloarchaea	8	6	2					
Deltaproteobacteria	7		5	2				
Cyanobacteria	6	3		2	1			
Thermoplasmatales	3	3						
Gammaproteobacteria	3	3						
TM7	3	1	2					
Planctomycetes	2		2					
All 16S rRNA strains	386	137	128	115	3	2	1	

Table 2. Distribution of 16S rRNA defined species

Clustering of samples

Using the abundance patterns of the 124 genomically defined organisms, we found that microbial communities from different samples at the same site generally cluster together (Fig. 5). In the ordination analyses, samples from the wettest and intermediate sites separate from the driest site along NMDS1 axis (sample Sw 5 is a potential outlier). Additionally, the wettest site formed a separate cluster from samples at the intermediate site along NMDS2 axis.

Communities from samples collected at the intermediate site showed the highest intra-group similarities relative to the other sites. Moreover, each of the three sampling plots at the intermediate site formed individual clusters within this grouping. Samples from the wettest site showed the highest within-site variation and low to no grouping of plots. Samples from the driest site showed a trend for plot-based grouping on either NMDS1 or NMDS2 axis.

Statistical analysis of the PhyloChip data yielded similar results. The principal component analysis (PCoA) shows that samples group together by site, with the intermediate site having the highest within-group similarity (Fig. 6). Along PCoA1 axis, it is apparent that samples from adjacent sites are more similar to each other than samples from opposing ends on the transect (eg. the wettest site is closest to the intermediate site and furthest from the driest site). A hierarchal clustering analysis of the PhyloChip data further confirmed that the samples from within a site are most similar to each other, and that the wettest and intermediate sites are more similar to each other than to samples at the driest site (Fig. 7).

Among the measured abiotic factors, moisture and longitude (distance from the Pacific Ocean) were determined to have the highest correlation with the observed microbial community patterns (BioEnv correlation = 0.58). These two factors were also shown to have a significant influence on the observed dissimilarities of the samples (PERMANOVA p-value <0.001). A Mantel test of the distance between samples and community dissimilarity showed that the spatial distance between samples correlates with the distances of the microbial communities (p-value = 0.001 and observation value = 0.59, based on 999 replicates).

Community activity

To understand the capacity of the communities to sustain growth, a cell count of the photosynthetic organisms was performed. We found that the number of primary producers (cyanobacteria and algae) is greatest at wettest site and declines along the fog gradient (Fig. 8; Table 3). There does not appear to be a consistent trend in the location of cells concentrated in a sample, with the highest counts fluctuating between all three sections (upper, middle, lower). The average cell concentration per gram of sample was 1.53×10^7 at the wettest site, 1.01×10^7 at the intermediate site, and 3.03×10^6 at the driest site.

The radiocarbon content of three samples at the intermediate site and three at the driest site suggests that carbon turnover is occurring more rapidly at the intermediate site (no data was collected for the wettest site). At the intermediate site all of the carbon was found to be "modern", indicating that this organic carbon has accumulated in the past few decades. The age of occluded organic carbon at the driest site gave results of 2546, 8521, and 1995 cal year BP, suggesting a much slower rate of carbon cycling in the system (Table 4).

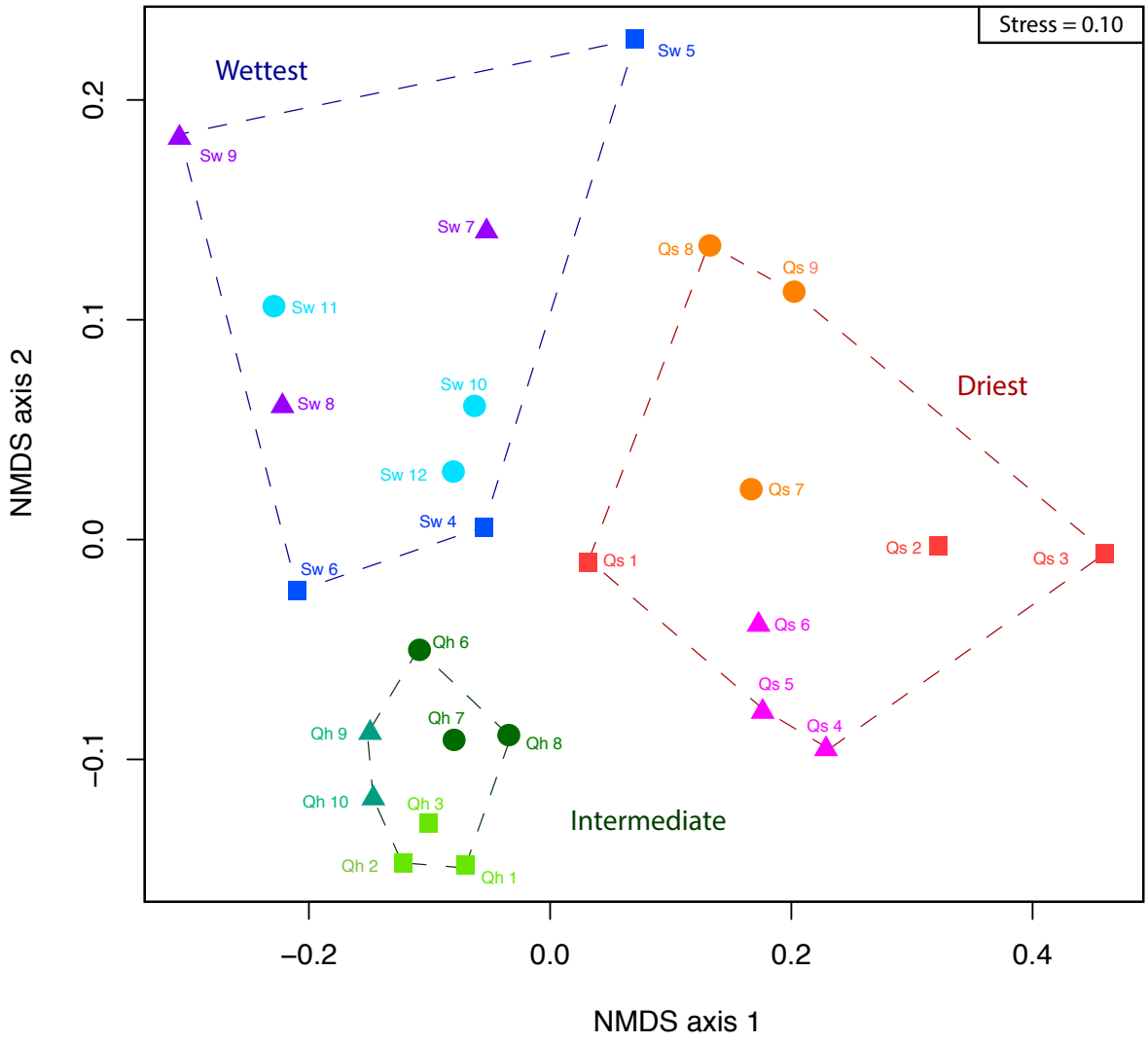

Figure 5. Non-metric multidimensional scaling from community dissimilarities calculated using the Bray-Curtis index of the 124 genome resolved organisms

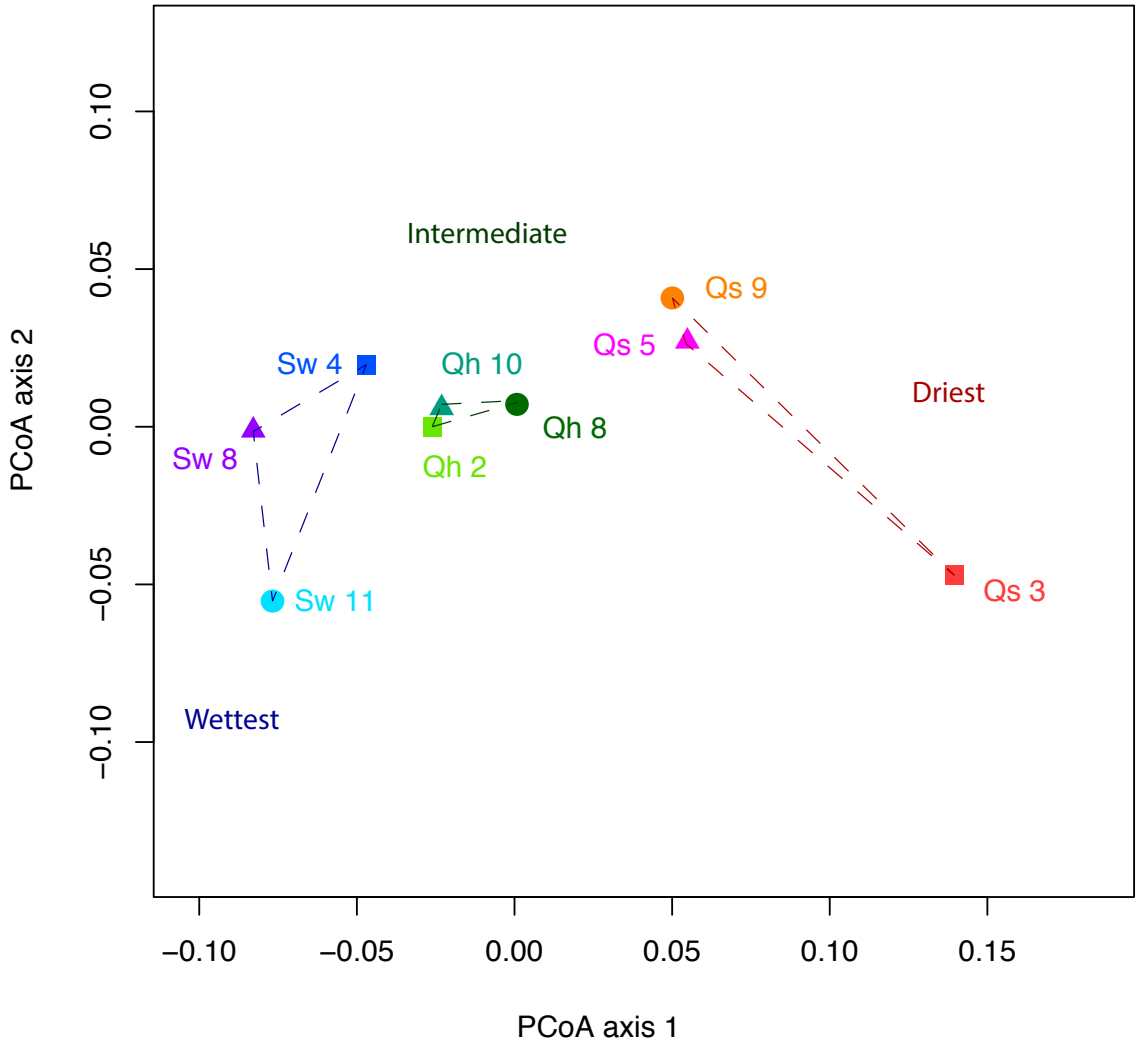

Figure 6. A principal component analysis of the PhyloChip G3 data. This accounts for 86% of the data variance, with an axis 1 value of 0.71 and an axis 2 value of 0.15.

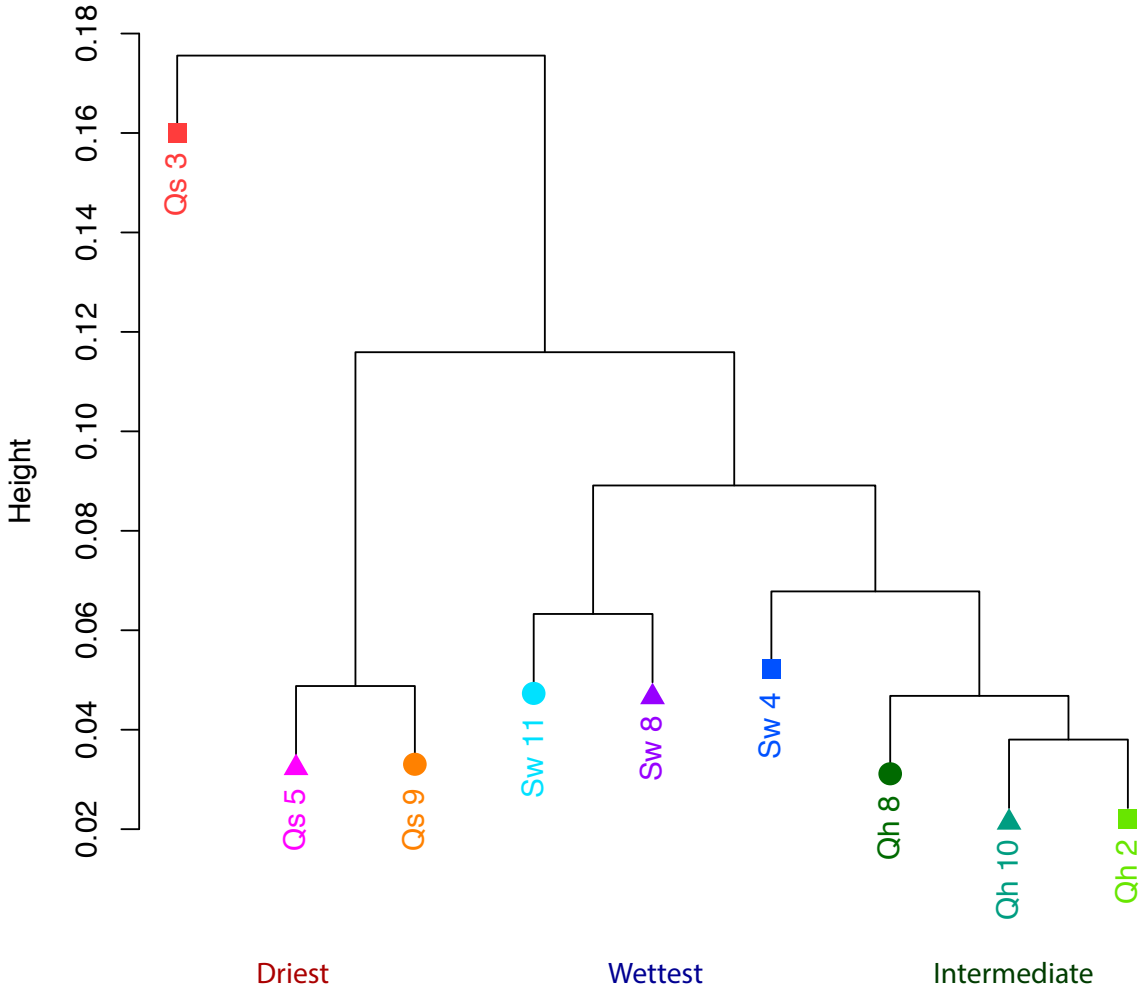

Figure 7. Hierarchical clustering of samples from PhyloChip G3 data.

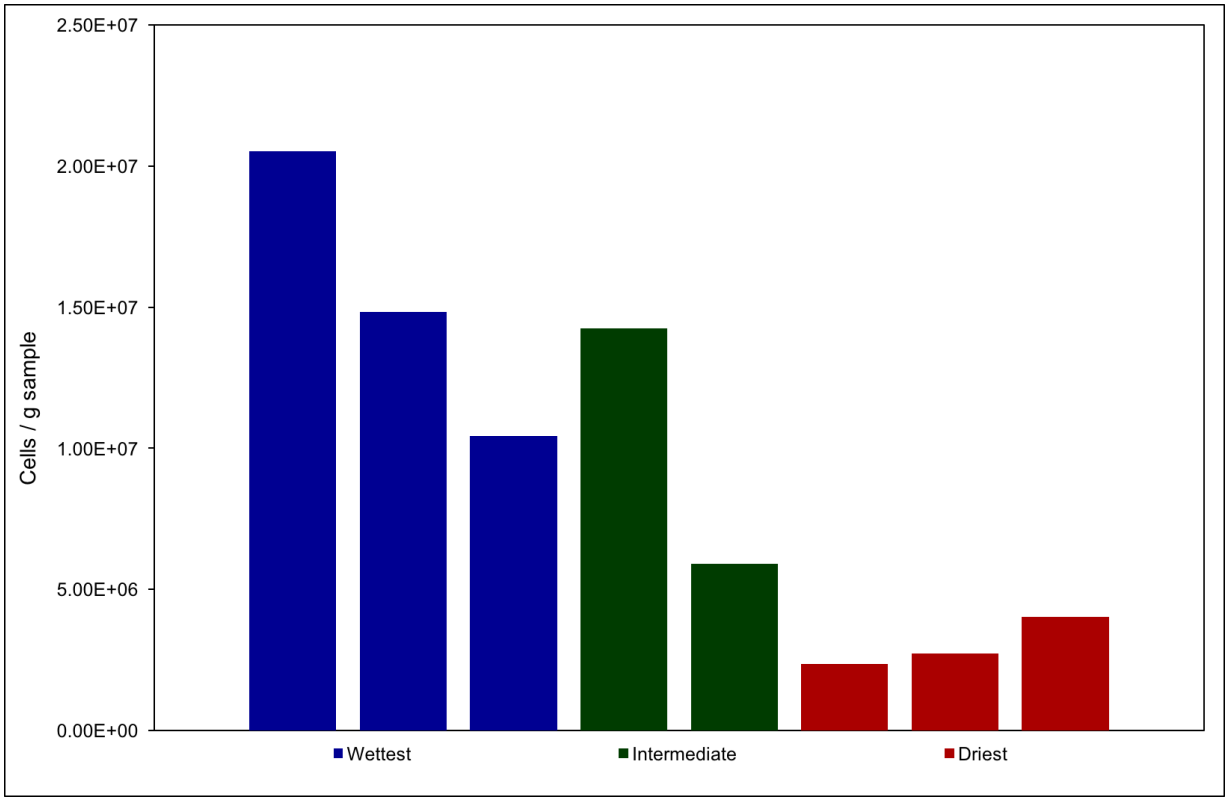

Figure 8. Quantity of auto fluorescent cells at each site. Samples were sectioned into upper, middle, and lower to determine if cell concentration is varied by depth within the sample. Two samples from the intermediate site were used and three samples from each the wettest and driest sites.

Site	Sample	Section	Total cells counted in 100 x 100 um area	Total cell / g sample in section
Wettest	1	Upper	660	1.98E+07
Wettest	1	Middle	1152	3.03E+07
Wettest	1	Lower	384	1.15E+07
Wettest	2	Upper	968	1.75E+07
Wettest	2	Middle	1528	2.00E+07
Wettest	2	Lower	376	6.96E+06
Wettest	3	Upper	620	4.94E+06
Wettest	3	Middle	996	2.04E+07
Wettest	3	Lower	396	5.95E+06
Intermediate	1	Upper	648	8.63E+06
Intermediate	1	Middle	876	1.34E+07
Intermediate	1	Lower	1276	2.07E+07
Intermediate	2	Upper	136	1.71E+06
Intermediate	2	Middle	584	7.47E+06
Intermediate	2	Lower	301	8.51E+06
Driest	1	Upper	72	1.80E+06
Driest	1	Middle	132	2.24E+06
Driest	1	Lower	128	3.05E+06
Driest	2	Upper	60	1.85E+06
Driest	2	Middle	132	3.71E+06
Driest	2	Lower	88	2.60E+06
Driest	3	Upper	220	4.50E+06
Driest	3	Middle	132	3.47E+06
Driest	3	Lower	256	4.09E+06

Table 3. Quantity of auto fluorescent cells at each site. Samples were sectioned into upper, middle, and lower to determine if cell concentration is varied by depth within the sample. Two samples from the intermediate site were used and three samples from each the wettest and driest sites.

Facility #	GPS	Site	$\delta^{13}C$ (‰)	$\Delta^{14}C$	±	^{14}C age cal yr BP	±
CAMS 166850	21°11'59.43"S 69°40'38.42"W	Intermediate	-25.44	9.3	3.0	modern	-
CAMS 166851	21°11'59.77"S 69°40'37.19"W	Intermediate	-24.77	8.8	3.3	modern	-
CAMS 166852	21°12'1.02"S 69°40'36.52"W	Intermediate	-24.89	7.4	3.0	modern	-
CAMS 166846	21°20'46.41"S 69°34'36.68"W	Driest	-29.41	-281.0	2.5	2546	54
CAMS 166847	21°20'46.92"S 69°34'36.18"W	Driest	-27.01	-623.5	2.9	8521	117
CAMS 166849	21°20'46.63"S 69°34'35.14"W	Driest	-25.99	-234.2	2.5	1995	68

Table 4. Radiocarbon dates from selected strata of the dunes. Radiocarbon ages were calibrated to calendar yr BP using the CALIBomb online program (http://calib.qub.ac.uk/CALIBomb/) with the dataset and extension curve corresponding to our study region (SH_CAL13; SHZ1-2) (Hogg et al., 2013; Hua et al., 2013).

Discussion

Patterns and drivers of community composition

In total, we identified 386 unique 16S rRNA sequences. A single cyanobacterial population was the only 16S rRNA sequence found in every sample. This is by far the most widely distributed organism we observed. Excluding this cyanobacteria, only 16 of 385 organisms were found in more than a one sample, the rest are specific to a single sample. Of those 16, only 6 were found at more than one of the three sites. The identification of this cyanobacteria in all samples is therefore remarkable in comparison. When compared at the genomic level, these cyanobacterial populations are 99% similar.

Our statistical analyses of community composition and abundance patterns showed that not only are samples from a given site most similar to each other, but also that samples from adjacent sites are more similar than samples from non-adjacent sites. Further, we found that the spatial distance between individual samples correlates with the distances of the microbial communities. Among the measured abiotic factors, our BioEnv analysis showed that moisture and longitude (proximity to the coast) have the highest correlation with the observed microbial community structure. This finding is not surprising as this is an extremely arid system. Species richness, species evenness, and photosynthetic capacity are all correlated positively to moisture content. In a related study, Robinson et al. (2014) also found that the abundance of algae at sites in the Atacama Desert was correlated to fog occurrence.

At the wettest and intermediate sites examined here, we detected the presence of an amoeba (*Naegleria*) and a novel Thermoplasmatales, both of which have not previously been identified in this system. These organisms were found in the highest abundance and highest percentage of samples at the wettest site, and neither were detected at the driest site. This possibly suggests our fog gradient crosses some threshold water activity value required for their survival. Additionally, the greatest abundance and diversification of Candidate Phyla Radiation Parcubacteria OD1 superphylum and Nanohaloarchaea were identified at the wettest site, while the driest site showed the least abundance and diversification of these organisms. Interestingly, the driest site showed the greatest abundance and diversification of Candidate Phyla Radiation Saccharibacteria TM7.

The cyanobacteria and algae are inferred to be the primary producers for these communities. Our auto-fluorescent cell count showed that the quantity of primary producers declines along the fog gradient, indicating that the wettest site is able to support the highest activity at any given time (Fig. 8; Table 3). Radiocarbon dating of organic matter in samples from the intermediate and driest sites confirmed that rates of carbon turnover are higher at the intermediate site than at the driest site (no data was collected at the wettest site) (Table 4). There is an apparent distinction in the biodiversity and activity of the communities across the gradient, and we conclude that fog delivered moisture is driving these differences.

Conclusions

Although once thought to be almost devoid of biology, recent studies have identified salt deposits as oases for life in the hyperarid Atacama Desert. These communities rely on coastal fog intrusions as a water source since precipitation amounts to less than 2 mm each year. Using metagenomics and 16S rRNA analysis, we explored how the availability of moisture, controlled by distance to the Pacific coast and fog source, shape community composition and structure. All communities were found to be comprised of a large variety of halophilic archaea and *Salinibacter* species and few cyanobacterial populations. Additionally, members of the Candidate Phyla Radiation (Parcubacteria OD1 superphylum and Saccharibacteria TM7), not previously reported from hypersaline environments, were at relatively low abundance in all communities. The majority of all 124 genomically-defined organisms are present at all sites. However, based on bacterial and archaeal abundance patterns, samples cluster by site and biodiversity levels decrease with increasing distance from the ocean. Radiocarbon analysis of organic carbon occluded within halite samples and a count of auto-fluorescent cells further suggest that microbial activity and carbon turnover are highest at the wettest site. We conclude that moisture level, controlled by coastal proximity, is the strongest driver of community membership.

References

Brodie, E.L., T.Z. Desantis, D.C. Joyner, S.M. Baek, J.T. Larsen, G.L. Andersen, T.C. Hazen, P.M. Richardson, D.J. Herman, T.K. Tokunaga, J.M. Wan, and M.K. Firestone. 2006. Application of a High-Density Oligonucleotide Microarray Approach To Study Bacterial Population Dynamics during Uranium Reduction and Reoxidation. Applied and Environmental Microbiology 72(9): 6288–6298.

Brodie, E.L., T.Z. Desantis, J.P. Moberg, I.X. Zubieta, Y.M. Piceno, and G.L. Andersen. 2007. Urban aerosols harbor diverse and dynamic bacterial populations. PNAS 104: 299–304.

Cereceda, P., H. Larrain, P. Osses, M. Farias, and I. Egaña. 2008. The spatial and temporal variability of fog and its relation to fog oases in the Atacama Desert, Chile. Atmospheric Research 87(3-4): 312–323.

Crits-Christoph, A., D.R. Gelsinger, B. Ma, J. Wierzchos, J. Ravel, A.F. Davila, M.C. Casero, and J. Diruggiero. 2016. Functional interactions of archaea, bacteria, and viruses in a hypersaline endolithic community. Environmental Microbiology: n/a–n/a.

de los Ríos, S., S. Valea, C. Ascaso, A.F. Davila, J. Kastovsky, C.P. McKay, B. Gómez-Silva, and J. Wierzchos. 2010. Comparative Analysis of the Microbial Communities Inhabiting Halite Evaporites of the Atacama Desert. International Microbiology 13: 79–89Available at http://www.im.microbios.org.

Desantis, T.Z., E.L. Brodie, J.P. Moberg, I.X. Zubieta, Y.M. Piceno, and G.L. Andersen. 2007. High-Density Universal 16S rRNA Microarray Analysis Reveals Broader Diversity than Typical Clone Library When Sampling the Environment. Microbial Ecology 53(3): 371–383.

Hazen, T.C., E.A. Dubinsky, T.Z. Desantis, G.L. Andersen, Y.M. Piceno, N. Singh, J.K. Jansson, A. Probst, S.E. Borglin, J.L. Fortney, W.T. Stringfellow, M. Bill, M.E. Conrad, L.M. Tom, K.L. Chavarria, T.R. Alusi, R. Lamendella, D.C. Joyner, C. Spier, J. Baelum, M. Auer, M.L. Zemla, R. Chakraborty, E.L. Sonnenthal, P. D'haeseleer, H.Y.N. Holman, S. Osman, Z. Lu, J.D. Van Nostrand, Y. Deng, J. Zhou, and O.U. Mason. 2010. Deep-Sea Oil Plume Enriches Indigenous Oil-Degrading Bacteria. Science 330(6001): 204–208.

Hogg, A., Q. Hua, P. Blackwell, M. Niu, C. Buck, T. Guilderson, T. Heaton, J. Palmer, P. Reimer, R. Reimer, C. Turney, and S. Zimmerman. 2013. SHCAL13 southern hemisphere calibration, 0–50,000 years cal bp. Radiocarbon 55: 1889–1903.

Hua, Q., M. Barbetti, and A. Rakowski. 2013. Atmospheric radiocarbon for the period 1950–2010. Radiocarbon 55: 2059–2072.

Hyatt, D., G.L. Chen, P. LoCascio, M. Land, F. Larimer, and L. Hauser. 2010. Prodigal: prokaryotic gene recognition and translation initiation site identification. BMC Bioinformatics 11(119).

McKay, C., E.I. Friedmann, B. Gómez-Silva, L. Caceres-Villanueva, D. Andersen, and R. Landheim. 2003. Temperature and Moisture Conditions for Life in the Extreme Arid Region of the Atacama Desert: FourYears of Observations Including the El Niño of 1997–1998. Astrobiology 3.

Navarro-Gonzalez, R. 2003. Mars-Like Soils in the Atacama Desert, Chile, and the Dry Limit of Microbial Life. Science 302(5647): 1018–1021.

Peng, Y., H.C.M. Leung, S.M. Yiu, and F.Y.L. Chin. 2012. IDBA-UD: a de novo assembler for single-cell and metagenomic sequencing data with highly uneven depth. Bioinformatics 28(11): 1420–1428.

Probst, A.J., C.J. Castelle, A. Singh, C.T. Brown, K. Anantharaman, I. Sharon, L.A. Hug, D. Burstein, J.B. Emerson, B.C. Thomas, and J.F. Banfield. 2016. Genomic resolution of a cold subsurface aquifer community provides metabolic insights for novel microbes adapted to high CO 2concentrations. Environmental Microbiology.

Robinson, C.K., J. Wierzchos, C. Black, A. Crits-Christoph, B. Ma, J. Ravel, C. Ascaso, O. Artieda, S. Valea, M. Roldán, B. Gómez-Silva, and J. Diruggiero. 2014. Microbial diversity and the presence of algae in halite endolithic communities are correlated to atmospheric moisture in the hyper-arid zone of the Atacama Desert (CK Robinson, J Wierzchos, C Black, A Crits-Christoph, B Ma, J Ravel, C Ascaso, O Artieda, S Valea, M Roldán, B Gómez-Silva, and J Diruggiero, Eds.). Environmental Microbiology 17(2): n/a–n/a.

Rothschild, L.J., and R.L. Mancinelli. 2001. Life in extreme environments. Nature 409: 1–10.

Sharon, I., M.J. Morowitz, B.C. Thomas, E.K. Costello, D.A. Relman, and J.F. Banfield. 2013. Time series community genomics analysis reveals rapid shifts in bacterial species, strains, and phage during infant gut colonization. Genome Research 23(1): 111–120.

Stivaletta, N., R. Barbieri, and D. Billi. 2012. Microbial Colonization of the Salt Deposits in the Driest Place of the Atacama Desert (Chile). Origins of Life and Evolution of Biospheres 42(2-3): 187–200.

Stuiver, M., and H. Polach. 1977. Reporting of 14C data. Radiocarbon 19: 355–363.

Vogel, J.S., J.R. Southon, D.E. Nelson, and T.A. Brown. 1984. Performance of catalytically condensed carbon for use in accelerator mass spectrometry. Nuclear Instuments and Methods in Physics Research: 289–293.

Warren-Rhodes, K.A., K.L. Rhodes, S.B. Pointing, S.A. Ewing, D.C. Lacap, B. Gómez-Silva, R. Amundson, E.I. Friedmann, and C.P. McKay. 2006. Hypolithic Cyanobacteria, Dry Limit of Photosynthesis, and Microbial Ecology in the Hyperarid Atacama Desert. Microbial Ecology 52(3): 389–398.

Weinmaier, T., A.J. Probst, M.T. Duc, D. Ciobanu, J.-F. Cheng, N. Ivanova, T. Rattei, and P. Vaishampayan. 2015. A viability-linked metagenomic analysis of cleanroom environments: eukarya, prokaryotes, and viruses. Microbiome: 1–14.

Wierzchos, J., C. Ascaso, and C.P. McKay. 2006. Endolithic Cyanobacteria in Halite Rocks from

the Hyperarid Core of the Atacama Desert. Astrobiology 6(4): 1–7.
Wierzchos, J., A. de los Rios, and C. Ascaso. 2012. Microorganisms in desert rocks: the edge of life on Earth. International Microbiology 15: 171–181.
Wrighton, K.C., B.C. Thomas, I. Sharon, C.S. Miller, C.J. Castelle, N.C. VerBerkmoes, M.J. Wilkins, R.L. Hettich, M.S. Lipton, K.H. Williams, P.E. Long, and J.F. Banfield. 2012. Fermentation, Hydrogen, and Sulfur Metabolism in Multiple Uncultivated Bacterial Phyla. Science 337(6102): 1661–1665.

Chapter 4:
Late Quaternary paleoenvironmental record in loess deposits of the northern Atacama Desert, Chile

Introduction

The hyperarid Atacama Desert is the driest place on earth and has likely maintained a semi-continuous hyperarid climate for millions of years (Hartley and Chong, 2002; Amundson et al., 2012; Jordan et al., 2014). However, recent research on middens, wetlands, and stream activity indicates significant late Quaternary climate oscillations from 17,500 to 14,200 and 13,800 to 9,700 yr BP, known as Central Andean Pluvial Events (CAPE) (Rech et al., 2002; Nester et al., 2007; Quade et al., 2008; Gayo et al., 2012). These pluvial periods greatly increased Andean runoff and subsequently impacted the suitability of the desert for human habitation. The development of further high-resolution paleoclimate records is highly desirable, particularly in the watershed of the Salar Llamara. Within this region, contributing tributaries are now known to have experienced pluvial episodes corresponding to significant late Pleistocene hunter and gatherer occupations and dense late Holocene (but pre-Columbian) agricultural settlements (Workman, 2012; Latorre et al., 2013). This region is thus one of great climatic and anthropological interest.

One of the unique local climate characteristics of this area is the strong and persistent on-shore wind which has created various sculpted landscapes in the basin and its periphery. Within what is largely a deflationary landscape, we found small pockets of loess that have accumulated in depressions of highly eroded Miocene anhydrite and halite. In this study, we investigated these previously unrecognized loess deposits to determine whether they accumulate continuously or episodically, and if they might contain chemical and isotopic records of climate change. In addition, we consider the mechanisms that contribute to the formation and preservation of these loess deposits within this highly erosive setting.

Methods

Site description and sample collection

This study was conducted at two sites within the Llamara basin, a local semi-enclosed basin which has, over geological time, contained lakes, wetlands, and/or salt accumulations from the evaporation of waters derived from the Andes to the east (Fig. 1). The various basin sedimentary outcrops range in age from Miocene to early Holocene. The deposits examined here immediately overlie a Miocene outcrop known as the Soledad formation. The Soledad formation is characterized by a several meter-thick anhydrite-rich cap that overlies many meters of nearly pure halite (Pueyo et al., 2001). Locally, the anhydrite cap is discontinuous (likely due to eolian and water erosion), leading a badland-like topography with closed depressions several meters deep and tens of meters in diameter. In our field area, many of these depression have been partially infilled with a meter or more of loess. In most locations, the loess deposits are capped by a thin crust of distinctive lichen-bearing crust (Fig. 2).

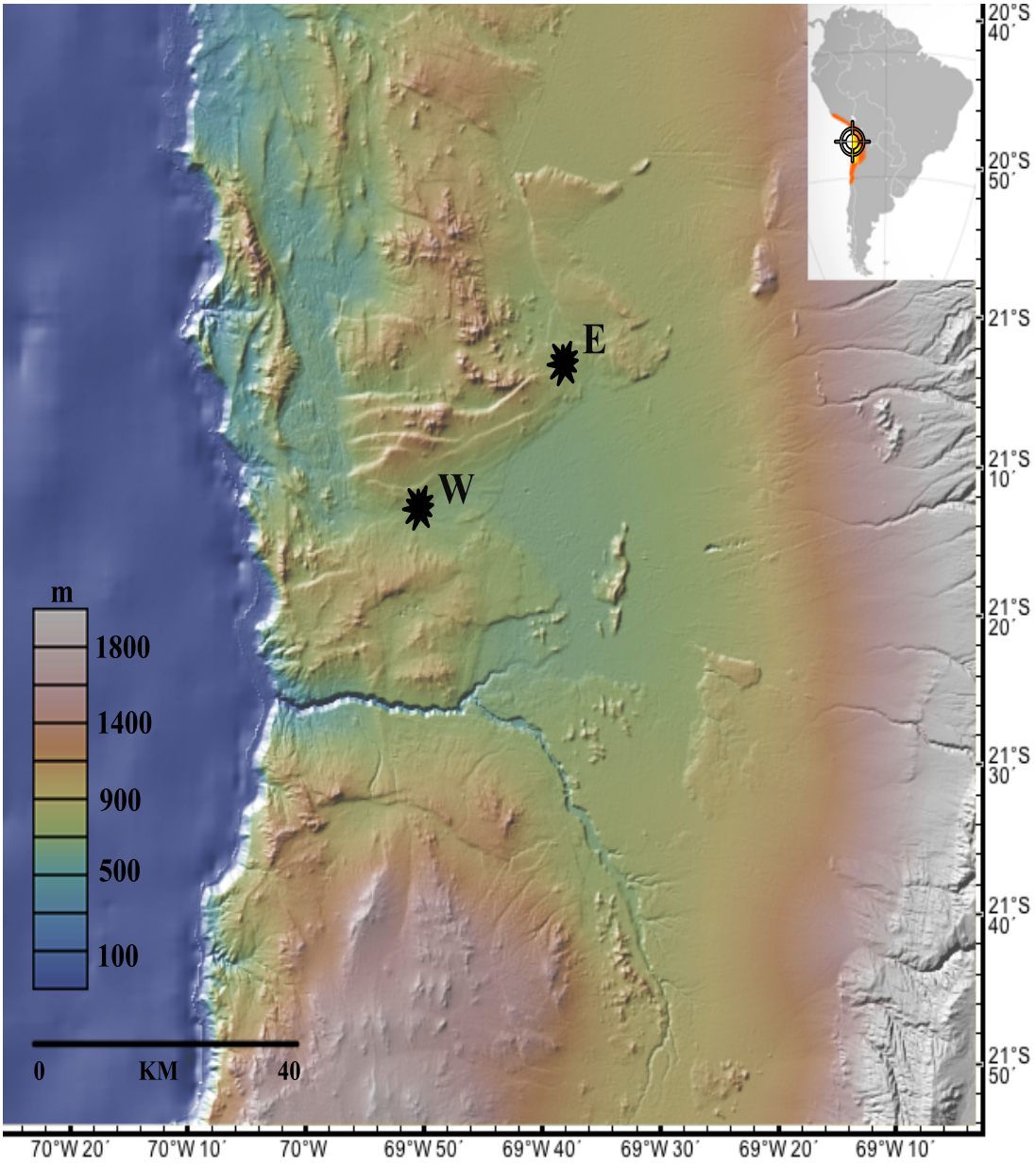

Figure 1. Location of sites within the Salar Llamara basin.

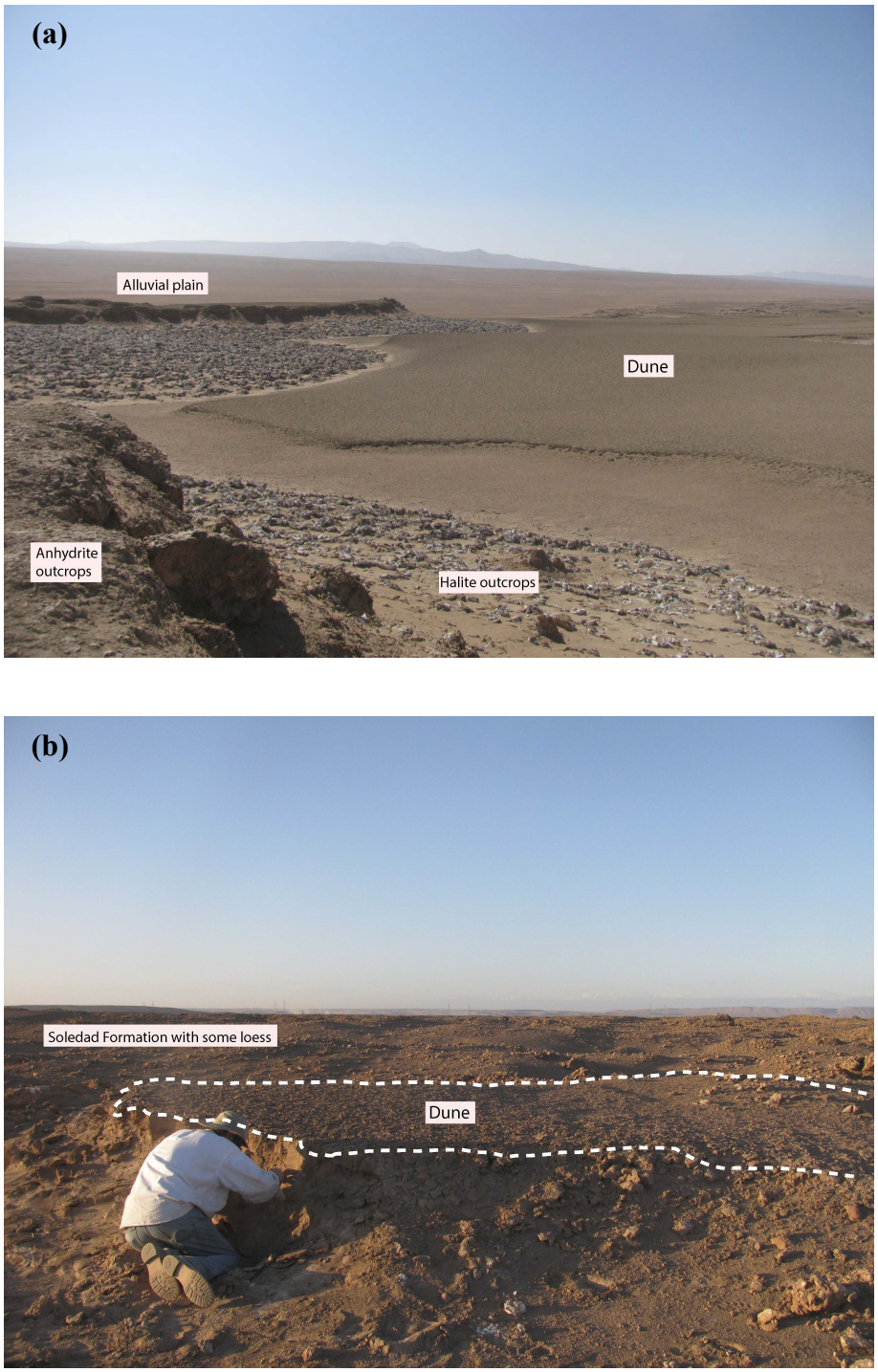

Figure 2. Landscape of the Soledad formation demonstrating the rugged terrain and eroded basins now containing loess deposits at the west site (a) and east site (b).

The two sites are located along a west and east transect on the northern edge of the Soledad formation at 835 and 895 meters above sea level (m.a.s.l.), and approximately 25 km and 50 km from the Pacific coast. Both sites experience frequent and strong onshore winds which often bring marine fog. The strong winds in other nearby landforms clearly result in significant deflation of the landscape, such as inverted stream channels. In other areas (particularly around perennial shrubs and trees), sediment is deposited as coppice dunes.

In June 2013, one loess dune at each site was hand excavated, and the stratigraphic and pedogenic soil features were logged and described using standard soil mapping procedures (Soil Survey Staff, 1999). Samples of each visually observable horizon were collected and transported back to the lab in Ziploc bags.

Environmental monitoring

We installed micrometeorological instrumentation to monitor key environmental parameters. Decagon Devices Inc. leaf wetness sensors, Davis cup anemometers, and total solar radiation sensors were used to monitor meteorological conditions at both sites. The leaf wetness sensors were installed as a proxy measurement for fog and dew accumulation (Burgess and Dawson, 2004). Since it did not rain during the year of study, we have assumed that any "wetness" events recorded by the leaf wetness sensor result from dew or fog. A value of 460 counts was chosen as the threshold to report wetness, which according to the manufacturer is a conservative value. In addition, Onset HOBO® Pro v2 (U23-002) temperature and relative humidity sensors were carefully installed beneath sections of lichen crust at each site (Fig. 3). Two sensors were installed at the east site and four sensors were installed at the west site. For all of the sensors, hourly monitoring began June 2013 and ran continuously for 13 months.

Soil chemical and physical characterization

Particle size analysis was performed on each sediment horizon using the hydrometer method outlined by Gee and Bauder (1986). Briefly, excess salt was removed prior to analysis by washing samples with deionized water. 30 g of dried sample was dispersed in 100 mL of 5% sodium hexametaphosphate solution by shaking for 16 hours on a horizontal shaker. The suspension was transferred to a sedimentation cylinder and deionized water added to reach 1 L. Contents of the cylinder were mixed thoroughly before the first reading. Readings of each sample and the blank solution were taken at 0.5, 1, 3, 10, 30, 60, 90, 120, and 1440 minutes using the hydrometer. Temperature readings were also taken at each time point.

X-ray diffraction (XRD) analysis was made on a PANalytical X'Pert Pro diffractometer equipped with a cobalt x-ray tube and X'Celerator detector in the department of Earth and Planetary Science at UC Berkeley. Dried samples were prepared for analysis by loading into glass well plates. The material was pressed flat using a glass slide. Each sample was run for 25 minutes.

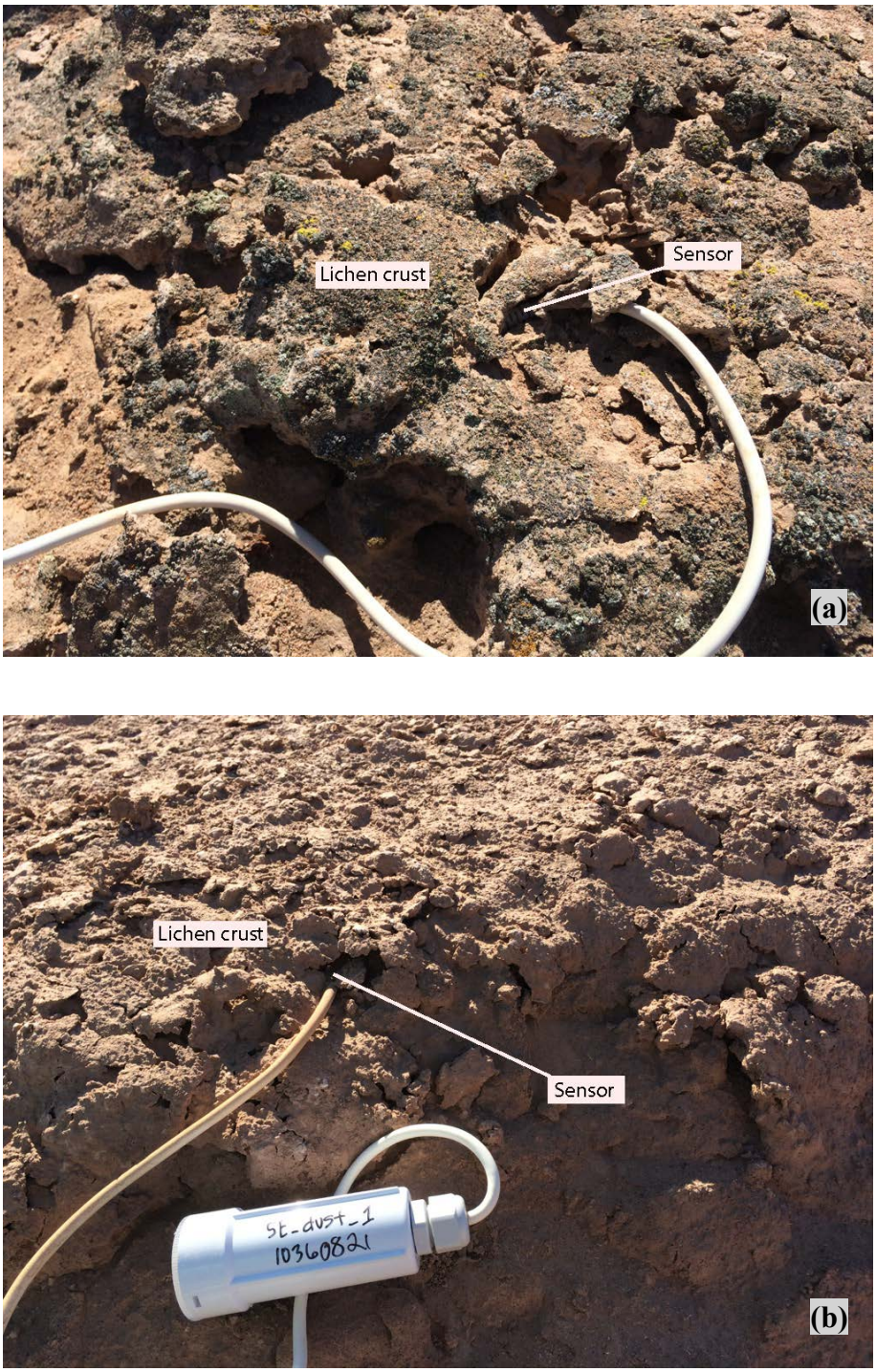

Figure 3. Installation of temperature and relative humidity sensors beneath the crust at the west site (a) and east site (b).

Sulfate stable isotope ratios
Sulfate sulfur stable isotope ratio analysis was performed in the Laboratory for Environmental and Sedimentary Isotope Geochemistry at the Department of Earth and Planetary Science, UC Berkeley. Soil sulfate was dissolved in water by shaking pulverized soil for 4 hours in excess deionized water. Sediment was then removed by filtering through a 0.2 μm paper filter. Sulfate was precipitated as $BaSO_4$ by adding excess 1 M $BaCl_2$ to the solution, then drying at 65 °C (following the protocol outlined in Michalski et al. (2004)). Approximately 50-200 μg of $BaSO_4$ sample was analyzed in duplicate on a GV Isoprime isotope ratio mass spectrometer and a Eurovector Elemental Analyzer (EuroEA3028-HT). The analytical precision of the measurement is better than 0.2‰. Values are reported as $\delta^{34}S$ relative to CDT.

Radiocarbon measurements
Samples were prepared for radiocarbon analysis by first removing inorganic carbon and excess salts. 5 g of pulverized soil was soaked in 0.5 M HCl for 24 hours with intermittent shaking to agitate the solution, followed by centrifuging and decanting the acidic solution. To ensure complete removal of HCl, the samples underwent alternating soaking and shaking in deionized water for 24 hours, then they were centrifuged and the supernatant discarded. This washing process with deionized water was repeated twice before samples were dried at 60 °C.

Radiocarbon analysis was performed on the Van de Graaff FN accelerator mass spectrometer (AMS) at the Center for Accelerator Mass Spectrometry at Lawrence Livermore National Laboratory, Livermore CA. Approximately 0.5 g of washed sample was prepared for ^{14}C measurement by sealed-tube combustion to CO_2 in the presence of CuO and Ag, and then reduced into iron powder in the presence of H_2 at 570 °C (Vogel et al., 1984). Aliquots of the CO_2 were analyzed for $\delta^{13}C$ at the Department of Geological Sciences Stable Isotope Laboratory, University of California Davis (GVI Optima Stable Isotope Ratio Mass Spectrometer). $\delta^{13}C$ values are reported relative to V-PDB. Measured $\delta^{13}C$ values were used to correct for mass-dependent fractionation and ^{14}C isotopic values are reported in $\Delta^{14}C$ notation. $\Delta^{14}C$ values were corrected for ^{14}C decay since 1950 (Stuiver and Polach, 1977), and the AMS precision was 3‰. Radiocarbon ages were calibrated to calendar year BP using the CALIBomb online program (http://calib.qub.ac.uk/CALIBomb/) with the dataset and extension curve corresponding to our study region (SH_CAL13; SHZ1-2) (Hogg et al., 2013; Hua et al., 2013).

Organic nitrogen stable isotope ratios
Samples for organic nitrogen stable isotope ratio analysis were prepared in a similar fashion as described above for radiocarbon analysis to remove inorganic forms. Dried material was weighed in tin capsules and analyzed in duplicate by continuous flow (CF) dual isotope analysis using a CHNOS Elemental Analyzer interfaced to an IsoPrime100 mass spectrometer at the UC Berkeley Center for Stable Isotope Biogeochemistry. Long-term external precision for nitrogen isotope analyses is ± 0.15‰. $\delta^{15}N$ values are reported relative to Air N_2.

Total fatty acid extraction and GC-IRMS analysis
Total fatty acids were extracted from the soils following the method developed by Graber and Tsechansky (2010) with a few modifications. Excess salts were first removed from the east site by shaking samples in 250 mL Ultrapure water for 4 hours then centrifuging and the discarding the supernatant. This procedure to remove excess salt was not performed on the west site

samples. 4 g of dried, sieved, and pulverized soil samples were placed in a Teflon tube with $NaSO_4$ added as a desiccant. 6 mL of 5% methanolic HCL and 6 mL of toluene were added, the samples vortexed, and then placed in the oven at 60 ˚C overnight. The following day, 15 mL of 5% NaCl solution was added, the samples vortexed, and then centrifuged for 40 min at 3000 rpm. The upper organic-bearing phase was pipetted into a new tube and 15 mL of a 2% $KHCO_3$ solution was added, sampled gently shaken for 2 min, and then centrifuged for 30 min at 3000 rpm. The upper organic-bearing phase was extracted by pipetting and passed over a $NaSO_4$ column then a Si gel column. Samples were dried in a stream of N_2 gas and then stored in the freezer at until analysis. Prior to analysis, samples from the west site were mixed with 100 ul 1:1 n-hexane:MTBE solution and samples from the east site mixed with 50 ul 1:1 n-hexane:MTBE solution. Five unknown samples were processed as described above in a batch along with one procedural blank (pure SiO_2).

Samples were analyzed in the Astrobiogeochemistry lab at NASA Jet Propulsion Laboratory in Pasadena, CA on a GC-IRMS using a DB-23 column (122-2362). Samples were run as 1 µl injections in duplicate along with the Supelco 37 Component FAME Mix (CRM47885) and the procedural blanks from the extraction (pure SiO_2). Fatty acids were identified using Thermo Scientific™ Xcalibur™ software program and were quantified using a one-point calibration referenced to the Supelco 37 Component FAME Mix. Samples were run a second time (also in duplicate) to measure the δ^2H of stearic and palmitic acids. Duplicate analyses of Fatty Acid Ester Mixture F8-3 were run along with the unknown samples (CRM available from https://arndt.schimmelmann.us/fatty-acid-esters.html).

Results and Discussion

Location and source of loess deposits

It is increasingly recognized that arid landscapes are complex mosaics of areas impacted by both eolian deflation and deposition. For example, in the southwestern USA deflation of exposed playas and stream beds generates dust that accumulates on surrounding landscapes as an eolian mantle (V horizon) over underlying soils (Turk and Graham, 2011). The Salar Llamara region in Chile represents a similar, but more extreme, version of processes that appear to operate in many deserts.

On the surface, the Soledad formation is a rough and discontinuous unit of anhydrite that is up to several m thick in some places, and is surrounded in many areas by relatively smooth basins of nearly pure halite. Within these basins are deposits of dust and eolian material. From the perspective of satellite imagery, a distinctive pattern of the deposits emerges (Fig. 4). On the western edge of the Soledad formation, the deposits are well developed transverse dunes, oriented slightly to the NW. Further to the east, the clarity of the shape of the dunes decreases. There they maintain a less distinct NW orientation, and in many areas the dunes may more commonly mimic a star-like orientation. Transverse dunes are oriented perpendicular to the direction of wind flow, while star dunes are believed to form in variable wind trajectories (Anderson and Anderson, 2010). We excavated two dunes along this gradient, one dune on the western edge, and one further to the east (Fig. 1).

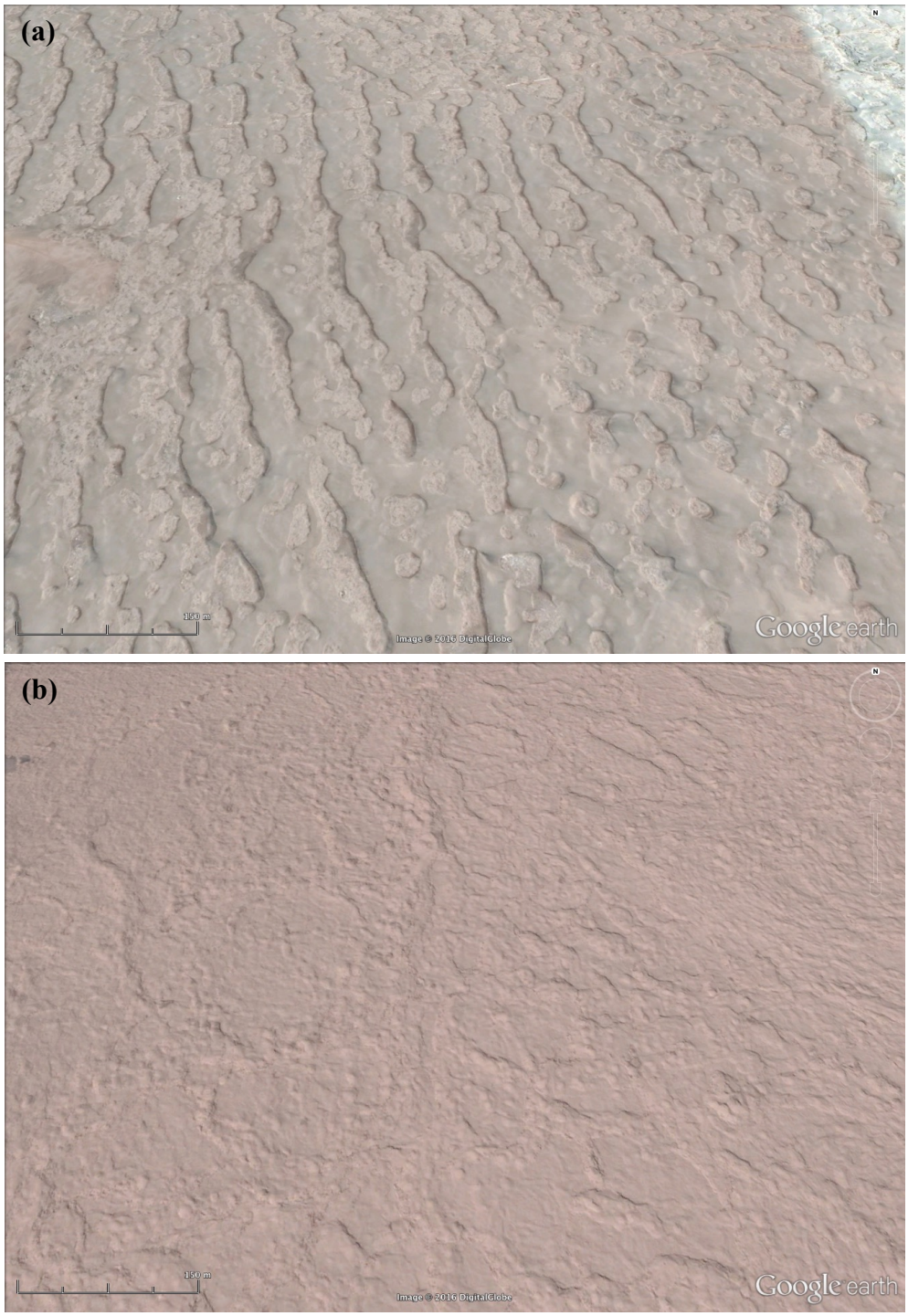

Figure 4. Satellite image of sites showing the shape of the dunes. Images taken from GoogleEarth in June 2016.
(a) On the western edge of the Soledad formation, the deposits are well developed transverse dunes, oriented slightly to the NW.
(b) Further to the east, the clarity of the shape of the dunes decreases and the dunes take on a more star-like orientation.

A unique characteristics of the alluvial fan landscapes that abut the Soledad formation is that their thick, sulfate rich soils have been irregularly deflated by wind, creating a novel landscape of low "mesas" of sulfate and dust-rich soils that are separated by shallow deflationary basins where the sulfate and dust has been removed to the level of an indurated halite layer (Fig. 5). The removal of susceptible soil particles from these fan surfaces is aided by their relatively low surface roughness. Smooth surfaces facilitate entrained dust particles to remain suspended during transport (Tsoar and Pye, 1987). However, the rugged topography of the Soledad formation represents a sharp relative increase in surface roughness. The large increase in surface roughness in turn leads to a reduction in velocity and a rapid deposition of particles near the roughness boundary. Clearly, the deposition is not a simple continuous blanket of loess (given the dune-like features), likely due to the complex topography and erratic eddies that occur. However, the overall trend appears to be one of a sharp and clear transition between dust sources on alluvial fans, and dust sinks within the Soledad formation.

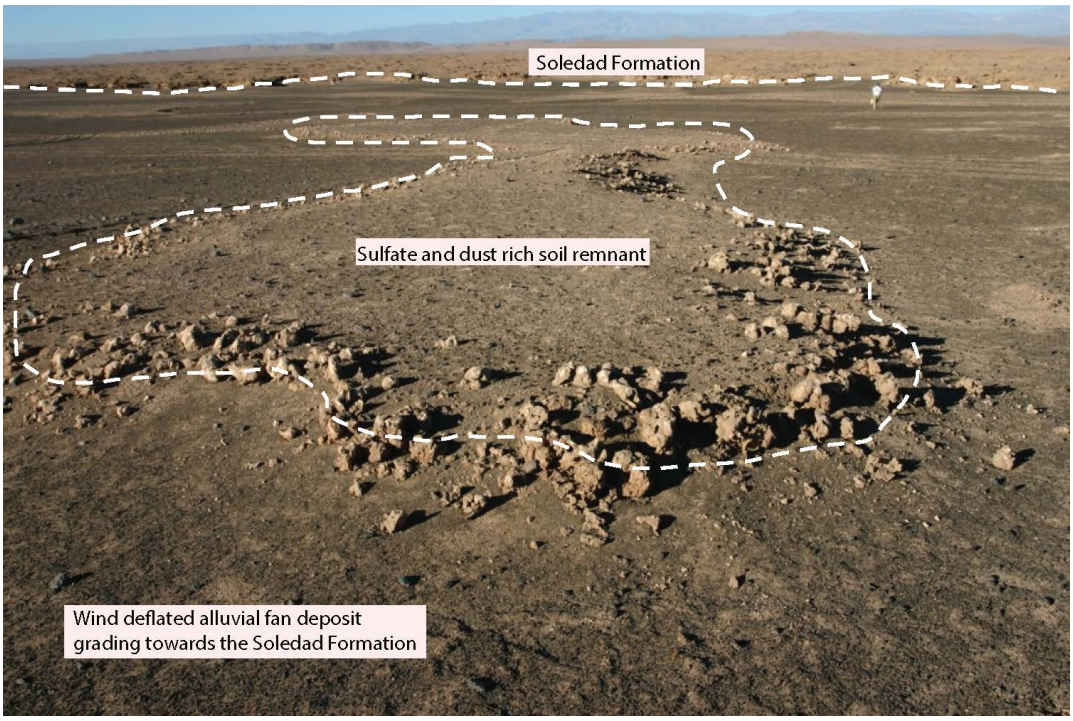

Figure 5. Wind deflated alluvial fans grading towards the Soledad Formation presumed to be the source of loess.

Dune age and rates of accretion

The surface crust of the dunes is a few cm thick and appears solidified by both lichen and sulfate salts. Beneath this crust, there is little evidence of pedogenesis or physical mixing. To test the notion that the dunes have accreted semi-continuously over time (and have not been physically or biologically mixed), we conducted radiocarbon dating at several depths in both deposits. Remarkably, both profiles show a clear trend of increasing age with increasing depth.

The surface-most layer of the west site has an average age of 1,691 years BP (n=4) and the surface of the east site has an average age of 2,573 years BP (n=3). Both dunes have late Pleistocene maximum ages at their bases, ~18,941 years BP in the west deposit and 17,933 years BP in the east deposit (Table 1; Fig. 6). These dunes therefore represent the slow accumulation of captured material since the late Pleistocene. The increase in age monotonically with depth reflects the absence of biological and physical mixing processes. Due to the hyperarid conditions that have prevailed throughout the formation of these dunes, organic matter has been buried without significant degradation. This leaves a record of sedimentation and biologic material that is preserved.

While the accumulation and growth of the dunes has been continuous, the rate of growth has not been constant over time. During the early stages of accumulation, both dunes were growing at a rate of 0.07 cm yr^{-1}. This rate has been decreasing over time and both sites are now growing at rates less than 0.01 cm yr^{-1} (Fig. 7). Given that the timing of these changes occurs simultaneously at both sites, we conclude that the decrease in accretion rates is a response to a regional environmental change occurring during the early Holocene.

The rapid decline in dust accumulation rates at roughly 10,000 yr ago coincides with global sea levels approaching modern conditions. From 22,000 to 19,000 yr BP global sea level reached its recent minimum elevation during the height of the last glacial maximum (LGM) (Yokoyama et al., 2000; Lambeck et al., 2002). This resulted in a decline of about 130 m in sea level, and would have moved the coastline about 7 km further offshore. This position of sea level would therefore have increased the elevation of our field sites to 965 and 1025 m.a.s.l. from their present locations at 835 and 895 m.a.s.l.

Presently, fog in the Atacama Desert seldom penetrates regions above 1000 m.a.s.l. (Rech et al., 2003; Houston, 2006). It is therefore probable that fog intensity and frequency at our field areas were significantly lower during the LGM than they are today, given the increased elevations and distance from the coast. As a starting hypothesis, prior to examining the chemical and isotopic records in the sediment, we propose that the changes in loess deposition rates are in response to changes in sea level, which correspond to an increase in wind speeds and fog frequency, and a decrease in the rate of loess deposition. The lower sea level may have facilitated expanses of shelf for wind deflation and the decreased fog intensity may have weakened soil surface crusts and made sulfate-rich soils more susceptible to deflation.

CAMS #	Sample	Depth	$\delta^{13}C_{org.}$	$\Delta^{14}C$	±	Fraction Modern	±	^{14}C age	±	Age	±
		(cm)	(‰)					(yr BP)		(cal yr BP)	
164992	West 1	0-2	-22.8	-210.0	2.5	0.7961	0.0025	1830	25	1723	23
165000	West 1	0-2	-23.1	-208.0	3.0	0.7981	0.0030	1810	35	1638	26
164994	West 1	0-2	-22.7	-190.8	2.8	0.8154	0.0028	1640	30	1499	32
164995	West 1	0-2	-22.6	-226.2	2.3	0.7799	0.0023	1995	25	1904	26
164965	West 3	5-13	-24.5	-522.2	2.3	0.4815	0.0023	5870	40	6637	41
165882	West 5	32-49	-21.0	-691.0	2.3	0.3090	0.0023	9440	60	10629	76
165160	West 7	67-83	-28.3	-853.1	2.0	0.1469	0.0020	15410	110	18642	116
165883	West 9	104-118		-867.1	2.6	0.1329	0.0026	16210	160	19496	220
164993	West 11	121-149	-25.1	-860.2	2.0	0.1409	0.0020	15740	120	18941	130
164996	East 1	0-2	-24.2	-284.5	2.6	0.7211	0.0026	2625	30	2736	21
165363	East 1	0-2	-23.6	-270.3	2.2	0.7297	0.0022	2530	25	2546	53
164997	East 1	0-2	-23.3	-272.0	2.2	0.7336	0.0022	2490	25	2438	60
164998	East 4	7-14	-28.1	-774.7	1.9	0.2270	0.0019	11910	70	13673	76
164999	East 5	14-31	-28.8	-837.0	1.9	0.1642	0.0019	14510	100	17640	140
164966	East 7	33-52	-29.6	-842.4	2.0	0.1589	0.0020	14780	100	17933	137

Table 1. Radiocarbon dates from selected strata of the dunes. Radiocarbon ages were calibrated to calendar yr BP using the CALIBomb online program (http://calib.qub.ac.uk/CALIBomb/) with the dataset and extension curve corresponding to our study region (SH_CAL13; SHZ1-2) (Hogg et al., 2013; Hua et al., 2013).

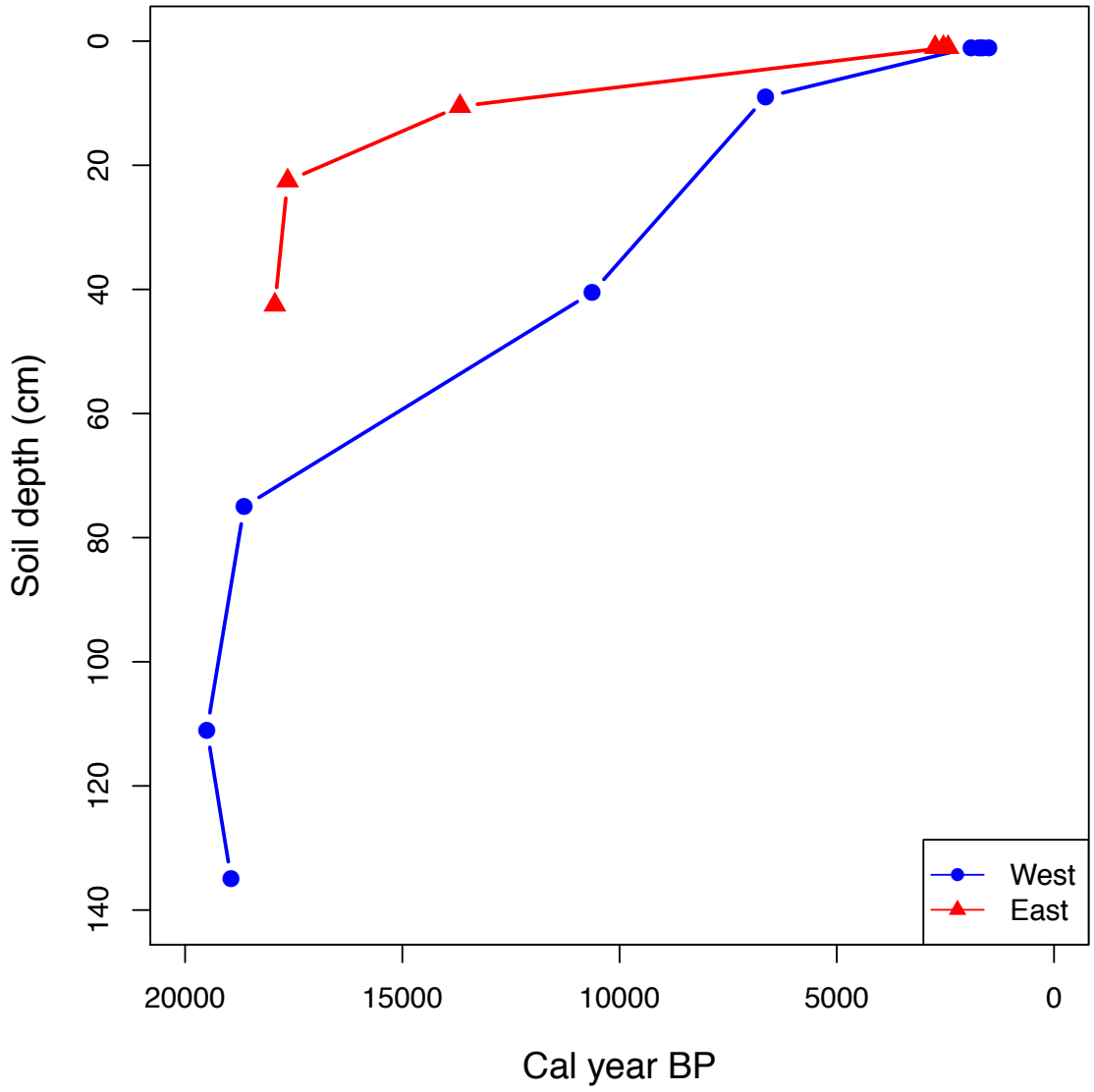

Figure 6. Radiocarbon measurements taken from strata within each dune profile. Additional data can be found in Table 1.

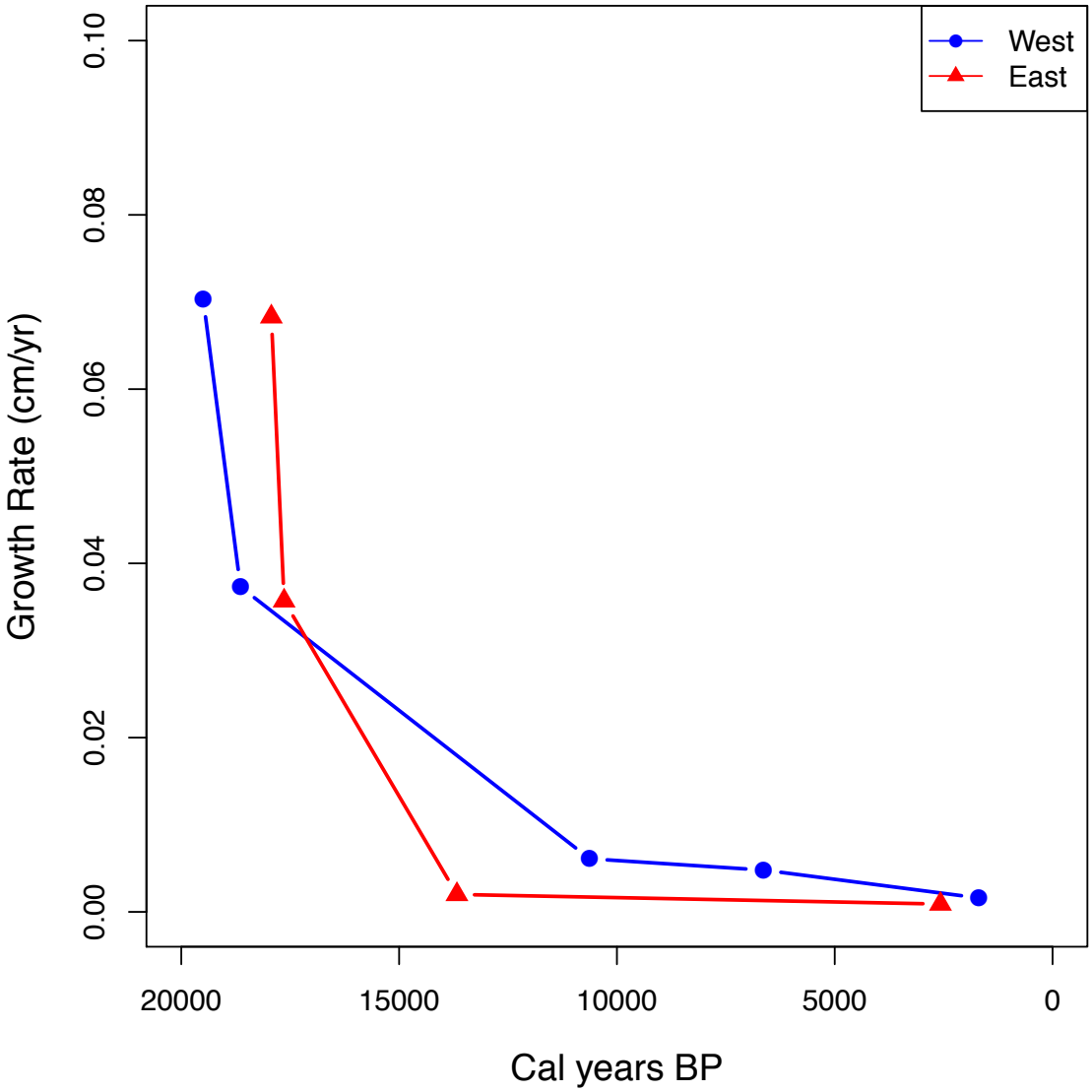

Figure 7. Rate of dune accretion calculated using radiocarbon ages in Figure 6.

Present day meteorological conditions

We used leaf wetness sensors to measure the present day differences in fog and dew between the two sites. Our data clearly show that the west site receives more intense and frequent fog events. Over the 13 months of recording, the west site had liquid moisture present for 3,109 hours, and the east site for 1,181 hours, out of 9,504 total hours. Thus, dew was on the sensor ~32% of the year at the west site, and ~12% at the east site. This difference in fog occurrence is explainable by the sites distance to the coast. The west site is ~25 km closer to the coast than the east site, therefore closer to the source of fog.

Similar to the leaf wetness sensors, monitoring of the temperature (T) and relative humidity (RH) under the surface crust at each site showed that the west site maintains a higher RH than the east site (Table 2). The average annual RH at the west site was 1.5x greater than the east site, 52% versus 34%. This difference in average RH is consistent throughout all seasons and likely a response to fog conditions. The average temperature beneath the crust at the west site was 18 °C, and at the east 20 °C. The sensors show that the east site has greater temperature extremes, reaching 10 °C warmer and 2.5 °C cooler than the west site. These temperature differences are likely a product of the more frequent and intense fog at the west site, which keeps the soil cooler and wetter.

Our anemometers showed that the winds commonly blow SW or NE at our field sites, and that the west site regularly experiences higher speeds. On average, the wind speed at the west site was 3 m s^{-1} and 1.7 m s^{-1} at the east site (Fig. 8 and 9). Both sites experience gusts as high as 11.5 m s^{-1}.

Sensor	Jun - Aug Avg T (°C)	Sep - Nov Avg T (°C)	Dec - Feb Avg T (°C)	Mar - May Avg T (°C)	Jun - Aug Avg RH (%)	Sep - Nov Avg RH (%)	Dec - Feb Avg RH (%)	Mar - May Avg RH (%)
W1	13.6	18.1	22.1	18.2	56.4	46.5	47.7	55.9
W2	14.4	17.6	20.9	18.1	58.7	53.9	56.1	61.3
W3	15.3	19.8	23.5	19.8	49.1	42.2	45.1	50.4
W4	13.1	18.7	23.1	17.9	56	44.4	45.9	55.7
West avg	**14.1**	**18.6**	**22.4**	**18.5**	**55.1**	**46.8**	**48.7**	**55.8**
E1	13.8	22.1	27.3	19.9	37.5	24.4	29.7	38.9
E2	15.6	21.2	25.3	20.5	35.5	28.7	36.1	40.4
East avg	**14.7**	**21.7**	**26.3**	**20.2**	**36.4**	**26.5**	**32.9**	**39.6**

Table 2. Temperature and relative humidity data recorded using Onset HOBO® Pro v2 (U23-002) sensors installed beneath the surface crust (Figure 3).

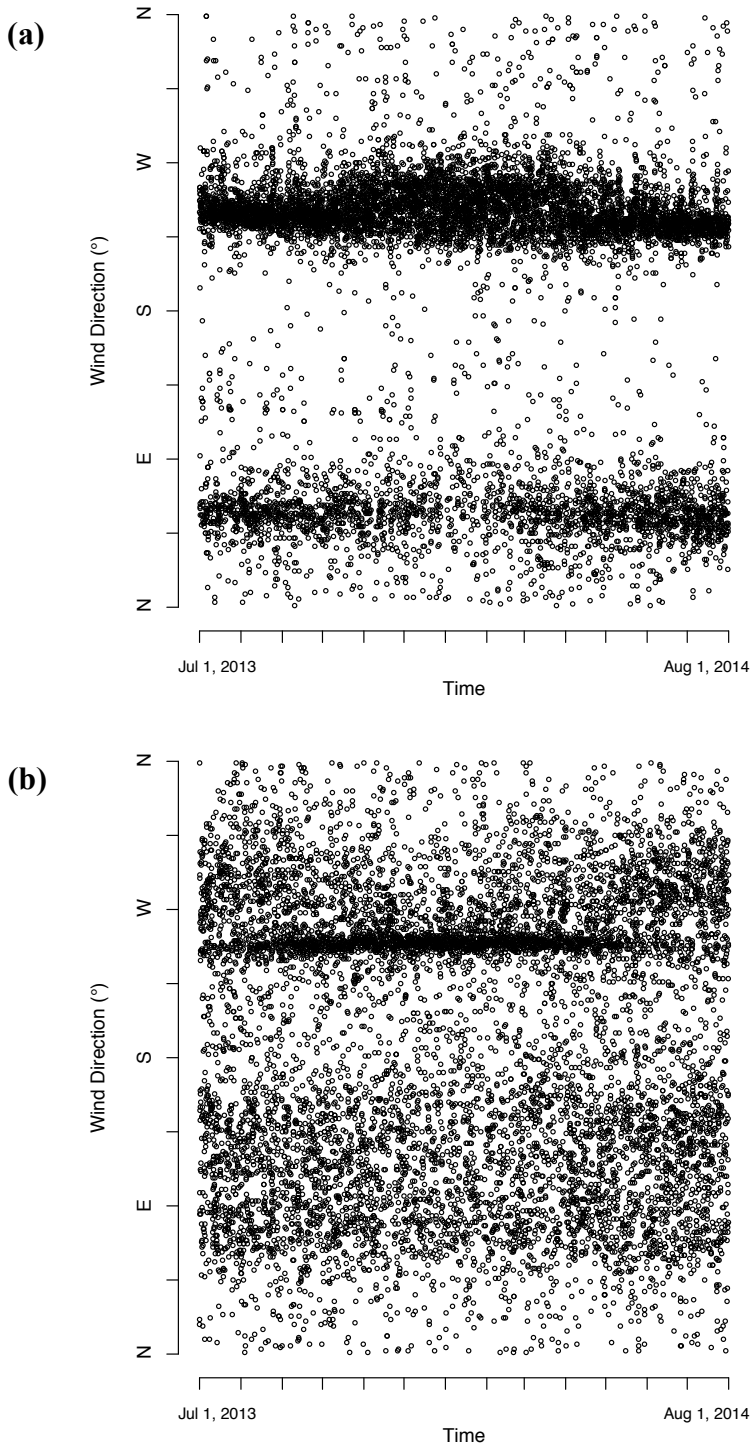

Figure 8. Direction of wind recorded over 13 months starting June 2013 in hourly intervals. Each point represents the recorded direction at each time point at the west site (a) and east site (b).

(a)

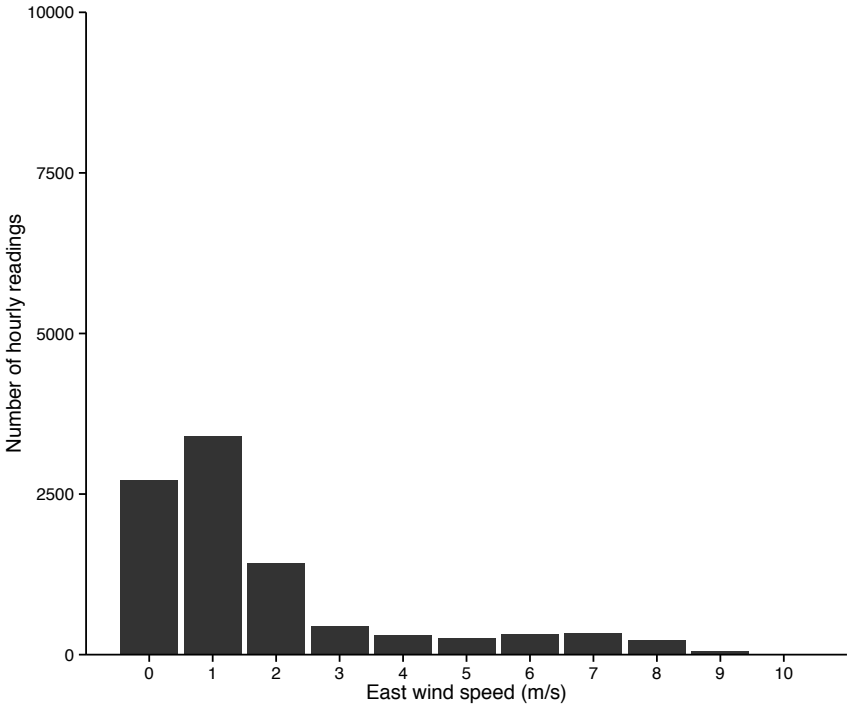

(b)

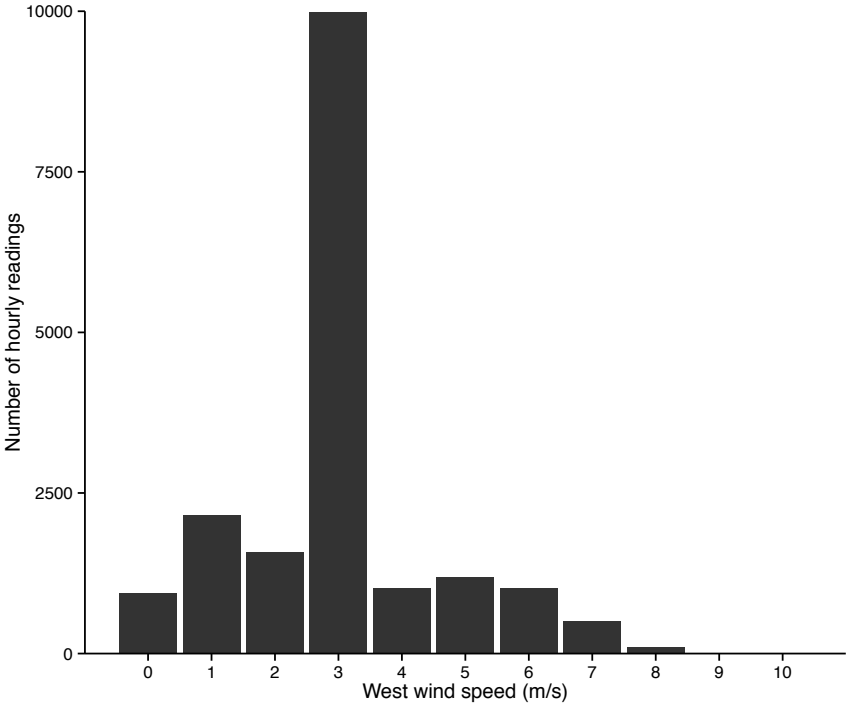

Figure 9. Speed of the winds recorded over 13 months starting June 2013 at the west site (a) and east site (b).

Dune stratigraphy

A coarse, and discontinuous or irregular, platy structure was found on the immediate surface of the dunes. These crusts had easily identifiable zones of lichens, and the lichen density and vibrancy was more distinct at the west site. The biomass and activity of biological soil crusts (BSC), such as these, are concentrated in the upper few mm of a soil and is comprised of an assortment of prokaryotic and eukaryotic organisms (Moore, 1998). Lichen are an intimate symbiotic association of fungi and a photosynthetic partner, either cyanobacteria or algae. Cyanobacteria are known for requiring liquid water for survival, unlike algae, which can activate photosynthesis from fog sources alone (Lange et al., 1993).

Below the crust, the next 10 to 15 cm of the soil formed prominent polygonal structures up to 30 cm in width. With the overlaying material removed, these larger structures appear to have smaller polygons in a somewhat fractal-like pattern (Fig. 10). Throughout the profile were irregularly spaced and somewhat horizontal visible accumulations of sulfate. Individual soil horizons were designated on the basis of changes in the sulfate concentration and soil color and density.

The sediment in the dunes is largely silicate in origin (quartz and feldspar) with varying concentrations of sulfate and chloride salts (bassanite, anhydrite, and halite) (Table 3). At the two sites examined in detail here, the surface layers at both sites have bassanite (a partially hydrated sulfate mineral) as the primary sulfate mineral, whereas anhydrite exceeds bassanite in most soil layers in the lower depths. While bassanite is a somewhat uncommon mineral at the Earth's surface, it has been found in evaporite deposits of arid regions (Hunt et al., 1966; Akpokodje, 1984; Gunatilaka et al., 1985; Mees and De Dapper, 2005). We hypothesize that the frequent interaction of the surface minerals with fog have created a more hydrated sulfate species at the immediate land surface, while high temperatures and low water activity maintain or have formed anhydrite at lower depths.

Inorganic C concentrations in the dunes are very low. In most soils, inorganic C is largely carbonate. However, lichens are well-known producers of Ca-oxalate (eg. Del Monte et al., 1987; Russ et al., 1996), and some or much of the inorganic C here is likely oxalate. Additional evidence for oxalate was generated by samples submitted for carbonate C and O isotope analyses via the phosphoric acid reaction. Anomalously negative ^{13}C values (on the order of -19‰) suggested a non-carbonate contributor to released CO_2. Preliminary subsequent experiments with laboratory grade oxalate reveals a partial reaction with phosphoric acid, and similarly depleted C isotope values. Thus, it is likely that much or all of the inorganic C here is biogenically produced Ca-oxalate.

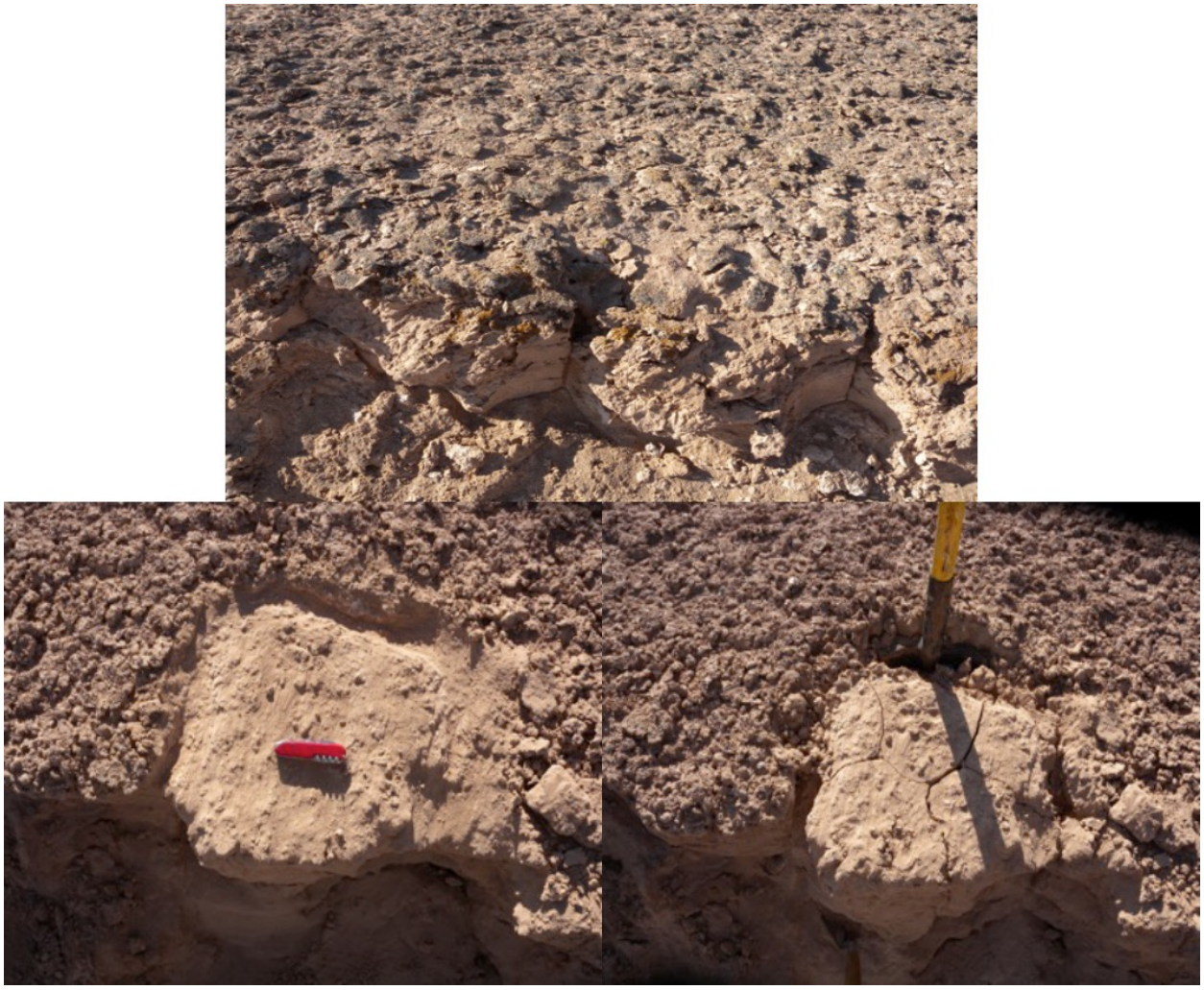

Figure 10. Beneath the surface crust of the dunes are polygonal sulfate structures, which after further cleaning, reveal a somewhat fractal-like pattern.

Sample	Depth (cm)	Classification	Sand (%)	Silt (%)	Clay (%)	Mineralogy top 5 hits on XRD
West 1	0-2	Loamy Fine Sand	79	13	8	bassanite, quartz, anhydrite, albite, monalbite
West 2	2-5	Sandy Loam	72	18	10	anhydrite, quartz, bassanite, albite, muscovite
West 3	5-13	Sandy Loam	68	22	10	bassanite, quartz, anhydrite, albite
West 4	13-32	Sandy Loam	59	32	9	anhydrite, quartz, halite, bassanite, sodalite
West 5	32-49	Sandy Loam	66	25	9	anhydrite, quartz, halite, bassanite, anorthite
West 6	49-67	Sandy Loam	66	26	8	anhydrite, quartz, halite, bassanite, cristobalite
West 7	67-83	Sandy Loam	73	18	9	anhydrite, quartz, halite, albite, bassanite
West 8	83-104	Sandy Loam	73	18	9	anhydrite, quartz, muscovite, bassanite, orthoclase
West 9	104-118	Sandy Loam	64	26	10	anhydrite, quartz, halite, bassanite, albite
West 10	118-127	Sandy Loam	67	22	11	bassanite, quartz, anhydrite, halite, albite
West 11	121-149	Sandy Loam	69	21	10	anhydrite, quartz, halite, albite, bassanite
East 1	0-2	Sandy loam	68	22	10	bassanite, quartz, anhydrite, sylvine, albite
East 2	2-4	Sandy loam	58	36	6	bassanite, quartz, anhydrite, albite, muscovite
East 3	4-7	Sandy loam	53	39	8	anhydrite, quartz, bassanite, albite, muscovite
East 4	7-14	Loam	47	42	11	anhydrite, quartz, anorthite, bassanite, muscovite
East 5	14-31	Sandy loam	56	35	9	anhydrite, quartz, albite, halite, bassanite
East 6	31-33	Sandy loam	57	30	13	quartz, anhydrite, halite, albite, glauberite
East 7	33-52	Sandy loam	54	37	9	anhydrite, quartz, halite, albite, bassanite

Table 3. Textural classification and most dominant minerals found in each dune layer.

Paleoenvironmental records in the loess

Textural analysis of the sediment

Nearly all of the sediment in the dunes has a textural classification of a sandy loam, though strata at the west site have larger grains (more sand) relative to the east site (Table 3; Fig. 11). The exact source(s) of the sediment in these dunes is not fully known. Some may have originated from weathered beach material to the west, however the large areas of deflated alluvial fan are probably a major source of dust in the region. As previously discussed, wind speeds at the west site are ~2x higher than those at the east site. This difference in wind speeds creates a spatial gradient, with grain size decreasing further from the coast as a result of the decreased wind speeds and capacity for transporting larger grains.

Prior to 15,000 yr BP, the proportion of sand and silt that accumulated at each site was relatively constant (though coarser at the western-most site). After this time, both sites began to steadily become more sand-rich, indicative of continuously increasing wind speeds over time (or alternatively, changes in source material supply). The timing of these changes occurs at the same time as the observed decrease in dune growth rate discussed in section 3.2. We interpret this as a reflection of changes in distance from coast and/or wind speeds and fog intensity linked to changes in sea level. An increase in wind speeds would both increase the size of grains transported and increase erosion from the dunes leading to decreased accumulation rates.

Stable isotope ratios of sulfur in sulfate

The $\delta^{34}S$ values of the sulfate at both of the sites does not vary widely, averaging +8.5‰ at the west site and +9.1‰ at the east site (Fig. 12; Table 4). Possible sulfate sources at these sites include: (1) deflated sulfate rich soils, (2) erosion and deflation of anhydrite from the Soledad formation, (3) deflation of ground water sulfates in nearby basins, and (4) marine sources. Rech et al. (2003) report that Andean mantle and juvenile rocks have $\delta^{34}S$ values of -5 to +5‰, and here we report values of +6‰ from the Soledad formation. In contrast, Bao et al. (2000) has reported that biogenic marine sulfates have $\delta^{34}S$ values ranging from +13 to +22‰, and seawater sulfate a $\delta^{34}S$ value of about +21‰. Given these values, both of these sites are likely receiving the majority of their sulfate from some combination of Andean sources (ancient Soledad, salars, local soil sulfate).

A small shift in the isotopic composition of the sulfate occurred roughly ~10,000 yr ago. At this time, $\delta^{34}S$ values begin to steadily increase, possibly suggesting a larger input of marine sulfates, though the total amount remained small. This change occurred at a time that we suggest may have represented an increase in winds and fog intensity. These changes may have contributed larger concentrations of marine material to these dunes, increasing the $\delta^{34}S$ sulfate values.

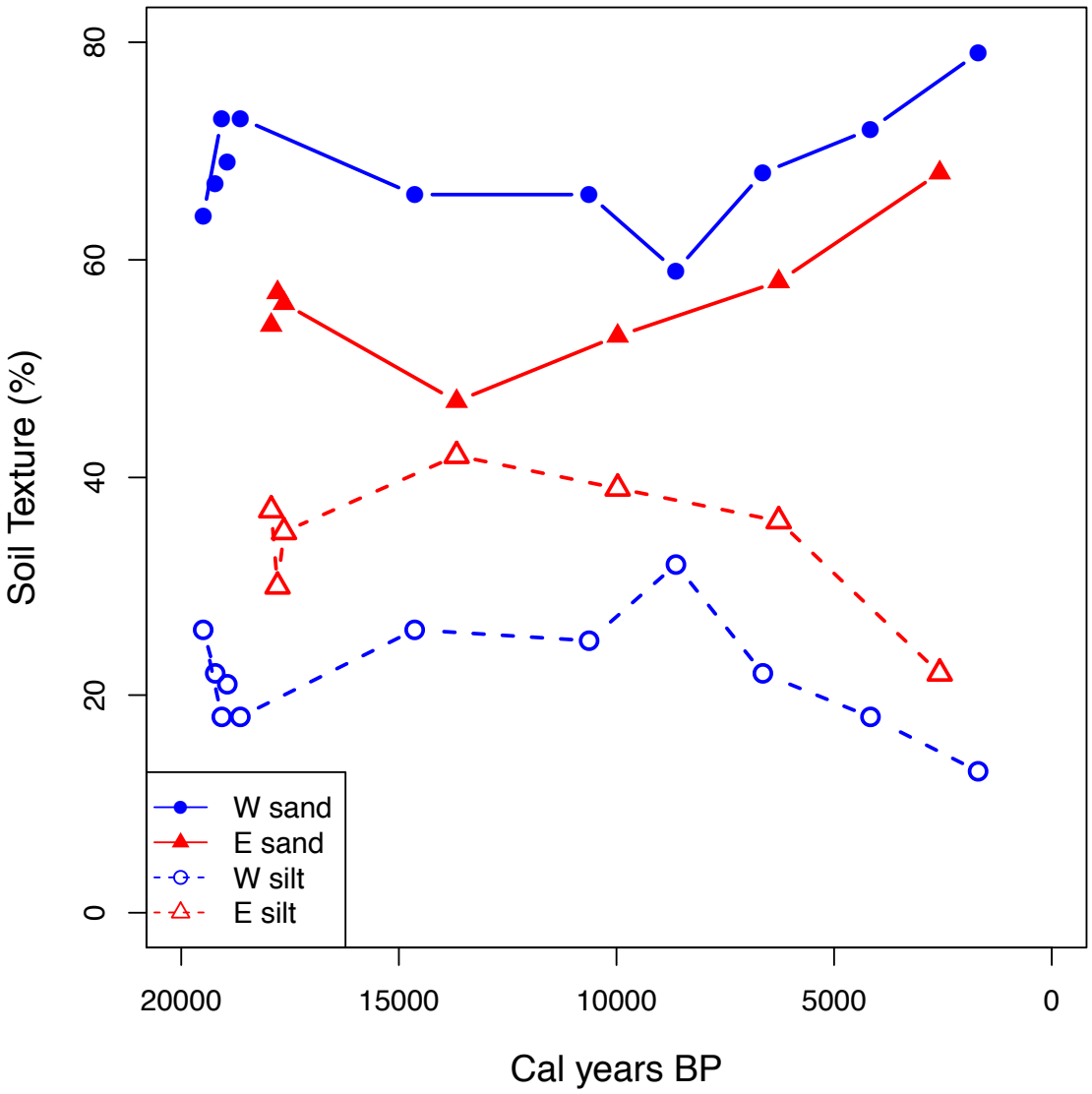

Figure 11. Changes in texture of the sediment at both sites over time. Additional data can be found in Table 3.

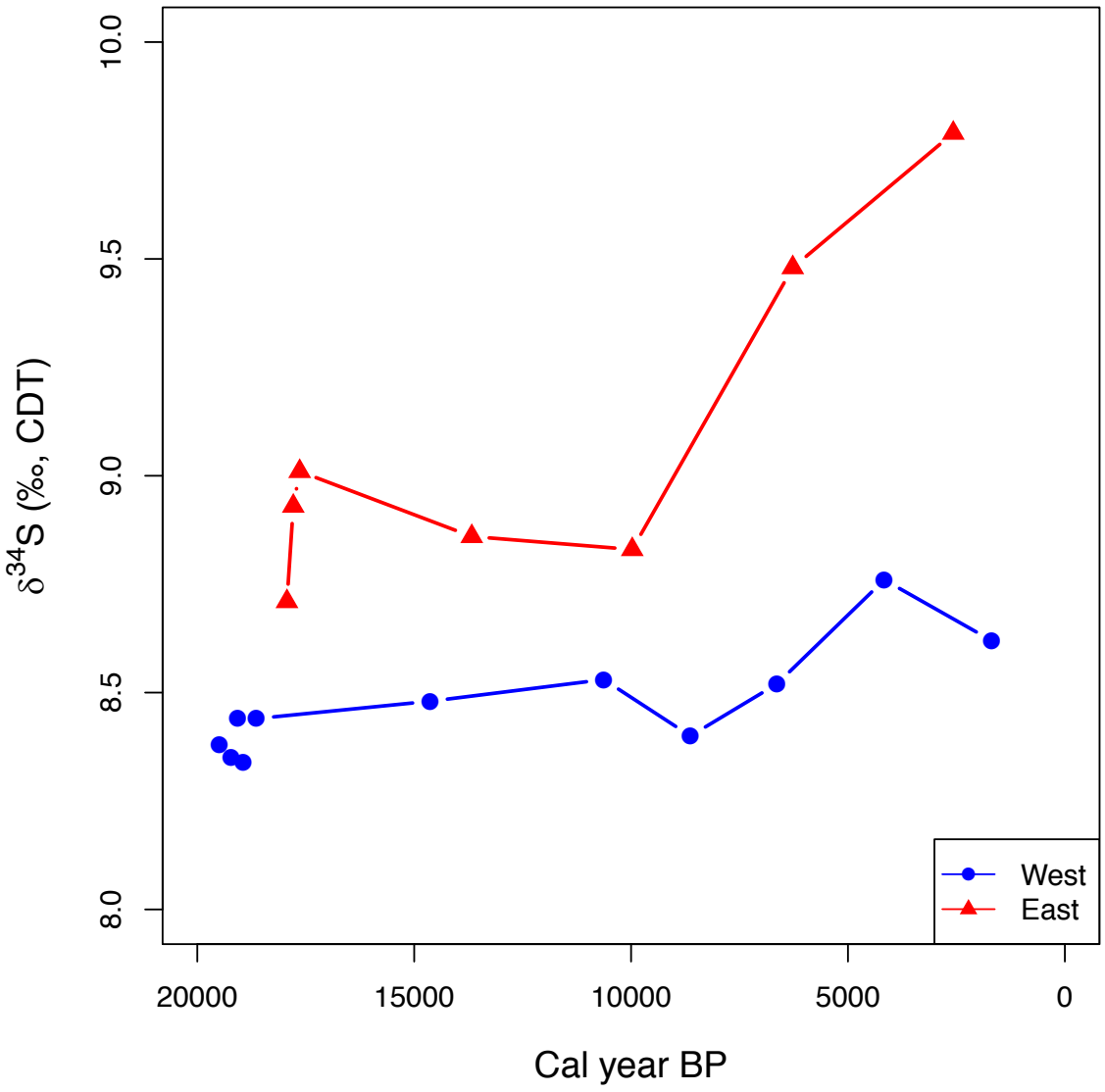

Figure 12. Measured $\delta^{34}S$ values from extractable sulfate at both sites over time. All values are reported relative to CDT.

Sample	Depth	$\delta^{34}S$ sulfate	$\delta^{2}H$ Palmitic Acid	$\delta^{15}N$ org. N
	(cm)	(‰, CDT)	(‰, VSMOW)	(‰, Air N_2)
West 1	0-2	8.54	-88.2	1.59
West 1	0-2	8.69	-85.2	1.48
West 2	2-5	8.77	-98.3	1.68
West 2	2-5	8.74	-103	1.98
West 3	5-13	8.73	-134.3	3.20
West 3	5-13	8.30	-136.5	3.27
West 4	13-32	8.44	-167	4.24
West 4	13-32	8.35	-166.7	4.43
West 5	32-49	8.39	-148.2	3.34
West 5	32-49	8.67	-145.5	3.24
West 6	49-67	8.60	-155.7	4.35
West 6	49-67	8.36	-150.1	4.47
West 7	67-83	8.37	-	7.30
West 7	67-83	8.50	-	7.17
West 8	83-104	8.43	-	6.46
West 8	83-104	8.44	-	6.40
West 9	104-118	8.32	-147.9	3.25
West 9	104-118	8.43	-146.2	3.17
West 10	118-127	8.27	-138.8	2.36
West 10	118-127	8.43	-133.4	2.63
West 11	121-149	8.19	-137	7.16
West 11	121-149	8.49	-142	6.42
East 1	0-2	9.89	-60.6	8.59
East 1	0-2	9.68	-62.2	7.70
East 2	2-4	9.59	-91.2	5.75
East 2	2-4	9.37	-90.7	7.02
East 3	4-7	8.87	-114.8	8.51
East 3	4-7	8.79	-111.6	7.47
East 4	7-14	8.89	-127.2	11.00
East 4	7-14	8.82	-123.6	11.57
East 5	14-31	9.13	-136.5	11.79
East 5	14-31	8.88	-134.7	11.96
East 6	31-33	8.93	-138.2	12.47
East 6	31-33	8.93	-137	13.07
East 7	33-52	8.80	-148.2	16.25
East 7	33-52	8.61	-144.5	16.65

Table 4. Measured stable isotope data from each dune layer.

Stable isotope ratios of hydrogen in fatty acids

The use of δ^2H values in lipid biomarkers as a paleoclimate proxy is becoming increasingly common (eg. Andersen et al., 2001; Sauer et al., 2001; Huang et al., 2002; Sachse et al., 2004a). The basis for the approach is that photosynthetic organisms derive their H from water sources, and therefore the δ^2H in lipid biomarkers reflects the δ^2H of the source plus the effects of biochemically mediated isotope fractionation. Here we focus on palmitic acid, one of the most common fatty acids in both microbes, plants and animals. In both dunes, the δ^2H value of palmitic acid generally increased with decreasing age (Table 4; Fig. 13) Additionally, the east site is about 30 to 50‰ more positive than the lipids in the western dune after 17,000 yr BP. Below, we consider an explanation for these patterns.

The H isotope fractionation between water and fatty acids is reported to be around -160‰ (Sessions et al., 1999; Sachse et al., 2004b). Thus, the water values that the ~ 20,000 yr old lipids formed from is approximately -100‰, much more negative than the water droplets that should form from marine vapor (e.g. 0‰) or from the average atmospheric water vapor itself (-85‰ at 15C, (Horita and Wesolowski, 1994)) .Whatever the source of water in the late Pleistocene for the lichen crust, both sites received similar water and it was very depleted in D relative to what is contributing to the fatty acids at both sites today (or in the recent past). It is possible that rain, rather than fog, provided small amounts of water to the sites. Ewing et al. (2006) suggested that soils further to the south reflect some past periods of surficial modification by rainfall, and that the nearly ubiquitous cap of low density sulfate over the landscape appears to be largely a Holocene phenomenon. However, we here focus on the fog process itself.

Two key processes are expected to affect the isotopic composition of advection fog as it moves across the landscape. First, fog forming over the ocean (0‰) at 15 °C should have a δ^2H of -85‰ (Horita and Wesolowski, 1994). As this fog travels inland and begins to condense and dissipate with westerly winds, the fog vapor will become progressively more negative as the heavier ^2H condenses out in droplets. Second, as the fog rises in elevation and warms as it crosses the continent, the water droplets in the fog will undergo evaporation, increasing their δ^2H values.

At the sites here, the greatest increases in δ^2H values beginning 10,000 yr BP, though the offset between the two sites appeared by 15,000 yr BP. Assuming the isotopic difference between sites is due to the evaporation of the fog droplets during transport to the east (something that is visually apparent in the field), one can use a simple Rayleigh model to estimate the fraction of water droplets that have evaporated between the west and the east site. Assuming an equilibrium fractionation between water and vapor of -85‰, the data suggest a loss of about 50% of the total water. This is roughly consistent with the average RH differences between the sties (Table 2).

The trend toward increasing δ^2H values with time (after 10,000 yr BP) at both sites may hinge on an overall increase in fog density over time, with much less loss of liquid water from the fog mass at the time it reaches the sites. Consistent with this interpretation, the work of Latorre et al. (2011) concluded that fog intensity has been increasing since at least 3,000 yr ago, based on the record of Tillandsia growth. This trend of increasing δ^2H becomes most pronounced at the west site beginning ~10,000 yr BP, the same time we have proposed a shift in wind speeds and increase in marine fog intrusions.

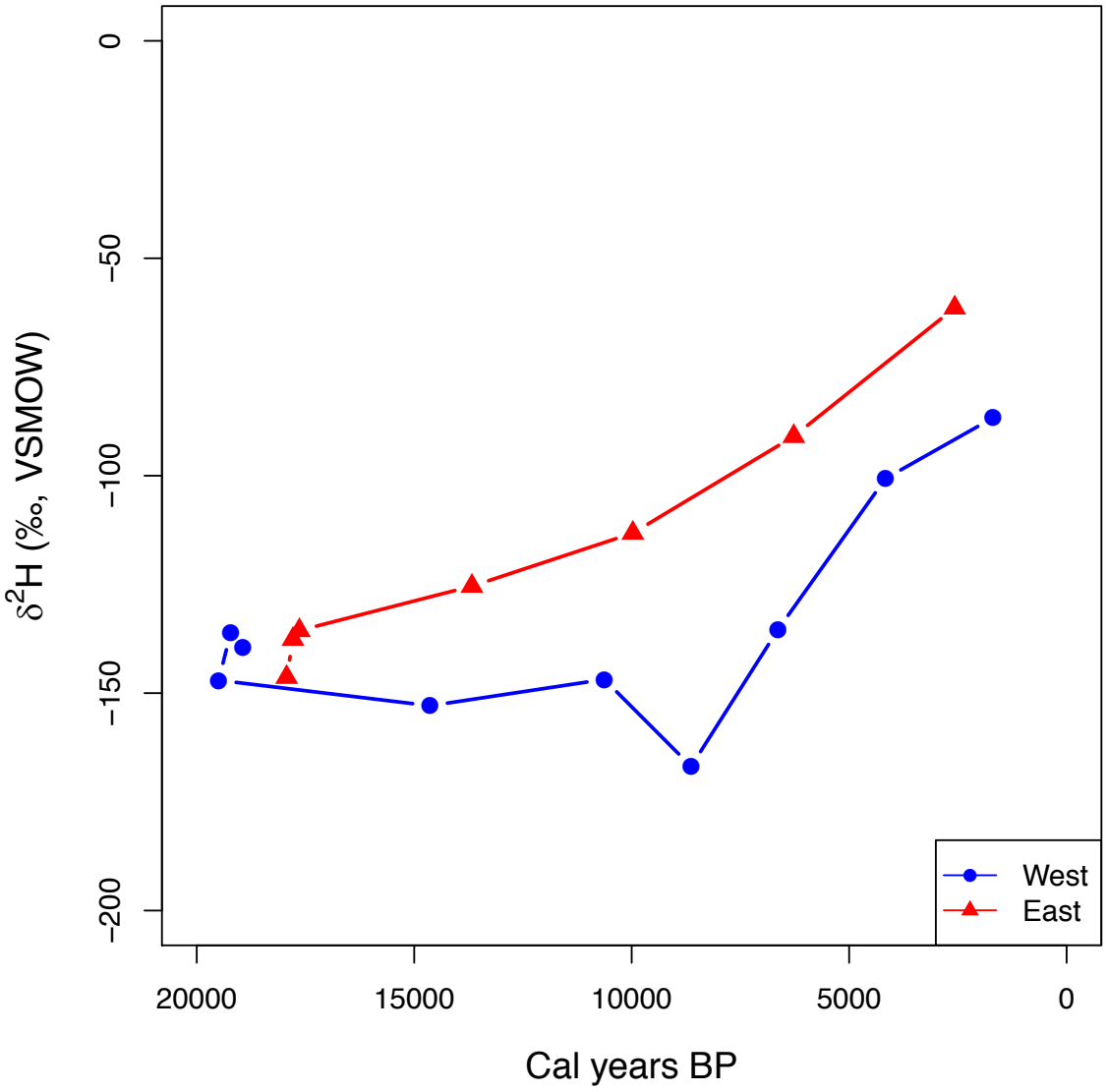

Figure 13. Measured δ^2H values in palmitic acid at both sites over time. All values are reported relative to VSMOW.

Stable isotope ratios of organic nitrogen

In dunes examined here, the $\delta^{15}N$ values of organic N tend to decline with time, at the west site from ~ +7 to +2‰, and at the east site from +17 to +7‰ (Table 4; Fig. 14). The largest declines in $\delta^{15}N$ values occur before ~ 10,000 yr BP.

The organisms comprising the crusts are likely not fixing nitrogen from the atmosphere, but are rather assimilating nitrate and ammonium deposited on the land surface. The source of atmospheric N in the Atacama Desert has been the subject of considerable research. It is well-known that nitrate both in the present atmosphere and in large nitrate accumulations in ancient soils is largely comprised of nitrate that formed in the troposphere via reactions with ozone or related oxidants (Michalski et al., 2004; Ewing et al., 2007). The original source of the N in the nitrate remains less well constrained, but is likely largely from the volatilization of ammonia and NOx from the upwelling of the productive Pacific Ocean.

The isotope composition of marine N is driven by N cycling, and in particular, redox reactions. Recent research has shown that as upwelling increases, biological productivity and oxygen tend to decline (De Pol-Holz et al., 2009; Mollier-Vogel et al., 2012). Currently, the most ^{15}N enriched surface sediment organic matter and surface water NOx in all of Chile and Peru is located about ~20 ^{0}S, essentially west of our field sites. Surface sediment organic matter has a projected $\delta^{15}N$ value of +11 to +15‰, while the NOx has a value of about +17 to +18‰ (Mollier-Vogel et al., 2012). This NOx is likely subject to a number of reactions which form nitrate (Michalski et al., 2004). The N isotope fractionation associated with the processes that oxidize or remove NOx from the atmosphere is very poorly understood, but due to kinetic processes, the lighter isotopes should be concentrated in the reaction products. If NOx is continuously oxidized during transport with air masses, one might expect spatial changes in the remaining NOx gas and resulting deposited nitrate. There is again a lack of systematic study of natural systems to confirm this hypothesis. Nonetheless, we use this conceptual model to consider and evaluate the N isotope composition of the organic N in the dune soils.

We assume that N taken up by biological processes in the lichens cause little isotope fractionation, and that the buried organic matter has not been subject to isotope fractionation. The virtual absence of rainfall, and the preservation of C for 10's of thousands of years, lends support to these assumptions. The $\delta^{15}N$ value of the surface material at the western most (coastal) site is about +2‰, 15‰ more negative than measured NOx in the nearby marine environment. The $\delta^{15}N$ values of nitrate in ancient soils at this latitude are reported to be between +0.6 and -1.6 ‰ (Michalski et al., 2004), consistent with long term N deposition (over millions of years) in the region. The offset between measured marine NOx and nitrate (Michalski et al., 2004) and organic N (here) suggest either a large fractionation between NOx and nitrate, or some other sources or mechanisms of atmospheric N in the region. However, a large fractionation between NOx and deposited nitrate is consistent with our data. The east site, downwind and along a plausible transport and reaction pathway, has had, throughout the last 20,000 yr, a nearly 5‰ greater $\delta^{15}N$ value than the west site. Assuming that nitrate formation enriches the remaining NOx in ^{15}N, this constant offset is supportive of both a large fractionation, and progressive loss of NOx as the air mass moves inland.

As a first approximation, assuming that the air mass has lost 50% of its N between the west and east sites (the mass of water lost by H isotope interpretations), the apparent fractionation factor is -10‰ (derived using a Rayleigh fractionation model, Criss (1999)). This suggests the atmospheric N at the western sites is about +12‰. A recent study of the N isotope composition of nitrate deposited in dust collectors to the south of our study area suggests that nitrate becomes *depleted* in ^{15}N with increasing distance from the coast, which would imply that the deposited nitrate is enriched in ^{15}N relative to NOx (Wang et al., 2014). However, this transect is complicated by likely anthropogenic sources near the coast, as discussed in their paper. In contrast, it has been reported that the $\delta^{15}N$ values of nitrate collected on snow surfaces *increase* from ~ -11‰ at the Antarctic coast to +25‰ 1000 km inland. While we do not know the combination of mechanisms or species involved in the accumulation of N in the dunes examined here, it is clear that the deposited forms of N are more depleted that the source, and that these processes have remained constant through time.

The organic N $\delta^{15}N$ value in the dunes examined here are in a very unique setting, one which can possibly provide connections to the marine record. While the $\delta^{15}N$ values within the dunes have become much more negative since the LGM (by 8 or 9‰), the $\delta^{15}N$ values of organic N in offshore marine sediments has become enriched in ^{15}N by up to 6‰ since the end of the LGM. Within the Holocene, the sediment core at 30° S undergoes a 2 or 3‰ decline in $\delta^{15}N$ to its minimum at 7,000 years BP, followed by a 1 to 2‰ increase to the present value (De Pol-Holz et al., 2007). There is an anti-correlation between the dunes and the marine record over time. As discussed, we suggest this lack of correlation is embedded in isotope effect of air mass N processing, and its changes in path length (and elevation above sea level) over time. The decline in the $\delta^{15}N$ values at both sites over time (most significant during 20,000 to 10,000 ya BP), is consistent with a longer transport distance from the coast at the LGM, which would cause any NOx bearing air mass to have undergone more reaction before reaching the sites than the present sea level imposes. The observation that most of the change in $\delta^{15}N$ values at both sites largely ceased or decreased by 10,000 yr BP is consistent with the stabilization of sea level, and the emplacement of the present sea to shore flow paths that characterize the region today.

While it is clear that there are large uncertainties in isotope fractionation factors, and in the mechanisms of N transport and chemical processing, the N isotope patterns examined here suggest a number of follow-up questions and studies on the local N cycle. Even with these uncertainties, the data are consistent with other chemical and physical data we have examined in the dunes, data that suggests these sites are recording changes in fog intensity and its related impacts over late Quaternary time.

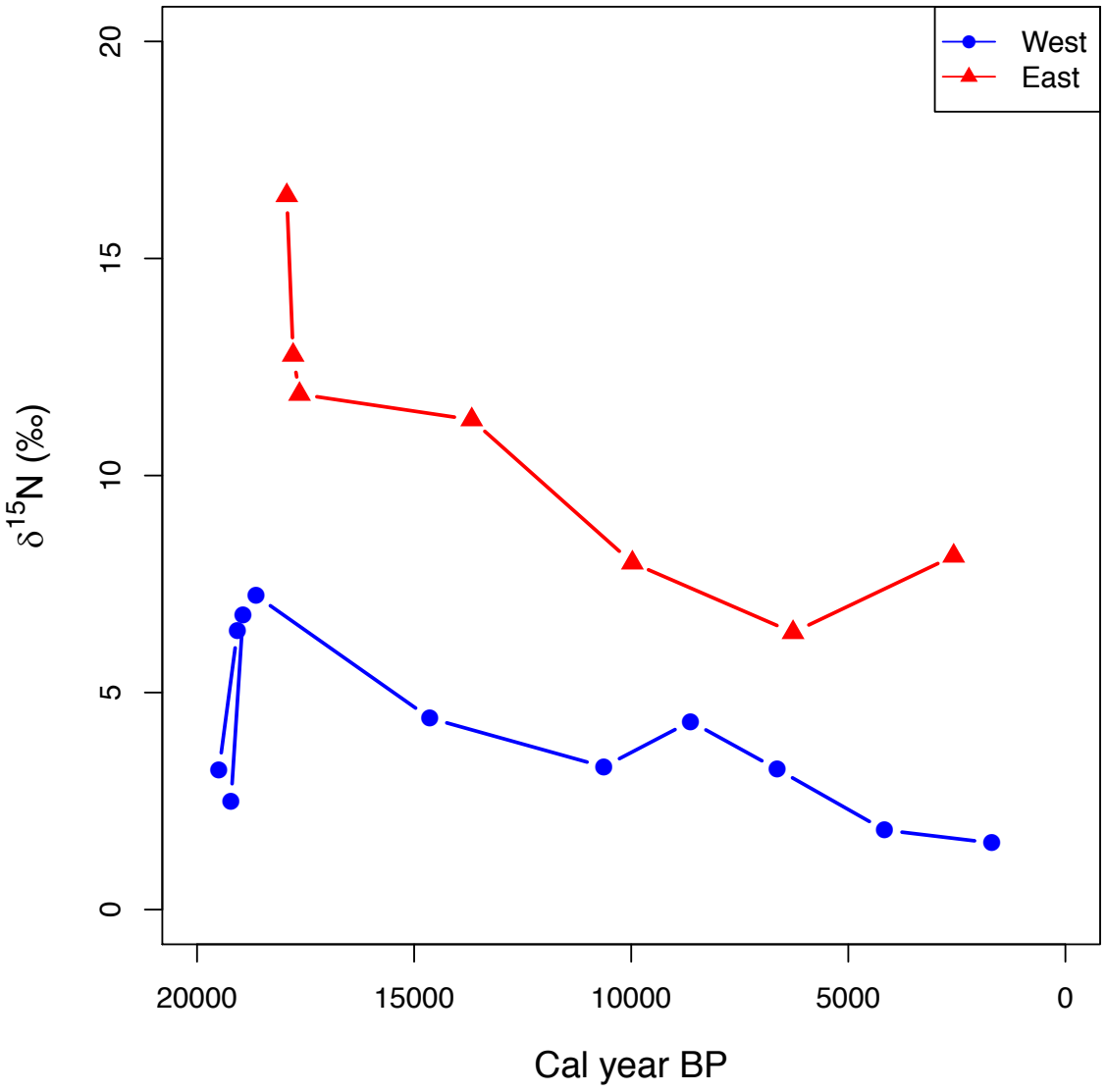

Figure 14. Measured $\delta^{15}N$ values in organic nitrogen from the sediments at both sites over time. All values are reported relative to N_2 Air.

Conclusions

Here, we report on our discovery of small scale late Quaternary loess deposits in a windy and fog impacted region of the Atacama Desert. The unique accumulation of dust has apparently occurred as a result of a combination of sea level and fog intensity changes that occurred in the late Pleistocene to Holocene. The dunes form in a rugged badland-type topography that lends itself to creating local reductions in wind velocity and the settling of suspended particles in the surface winds. Radiocarbon ages of organic matter embedded within the deposits shows that the deposits began accumulating rapidly at the LGM, and that accumulation of sediment slowed considerably after the Pacific Ocean attained its present post-glacial level.

Due to the extreme aridity and lack of biological mixing processes, the dunes retain a detailed stratigraphic record of chemical and physical changes over time. Chemical and H isotopic analysis of the sediment and fatty acids preserved within the dunes provide evidence for increased marine fog density and intensity of onshore westerly winds beginning 10,000 yr BP. At this time, grain sizes are seen to increase at both sites while accumulation rates simultaneously decrease, suggesting greater wind speeds and/or decrease in sediment supply. The $\delta^{34}S$ in sulfate begins to increase, possibly indicative of more marine sulfate. Organic sediment $\delta^{15}N$ values steadily decreases, suggesting a shorter path length between N upwelling and N deposition and subsequent assimilation by the lichens and other organisms in the crust. Finally, the $\delta^{2}H$ values in palmitic acid retrieved from the sediment increase over time, which we tentatively interpret as reflecting the presence of a thicker and denser fog.

This unique and continuous record of paleo-conditions provides a window into local processes that were impacted by a complex array of sea-level, marine upwelling, and fog processes. In particular, the sediments accumulate N from the nearby upwelling Pacific, and thus provide land-based responses to large scale marine processes. The depth sampling conducted here was relatively coarse, in order to test whether the sediments indeed accumulated continuously. It appears that much finer scale depth increments coupled with radiocarbon dating should be able to provide a much higher resolution late Quaternary record. In addition, the quantification and stable N isotope analyses of both ammonium and nitrate in the sediment (to complement the organic N) will prove to be important to better understand the marine-terrestrial linkages in this region.

References

Akpokodje, E. 1984. The occurrence of bassanite in some Australina arid zone soils. Chemical Geology: 361–364.

Amundson, R., W. Dietrich, D. Bellugi, S. Ewing, K. Nishiizumi, G. Chong, J. Owen, R. Finkel, A.M. Heimsath, B. Stewart, and M. Caffee. 2012. Geomorphologic evidence for the late Pliocene onset of hyperaridity in the Atacama Desert. Geological Society of America Bulletin.

Andersen, N., H. Paul, S. Bernasconi, J. McKenzie, A. Behrens, P. Schaeffer, and P. Albrecht. 2001. Large and rapid climate variability during the Messinian salinity crisis: Evidence from deuterium concentrations of individual biomarkers. Geology: 799–802.

Anderson, R.S., and S.P. Anderson. 2010. *Geomorphology: the mechanics and chemistry of landscapes*. Cambridge University Press.

Bao, H., D.A. Campbell, J.G. Bockheim, and M. Thiemens. 2000. Origins of Sulphate in Antarctic Dry-Valley Soils as Deduced From Anomalous ^{17}O Compsitions. Nature: 1–4.

Burgess, S.S.O., and T.E. Dawson. 2004. The contribution of fog to the water relations of Sequoia smpervirens (D. Don): foliar uptake and prevention of dehydration. Plant, Cell and Environment 27: 1023–1034.

Criss, R.E. 1999. Principles of stable isotope distribution. Oxford University Press.

De Pol-Holz, R., R.S. Robinson, D. Hebbeln, D.M. Sigman, and O. Ulloa. 2009. Controls on sedimentary nitrogen isotopes along the Chile margin. Deep Sea Research Part II: Topical Studies in Oceanography 56(16): 1042–1054.

De Pol-Holz, R., O. Ulloa, F. Lamy, L. Dezileau, P. Sabatier, and D. Hebbeln. 2007. Late Quaternary variability of sedimentary nitrogen isotopes in the eastern South Pacific Ocean. Paleoceanography 22(2).

Del Monte, M., C. Sabbioni, and G. Zappia. 1987. The origin of calcium oxalates on historical buildings, monuments, and natural outcrops. The Science of the Total Environment 67: 17–39.

Ewing, S.A., G. Michalski, M. Thiemens, R.C. Quinn, J.L. Macalady, S. Kohl, S.D. Wankel, C. Kendall, C.P. McKay, and R. Amundson. 2007. Rainfall limit of the N cycle on Earth. Global Biogeochemical Cycles 21(3): GB3009.

Ewing, S.A., B. Sutter, J. Owen, K. Nishiizumi, W. Sharp, S.S. Cliff, K. Perry, W. Dietrich, C.P. McKay, and R. Amundson. 2006. A threshold in soil formation at Earth's arid–hyperarid transition. Geochimica et Cosmochimica Acta 70(21): 5293–5322.

Gayo, E.M., C. Latorre, T.E. Jordan, P.L. Nester, S.A. Estay, K.F. Ojeda, and C.M. Santoro. 2012. Late Quaternary hydrological and ecological changes in the hyperarid core of the northern Atacama Desert (~21°S). Earth-Science Reviews 113(3-4): 120–140.

Gee, G., and J. Bauder. 1986. Gee_Bauder_1986. p. 383–411. *In* Klute, A. (ed.), Methods of Soil Analysis, Part 1. 2nd ed. ASA and SSSA, Madison, WI.

Graber, E.R., and L. Tsechansky. 2010. Rapid One-Step Method for Total Fatty Acids in Soils and Sediments. Soil Science Society of America Journal 74(1): 42.

Gunatilaka, A., A. Al Temeemi, A. Saleh, and N. Nassar. 1985. A new occurrence of bassanite in recent evaporitic environments, Kuwait, Arabian Gulf. Kuwait Journal of Science 12: 157–166.

Hartley, A., and G. Chong. 2002. Late Pliocene age for the Atacama Desert: Implications for the desertification of western South America. Geology 30: 43–46.

Hogg, A., Q. Hua, P. Blackwell, M. Niu, C. Buck, T. Guilderson, T. Heaton, J. Palmer, P.

Reimer, R. Reimer, C. Turney, and S. Zimmerman. 2013. SHCAL13 southern hemisphere calibration, 0–50,000 years cal bp. Radiocarbon 55: 1889–1903.
Horita, J., and D.J. Wesolowski. 1994. Liquid-vapor fractionation of oxygen and hydrogen isotopes of water from the freezing to the critical temperature. Geochimica et Cosmochimica Acta 58: 3425–3437.
Houston, J. 2006. Evaporation in the Atacama Desert: An empirical study of spatio-temporal variations and their causes. Journal of Hydrology 330(3-4): 402–412.
Hua, Q., M. Barbetti, and A. Rakowski. 2013. Atmospheric radiocarbon for the period 1950–2010. Radiocarbon 55: 2059–2072.
Huang, Y., B. Shuman, Y. Wang, and T.I. Webb. 2002. Hydrogen isotope ratios of palmitic acid in lacustrine sedimentsrecord late Quaternary climate variations. Geology 12: 1–4.
Hunt, C., T. Robinson, W. Bowles, and A. Washburn. 1966. Hydrologic Basin Death Valley California. Geological Survery Professional Paper 494-B.
Jordan, T.E., N.E. Kirk-Lawlor, N.P. Blanco, J.A. Rech, and N.J. Cosentino. 2014. Landscape modification in response to repeated onset of hyperarid paleoclimate states since 14 Ma, Atacama Desert, Chile. Geological Society of America Bulletin 126(7-8): 1016–1046.
Lambeck, K., Y. Yokoyama, and T. Purcell. 2002. Into and out of the Last Glacial Maximum: sea-level change during Oxygen Isotope Stages 3 and 2. Quaternary Science Reviews 21: 343–1360.
Lange, O.L., B. BÜdel, A. Meyer, and E. Kilian. 1993. Further Evidence That Activation of Net Photosynthesis by Dry Cyanobacterial Lichens Requires Liquid Water. The Lichenologist 25: 175–189.
Latorre, C., A.L. González, J. Quade, J.M. Fariña, R. Pinto, and P.A. Marquet. 2011. Establishment and formation of fog-dependent Tillandsia landbeckiidunes in the Atacama Desert: Evidence from radiocarbon and stable isotopes. Journal of Geophysical Research 116(G3): G03033.
Latorre, C., C.M. Santoro, P.C. Ugalde, E.M. Gayo, D. Osorio, C. Salas-Egaña, R. De Pol-Holz, D. Joly, and J.A. Rech. 2013. Quaternary Science Reviews. Quaternary Science Reviews 77(C): 19–30.
Mees, F., and M. De Dapper. 2005. Vertical variations in bassanite distribution patterns in near-surface sediments, southern Egypt. Sedimentary Geology 181(3-4): 225–229.
Michalski, G., J.K. Bohlke, and M. Thiemens. 2004. Long term atmospheric deposition as the source of nitrate and other salts in the Atacama Desert, Chile: New evidence from mass-independent oxygen isotopic compositions. Geochimica et Cosmochimica Acta 68(20): 4023–4038.
Mollier-Vogel, E., E. Ryabenko, P. Martinez, D. Wallace, M.A. Altabet, and R. Schneider. 2012. Deep-Sea Research I. Deep-Sea Research Part I 70(c): 14–25.
Moore, P.D. 1998. Life in the upper crust. Nature 393: 419–420.
Nester, P.L., E.M. Gayo, C. Latorre, T.E. Jordan, and N. Blanco. 2007. Perennial stream discharge in the hyperarid Atacama Desert of northern Chile during the latest Pleistocene. Proceedings of the National Academy of Sciences 104: 19724–19729.
Pueyo, J.J., G. Chong, and A. Jensen. 2001. Neogene evaporites in desert volcanic environments: Atacama Desert, northern Chile. Sedimentology 48: 1411–1431.
Quade, J., J.A. Rech, J.L. Betancourt, C. Latorre, B. Quade, K.A. Rylander, and T. Fisher. 2008. Paleowetlands and regional climate change in the central Atacama Desert, northern Chile. Quaternary Research 69(3): 343–360.

Rech, J.A., J. Quade, and J.L. Betancourt. 2002. Late Quaternary paleohydrology of the central Atacama Desert (lat 22-24 S), Chile. GSA Bulletin 114: 334–348.
Rech, J.A., J. Quade, and W.S. Hart. 2003. Isotopic evidence for the source of Ca and S in soil gypsum, anhydrite and calcite in the Atacama Desert, Chile. Geochimica et Cosmochimica Acta 67(4): 575–586.
Russ, J., R. Palma, D. Loyd, T.W. Boutton, and M. Coy. 1996. Origin of the Whewellite-Rich Rock Crust in the Lower Pecos Region of Southwest Texas and Its Significance to Paleoclimate Reconstructions. Quaternary Research 46: 27–36.
Sachse, D., J. Radke, and G. Gleixner. 2004a. Hydrogen isotope ratios of recent lacustrine sedimentary n-alkanes record modern climate variability. Geochimica et Cosmochimica Acta 68(23): 4877–4889.
Sachse, D., J. Radke, R. Gaupp, L. Schwark, G. L niger, and G. Gleixner. 2004b. Reconstruction of palaeohydrological conditions in a lagoon during the 2nd Zechstein cycle through simultaneous use of ?D values of individual n-alkanes and ?18O and ?13C values of carbonates. Int J Earth Sci (Geol Rundsch).
Sauer, P., T.I. Eglinton, J.M. Hayes, A. Schimmelmann, and A.L. Sessions. 2001. Compound-specific D/H ratios of lipid biomarkers from sediments as a proxy for environmental and climatic conditions. Geochimica et Cosmochimica Acta 65: 213–222.
Sessions, A.L., T. Burgoyne, A. Schimmelmann, and J.M. Hayes. 1999. Fractionation of hydrogen isotopes in lipid biosynthesis. Organic Geochemistry 30: 1193–1200.
Soil Survey Staff. 1999. Soil Taxonomy: A Basic System of Soil Classification for Making and Interpreting Soil Surveys. 2nd edition. Natural Resources Conservation Service. US Department of Agriculture Handbook 436.
Stuiver, M., and H. Polach. 1977. Reporting of 14C data. Radiocarbon 19: 355–363.
Tsoar, H., and K. Pye. 1987. Dust transport and the question of desert loess formation. Sedimentology 34: 139–153.
Turk, J.K., and R.C. Graham. 2011. Distribution and Properties of Vesicular Horizons in the Western United States. Soil Science Society of America Journal 75(4): 1449.
Vogel, J.S., J.R. Southon, D.E. Nelson, and T.A. Brown. 1984. Performance of catalytically condensed carbon for use in accelerator mass spectrometry. Nuclear Instuments and Methods in Physics Research: 289–293.
Wang, F., G. Michalski, J.-H. Seo, and W. Ge. 2014. Geochemical, isotopic, and mineralogical constraints on atmospheric deposition in the hyper-arid AtacamaDesert, Chile. Geochimica et Cosmochimica Acta 135(C): 29–48.
Workman, T. 2012. Paleowetlands and Fluvial Geomorphology of Quebrada Mani: Reconstructing Paleo-Environments and Human Occupation in the Northern Atacama Desert. 1–41.
Yokoyama, Y., K. Lambeck, P. De Deckker, P. Johnston, and L.K. Fifield. 2000. Timing of the Last Glacial Maximum from observed sea-level minima. Nature 406(6797): 713–716.